Delft University of Technology

_____

Impact of pore scale heterogeneity on salt precipitation and hydrate formation during CO₂ storage in porous media

Author:

Manon Arianne Renée Schellart

To be defended on:

08-07-2024

Thesis Committee	Dr. R. Farajzadeh	TU Delft and Shell, Supervisor
	Dr. Ir. H. Hendrikse	TU Delft, Supervisor
	Dr. D.V. Voskov	TU Delft, Co-Supervisor
	Dr. L. Yan	TU Delft, Daily-Supervisor
	Dr. A. Barnhoorn	TU Delft, Graduation Committee Member

Acknowledgements

I would like to express my deepest gratitude to my principal supervisor, Dr. Rouhi Farajzadeh, for the invaluable weekly meetings and guidance throughout my research. It was very special how, despite living in another country, he always managed to convey his meaningful involvement and help. I am equally grateful to my postdoctoral supervisor, Dr. Lifei Yan, for his significant contributions and for teaching me how to conduct the micromodel experiments for both salt dry-out and hydrate studies.

My appreciation extends to my other supervisors as well. Dr. Ir. Hayo Hendrikse, although our contact was limited, consistently provided clear and actionable feedback. I am thankful to Dr. Denis Voskov for the weekly group meetings and the support he offered during these sessions.

I also wish to thank the members of the reservoir lab team, Dr. Mahnaz Aghajanloo and Dr. Sian Jones, for always being available to answer my questions and for their thorough explanations and unwavering support. Mahnaz often brought delicious Iranian food to share, and Sian baked amazing cakes, brownies, and especially mochi recipes.

A special thanks goes to our lab technician, Michiel Slob. His expertise and the construction of the setups I used were critical to the success of my research. Without his knowledge and assistance, my experiments would not have been possible.

I thoroughly enjoyed working on my thesis and appreciated the vibrant atmosphere at the university. The lab technicians, even those not directly involved with my lab, were always approachable for both personal and professional conversations. My thanks go out to Marc Friebel, Karel Heller, Jens van den Berg, and Jelle Kampf for their camaraderie and support. Also, the intern lab technician Laurens Boersma is owned many thanks, due to his wide-ranging support.

Moreover, the days I spent working on my thesis at the Shell office were a valuable experience. Gaining firsthand experience in such a large and influential company was enlightening. I met many people with diverse backgrounds and expertise, and it was always fascinating to have conversations with so many different specialists. I would like to thank many people at Shell for their insights and support. In particular, I had numerous conversations with Dr. Diederik Boersma, discussing everything from frustrations about my thesis to the beauty of student associations and the similarities and differences we experienced during our student years. I always enjoyed these conversations. The Shell outings, such as the Christmas party, were very enjoyable.

Additionally, I am grateful to Dr. Steffen Berg from Shell, who dedicated an entire day to help me optimize my image simulation program for processing my experimental data.

Next to the professional support, I would also like to thank those who supported me personally. My parents and sister were not directly involved in my thesis work but were always open to talk. I am especially grateful to my boyfriend for the discussions we sometimes had at home about my research and for his help when I encountered obstacles, as we often found solutions together.

Concluding, my time as a student at TU Delft with this fascinating thesis topic has been an incredible experience. I am enthusiastic and curious about what the future holds, and I hope to always remain involved in this field!

Abstract

This thesis explores the occurrence of salt dry-out and hydrate formation when injecting CO_2 into porous media. In large-scale CCS projects, injecting CO_2 can potentially lead to salt precipitation or hydrate formation. These processes diminish injectivity and negatively alter reservoir rock properties. To gain deeper insight, experiments were conducted utilizing microfluidic setups, which allow for visual observation of salt-crystal or hydrate formation. Using microfluidic chips, ten salt dry-out experiments were conducted with varying pore sizes and six hydrate experiments were conducted with varying pulse trigger times. For the dry-out experiments, it was shown that salt crystals form mostly at the outlet side and that heterogeneity has a large impact on the precipitation process. A heterogeneous pattern results in a shift in salt distribution to the small pores, with results showing salt saturation at 7% in the small pore section of the medium-small pore chip, exceeding the 3% in the larger pore section. This shows the significant role of capillary action on salt precipitation. Results highlight that higher CO_2 flow rates accelerate water evaporation and salt formation, yet final salt precipitation levels remain similar across varied flow rates. For instance, in the small pore size chip, final salt saturation was observed at 7% with a flow rate of 4.38 mm/s, decreasing to 4% at 0.78 mm/s. Additionally, the importance of high water saturation for salt dry-out and the impact of water backflow is shown. For hydrate formation, the importance of temperature and pressure was noted in these experiments. Three different pressure pulses were employed: manual control, a 0.5-second electronic pulse, and a 0.2-second electronic pulse, which all showing great effect on hydrate formation, yet no correlation could be determined between pulse length and hydrate saturation. Specifically, manual control yielded a 15% hydrate saturation with a 9.4% conversion factor, while the 0.5-second pulse achieved a 7% saturation and 9.1% conversion factor. The 0.2-second pulse resulted in 8% saturation and a 5.9% conversion factor. For the dissociation, the large effect of temperature was observed. All experiments showed a stable hydrate concentration, and a dissociation temperature between 5 and 9°C where temperature differences as small as 0.1°C were shown to be the difference between no dissociation and complete disappearance of all hydrates. Next to this kinetics, an interesting observation regarding the hydrate morphology was made. In addition to the five hydrate morphologies found in literature, a sixth, 'sheet'-like type was observed.

Contents

List of figures

List of tables

Nomenclature

Abbreviation	Meaning	Unit
CO_2	Carbon Dioxide	
CCS	Carbon Capture and Storage	
P_c	Capillary pressure	Pa
P_{inj}	Well injection pressure	Pa
γ	Interfacial tension	Nm
θ	Contact angle	Deg
R	Effective radius	m
N_c	Capillary Number	
μ	Viscosity	Pa s
w	Channel width	m
h	Channel height	m
L	Channel Length	m
q	Flow speed	m/s
wt%	Weight percent	%
CH_4	Methane	
N_2	Nitrogen	
MFC	Mass flow controller	
EOR	Enhanced Oil Recovery	
k	Darcy Permeability	
m_H	Hydrate mass	g
S_H	Hydrate saturation	%
PV	Pore Volume	L
ρ_H	Hydrate density	g/L
Conv	Conversion factor	%
n_{H_2O}	Moles water	mol
Mw	Molecular mass	g/mol
N_H	Moles water per mol CO_2	

1 Introduction

The project's objective is to address a hurdle in CO_2 storage in the subsurface: injectivity loss due to salt precipitation, mostly in saline aquifer or hydrate formation, mostly in depleted gas fields. Ensuring safe and long-term CO_2 injection requires preventing clogged pore spaces near the injection well and within the reservoir. This research aims to pinpoint the causes, locations, and timing of CO_2 well injectivity loss stemming from salt precipitation or hydrate formation. It further sought to identify operational factors that can minimize the risk of reduced injectivity.

Salt precipitation in porous media can present significant obstacles to the efficacy of carbon capture and storage (CCS) in among others, deep saline aquifers. This is due to the formation of pore-blocking salt crystals, which can decrease the permeability of the surrounding formations and, consequently, the injectivity of wells. However, comprehending the pore-scale dynamics and underlying mechanisms of salt nucleation using traditional core-flooding techniques proves challenging.

Next to salt precipitation, injectivity can also be hindered by gas hydrates. Gas hydrates are solid crystalline compounds formed by water and gas molecules through molecular interactions, typically occurring at low temperatures and high pressures. They have sparked interest in studying the kinetics of CO_2 hydrate formation, particularly in the presence of various additives, driven by their applications in CO_2 capture. While gas hydrates hold promising potential for CCS, they may pose challenges if they undesirably form around injection pipes, obstructing the flow of CO_2 to underground storage formations. This unintended occurrence could diminish the effectiveness of CCS projects, highlighting that research to achieve precise control over the hydrate formation process is necessary.

To address these two issues, microfluidic experiments were conducted to offer high-resolution, pore-scale measurements of the de-wetting patterns and drying rates of brine, along with subsequent salt precipitation during gas injection. These experiments also delve into the impact of pore structures and brine concentrations on these phenomena.

1.1   Relevance of the study

1.1.1   Climate change and fossil fuels

Finding a solution for climate change is arguably most important scientific goal of the 21st century. The latest IPCC report, released in Interlaken, Switzerland, highlights the need for climate action as global warming reaches 1.1°C above pre-industrial levels due to prolonged fossil fuel use. To limit warming to 1.5°C, greenhouse gas emissions must be reduced by nearly half by 2030 (IPCC — Intergovernmental Panel on Climate Change, 2023). By now, it is a well-established fact that climate change is mostly caused by the burning of fossil fuels for energy, heat, and industrial products (Ghoniem, 2011). Countries all over the world are scrambling to switch to renewable energy sources. However, most countries have grown dependent on fossil fuels over the last decade. Quitting instantaneously would be catastrophic for the world economy (Suranovic, 2013). Therefore, technologies are necessary which can facilitate the transition, and ensure quick CO_2 reduction while phasing out fossil fuels. However, this debate is not part of this thesis, but findings could be used in future research to develop technologies that can help facilitate the energy transition.

1.1.2   Carbon capture and storage

CCS is a method designed to mitigate the impact of global climate change by collecting carbon dioxide (from the atmosphere) and safely sequestering it beneath the subsurface. CCS is a technology aimed at combatting climate change by capturing carbon dioxide emissions from sources like power plants and industrial processes, preventing their release into the atmosphere. Instead, the captured CO_2 is stored underground, with the objective of keeping it there indefinitely (as depicted in Figure 1-1). CCS serves as a transitional solution, enabling the continued utilization of fossil fuels in electricity generation and industry until more environmentally friendly alternatives become more feasible. Additionally, CCS may prove essential in achieving the negative CO_2 emissions necessary to meet the climate goals of limiting global warming to 1.5°C and 2°C. To significantly reduce carbon emissions through CCS, substantial quantities of CO_2 must be captured and securely stored (Bandilla, 2020).
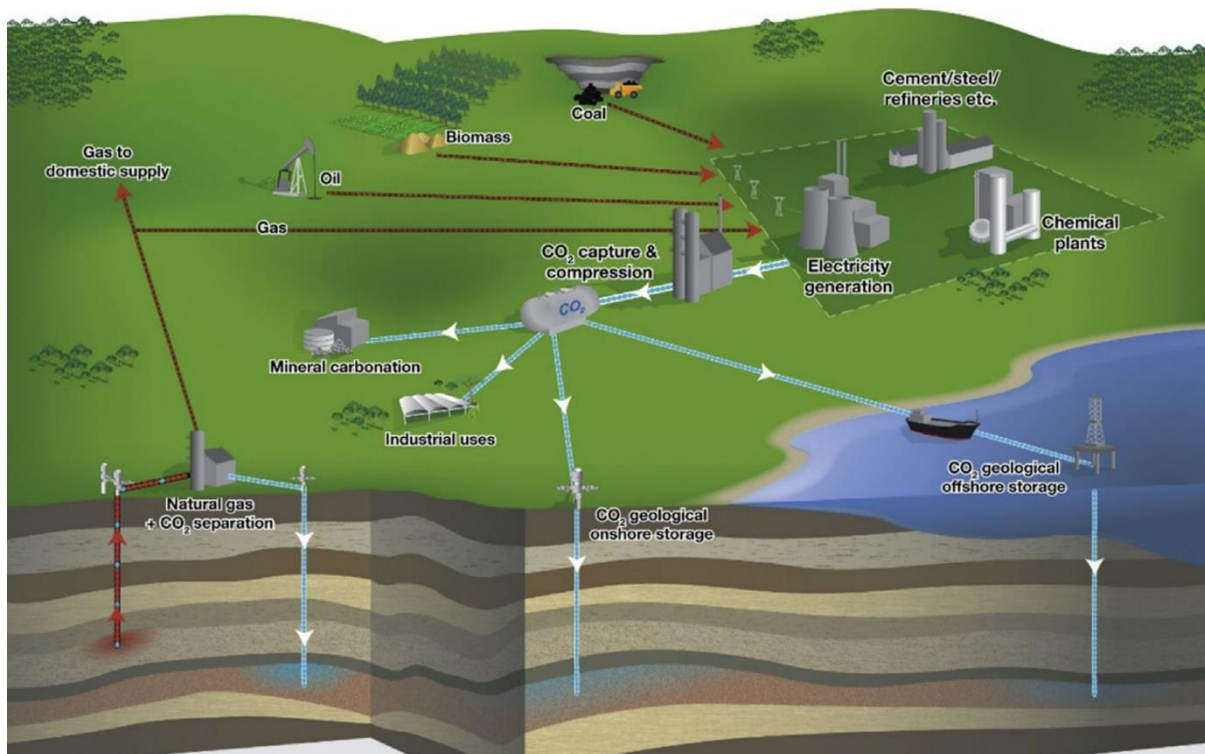
Figure 1-1 Visual representation outlining the concept of carbon capture and storage (Bandilla, 2020).

1.1.3   Challenges posed by salt precipitation

The phenomenon of salt precipitation induced by brine vaporization during dry CO_2 injection presents significant challenges for the feasibility and efficiency of CCS in saline aquifers. As undersaturated CO_2, which refers to a condition where the concentration of dissolved CO_2 in a solution is below the maximum amount that can be dissolved at a given temperature and pressure, is injected into the formation, the evaporation of formation water leads to the accumulation of dissolved salts, eventually exceeding their solubility limit and precipitating out of the aqueous phase (Ott et al., 2015). This process alters the porosity and permeability of the formation, impacting injectivity and storage capacity. Field observations and laboratory experiments (Miri & Hellevang, 2016) have highlighted the detrimental effects of salt precipitation on reservoir properties, including substantial reductions in permeability. However, conflicting reports on the impact of salt precipitation (Abbasi et al., 2022) on injectivity underscore the complexity of the phenomenon. The lack of a comprehensive physical model and inconsistencies between experimental results and numerical simulations further exacerbate the

challenge of predicting and mitigating salt precipitation. Addressing these challenges requires interdisciplinary research efforts to develop accurate predictive models, improve experimental design, and explore mitigation strategies to ensure the success of CCS projects in saline aquifers (Miri & Hellevang, 2016).

1.1.4   Challenges posed by hydrate formation

Under the right thermodynamic conditions, CO_2 injected into depleted gas reservoirs can combine with water to form hydrates. Hydrates resemble ice crystals and can clog the reservoir or injection wells, causing injection to slow down or come to a halt. In order for CCS to become feasible, this process must be managed. One of the major challenges lies in comprehending the intricate thermodynamics and kinetics that govern these exchange reactions. The behavior of hydrates under various temperature and pressure conditions, as well as their interactions with different gas compositions, demand a deeper understanding. The mechanics of hydrate formation needs to be understood, as well as the parameters that lead to hydrate dissociation. Additionally, factors such as grain size of the rock (Bhattacharjee et al., 2015), permeability, and the nature of the surrounding medium influence the exchange rates and overall efficiency of the process, adding further layers of complexity. Developing accurate reservoir simulation models to predict and optimize these processes remains a significant hurdle, requiring precise data and thorough validation. While field trials have shown promise in showcasing the feasibility CO_2 storage in saline aquifers, sustaining large-scale, prolonged storage remains a futuristic goal, necessitating continued research, innovation, and technological advancements to overcome these formidable challenges (Bhattacharjee et al., 2015).

1.2   Research objectives and questions

This thesis research is centered around two (chemical and physical) phenomena - CO_2 hydrates and salt precipitation - with a specific focus on their behavior in microfluidic systems under controlled temperature conditions. The primary objective of this research is to achieve a comprehensive understanding of the kinetics, formation mechanisms, spatial distribution, and structural aspects of CO_2 hydrates and salt precipitation. To achieve this, an experimental setup is employed to obtain data for future simulations. The experimental setup entails working with microfluidic models and a microscope to enable precise observation and documentation of the reactions. The experiment for the hydrate formation involves injecting water and CO_2, into these microfluidic systems, which are cooled by a cooling bath. The salt dry-out experiment for the salt precipitation involves injecting a brine solution and CO_2 into a microfluidic chip, which is heated by a heating bath. During both experiments, images of the hydrate formation and salt precipitation are captured regularly. These images serve as crucial visual data for analysis and verification.

The investigation into salt precipitation involves studying various microfluidic models, each with different patterns and structures, to explore the kinetics of salt precipitation, their locations within the microchannels, and their morphological characteristics. For CO_2 hydrate formation, the research is conducted using one variant of the microfluidic model. Subsequently, the acquired images are subjected to rigorous analysis, applying established theoretical frameworks to interpret and elucidate the observed phenomena. The experiments are repeated multiple times with different chip permeabilities to observe their impact on hydrate formation and salt precipitation.

1.2.1 Research questions

What are the mechanisms governing salt precipitation observed in heated microfluidic systems?
Sub-questions:
- How do these mechanisms affect the spatial distribution of salt precipitation?
- What is the impact of rock pattern and pore geometry on salt precipitation?
- How does the heterogeneity affect dynamics of salt precipitation?
- How can the insights gained from this study be utilized to enhance the efficiency of CCS technologies?

What factors influence the growth of CO_2 hydrates in microfluidic systems?
Sub-questions:
- How does this kinetics elucidate the mechanisms of hydrate formation and dissociation?
- What types of hydrate morphologies can be observed?
- How can the insights gained from this study be utilized to enhance the efficiency of CCS technologies?

1.3 Report structure

The report is divided into 6 chapters, after this introduction. Chapter 2 consists of the literature review into the theory and previous works on first salt dry-out, in section 2.1, then hydrate in section 2.2. Following this, Chapter 3 contains the methodology of the executed experiments and the data and image processing techniques. The results of these experiments are then given and analyzed in Chapters 4 and 5. Finally, the research questions of this thesis are discussed in Chapter 6, and conclusions followed by recommendations for future work in Chapter 7. In the Appendix, relevant data and results from the experiments are provided.

2   Background

2.1   Salt dry-out

2.1.1   Definition of salt dry-out

Subsurface porous media, like saline aquifers, oil, and gas reservoirs naturally contain dissolved mineral salts. The crystallization of these salts within the pores can significantly reduce the permeability of underground reservoirs. This decreased permeability leads to challenges such as decreased injectivity and storage potential in CO_2 sequestration, as well as reduced production from hydrocarbon reservoirs. Injecting CO_2 into saline water exacerbates this by causing formation dry-out and solid precipitation, further reducing porosity, permeability, and injectivity, as the increased salt concentration from formation dry-out leads to solid salt precipitation, blocking pores and channels (Ho & Tsai, 2020). The growth of salt crystals within porous media is driven by complex interactions between the chemical composition of the brine and the physical properties of the pore spaces. Factors such as ion concentration, temperature, pressure, and the availability of nucleation sites play a significant role in determining the rate and shape of crystal growth (Espinosa-Marzal & Scherer, 2010). Understanding these mechanisms is essential for predicting and managing the effects of salt precipitation in subsurface environments.

2.1.2   Salt precipitation

Salt precipitation refers to the chemical process where water is removed from a salt solution or hydrate salt, leaving crystalline salts behind. In this study, the phenomena occurring when a porous medium becomes fully saturated with brine and is subsequently exposed to CO_2 injection is investigated. Following CO_2 injection into the aquifer, three distinct zones emerge: a zone undergoing drying-out, a zone characterized by unsaturated two-phase flow, and a saturated zone, all depicted in Figure 2-2. Salt precipitation can occur through diverse mechanisms, including water evaporation, capillary-driven backflow, and salt diffusion. Salt diffusion refers to the movement of salt ions from areas of higher concentration to areas of lower concentration within a solvent, driven by the concentration gradient (Norouzi et al., 2021). There is a hypothesis suggesting that brine backflow, triggered by capillary pressure, is a pivotal factor in salt precipitation (Miri & Hellevang, 2016). Figure 2-1 shows an illustration of CO_2 injection drying front and capillary-driven brine backflow. Several factors can affect the extent and rate of salt precipitation in porous media. These include the concentration of dissolved salts in the brine, the rate (volume) of (dry) CO_2 injection, the temperature and pressure conditions within the reservoir, and the properties of the porous medium (Cerasi et al., 2021).
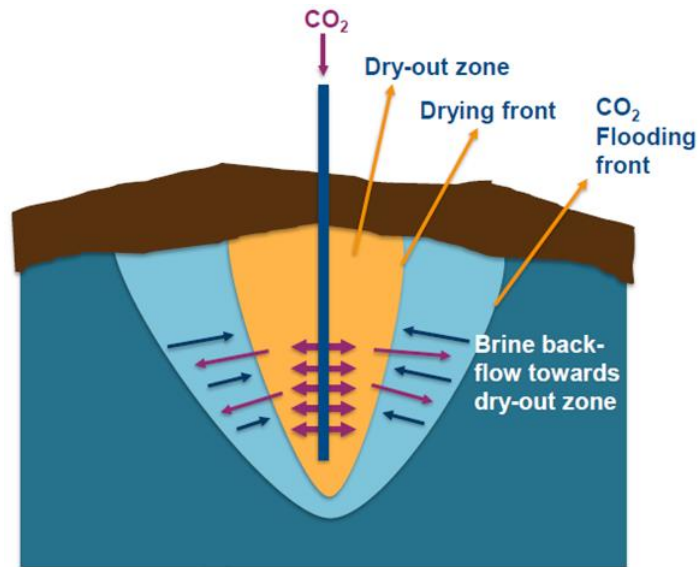
Figure 2-1 Sketch showing injected CO_2 drying front and capillary brine backflow (Cerasi et al., 2021)

2.1.2.1   Capillary-driven backflow

Due to surface energy effects and the hydrophilic properties of salt, brine is drawn into salt clusters, which grow within the CO_2 stream. These clusters, consisting of micrometer-sized crystals in the gaseous phase, create a micro-porous medium with significant capillary action (Masoudi, 2021). This allows the brine to be strongly absorbed over considerable distances, via capillary-connected water films, towards the evaporation front. The brine absorbed within the salt structure is significantly thinner compared to brine trapped in traditionally filled pores, as it forms a thin film on the surfaces. Owning to its high surface area to volume ratio, it quickly becomes highly supersaturated. This leads to a rapid nucleation rate and the formation of additional salt crystals (Miri et al., 2015).
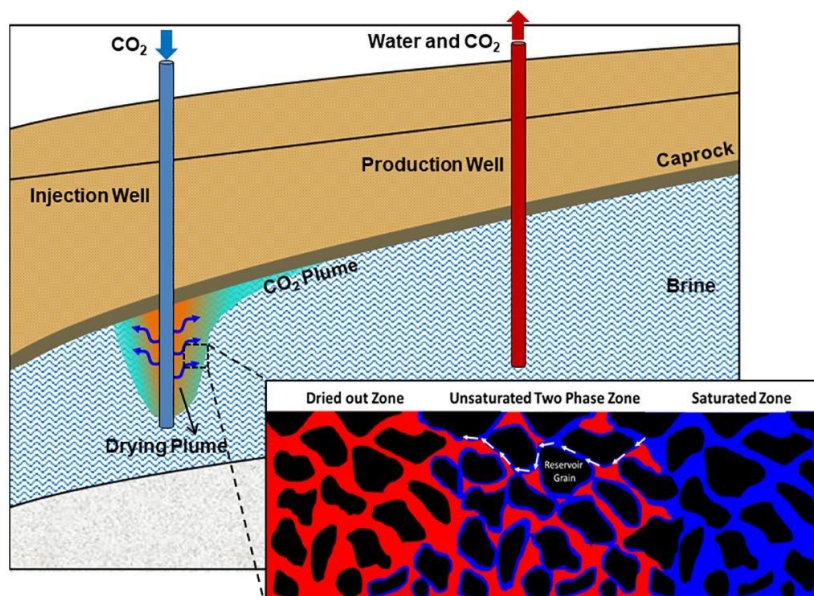
Figure 2-2 Zoomed out schematic diagram depicting salt precipitation and capillary flow during CO_2 injection in gas reservoirs (Norouzi et al., 2021)

The capillary pressure can be found by utilizing the Young-Laplace equation (2.1). This phenomenon can only occur when the capillary pressure P_c exceeds the injection pressure P_{inj} (Lyu et al., 2021) (Arendt et al., 2004).

$$P_c = P_{CO_2} - P_w = \frac{2 \cdot \gamma_{w,CO_2} \cdot cos\theta}{R} \tag{2.1}$$

Wherein γ_{w,CO_2} equals the water-CO_2 interfacial tension in N/m, θ is the contact angle and R is the effective radius of the canal. An alternative, simpler method to check the dominance of capillary action is by calculating the capillary number:

$$N_C = \frac{\mu v}{\gamma_{w,CO_2}} \tag{2.2}$$

This dimensionless quantity shows the balance between the viscous drag forces and surface tension. This number needs to be smaller than 10^{-5} in order for capillary forces to dominate (Yan et al., 2024). The variable μ represents the viscosity of the fluid, in this case CO_2. At a temperature of $50°C$ this is equal to $\mu_{CO_2} = 1.61 * 10^{-5}\ Pa \cdot s$ (The Engineering ToolBox, 2024). v represents the characteristic velocity, which is dependent on the flow rate. The interfacial tension is a material property, showing the bonding power of two substances under certain conditions. However, it is difficult to obtain a reliable value for this property of brine. (Sokama-Neuyam et al., 2020) found a value of $68\ mN/m$ for pure water at 1 bar and 50 °C, and $28\ mN/m$ at supercritical conditions. In (Yan et al., 2024) it is stated that the contact angle can be derived from the wettability of the reservoir. A 'water-wet' reservoir corresponds to contact angles of less than 75°, while an 'non-water-wet' reservoir corresponds to contact angles of more than 105°. All contact angles in between can be found in 'intermediate-wet' reservoirs. However, a high salinity can have a large effect leading to a possible increase in over 20° due to the free natrium ions (Yan et al., 2024).

The experiments are conducted in a microfluidic chip, which allow for the capillary number derivation to be expressed in known variables, together with the assumed values described above (Yan et al., 2024).

$$N_c = \frac{wL}{(w + h)} \frac{6 \cdot \mu \cdot q}{\gamma_{w,CO_2} \cdot cos\theta} \tag{2.3}$$

In this equation, h and L are the respective height and length of the microfluidic chip in m, while q equals the injection rate in m/s and w is the pore throat size in m. This calculation was done for every experiment to check validity. The results are shown in appendix C. In all experiments, capillary dominance was found and thus validity was shown.

2.2   Hydrates

2.2.1   Definition of hydrate

Gaseous hydrates are crystalline solid compounds formed by enclosing gas molecules within cages composed water molecules, connected by strong hydrogen bonds. Captured gas molecules such as CO_2, CH_4, and N_2 are known as "guest molecules," and water molecules forming the hydrate structure are known as "host molecules." Gaseous hydrates are non-stoichiometric solids that resemble ice (or snow) in appearance but are structurally quite different. Water molecules within the hydrate structure form hydrogen bonds with each other, creating hollow (cage-like) spaces and instability. At specific temperatures and pressures, and in the presence of gas molecules that are of a similar size to the cages, hydrates are formed (Gambelli & Rossi, 2021). Hydrates come in three structures: Structure I, II and H as shown in Figure 2-3. The difference in these structures is the way the "cages" are built, as so what gas can be captured. The simplest type "cage" is a pentagonal dodecahedron which is found in all three structures. The formation of hydrate is an exothermic process, meaning it releases heat, while hydrate dissociation is an endothermic process, meaning it absorbs heat.
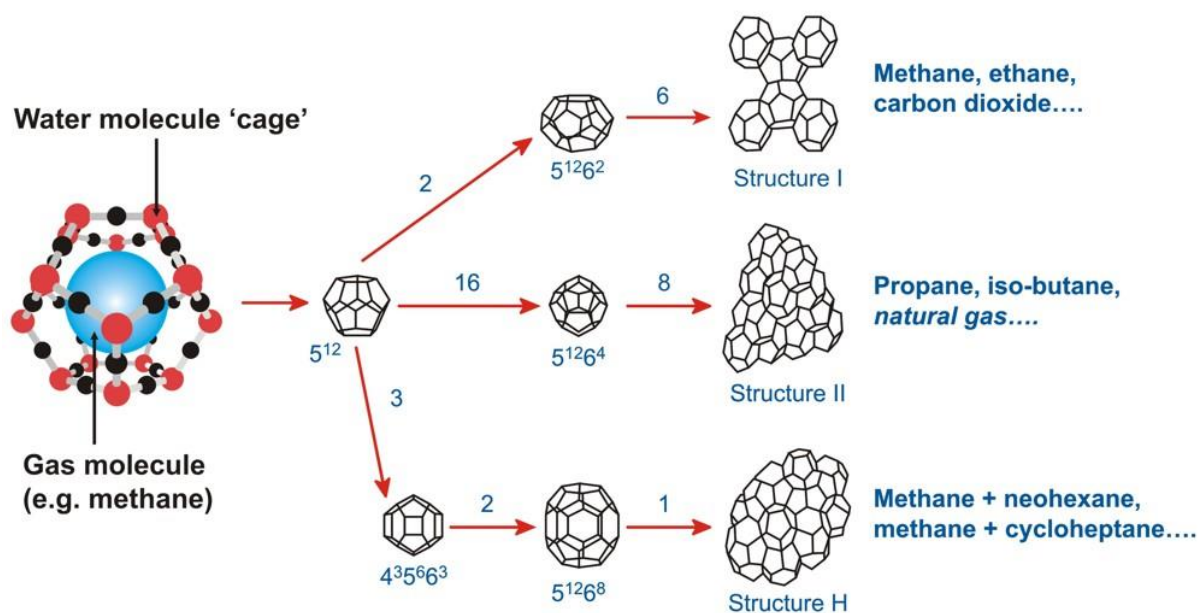
Figure 2-3 Schematic of hydrate structure type (Centre for Gas Hydrate Research, 2023). The numbers represent the number of faces and vertices per face with A^n as A as the vertices per face and n as the number of faces with that shape.

2.2.2   Hydrate nucleation

Hydrate nucleation is considered a microscopic phenomenon within the context of hydrate formation, involving tens to thousands of molecules. During this process, hydrate nuclei are formed, constituting small, labile clusters composed of gas and water molecules. These clusters undergo growth and dispersion while continuously collecting gas until their size and concentration reach the critical point for hydrate crystal formation, indicated as point B in Figure 2-4 (Vysniauskas & Bishnoi, 1982). Initially, gas is absorbed into water until point A, then the nucleation process occurs from point A to point B, and finally, the growth process takes place from point B to its endpoint.
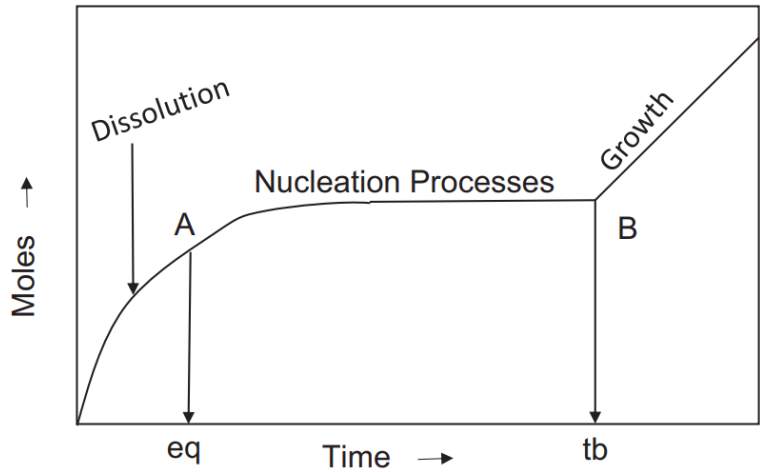
Figure 2-4 Typical gas consumption during hydrate formation (Sun & Kang, 2016).

2.2.3   Hydrate formation

Hydrate formation, subsequent to the critical nucleation step, transitions into a continuous crystal growth phase, as depicted in Figure 2-5. In this phase, the agglomeration of gas hydrate crystals takes place. Central to this process is the mass transport of gas molecules to the hydrate surface, which plays a pivotal role in facilitating crystal growth. Furthermore, the growth kinetics and the heat transfer characteristics of the exothermic growth process from the crystal surface to the surrounding solution are key considerations. Many studies have investigated hydrate formation kinetics yet the dominant phenomenon among these factors still remains ambiguous, highlighting the complex nature of hydrate formation. Understanding the interplay of mass transport, growth kinetics, and heat transfer is vital for gaining insights into the mechanisms underlying hydrate crystal growth.
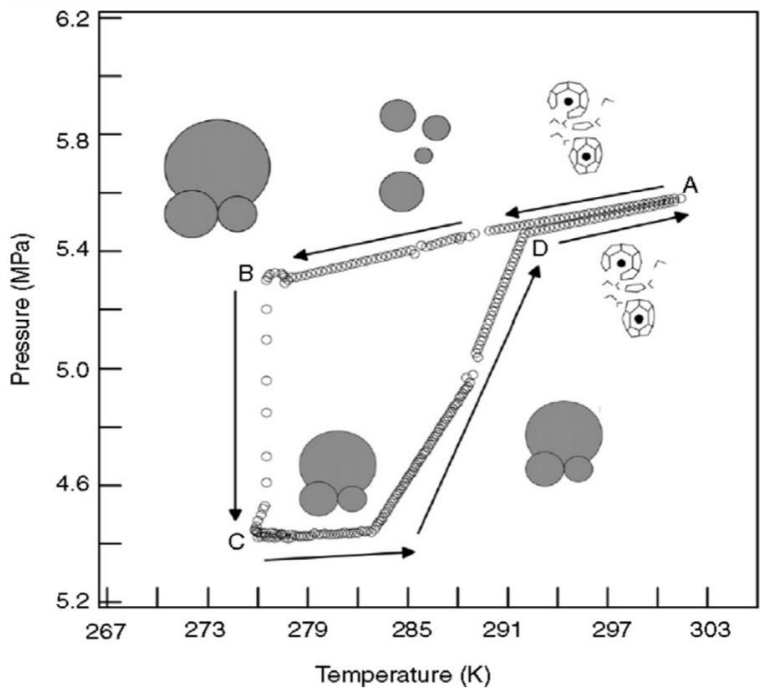
Figure 2-5 Hydrate cluster growth mechanism imposed on a pressure–temperature trace (Sun & Kang, 2016).

2.2.4   Joule-Thompson cooling

An important phenomenon to consider when studying hydrate formation in the context of CCS is the Joule-Thompson cooling effect (Chesnokov et al., 2024). When CO_2 is injected into the reservoir, it moves from the high pressure environment on the surface (for example 100 Bar) to the 'low' pressure environment in the reservoir (for example 30 bar). This causes the CO_2 to rapidly expand and cool to freezing temperatures, which can cause hydrate formation in the reservoir. This effect is shown in Figure 2-6, by the arrow leading from state A to D. Theoretically, by heating the CO_2 gas before injection, enthalpy levels can be increased (point B). This would also lead to a higher enthalpy after injection (point C), and thus fewer hydrates.
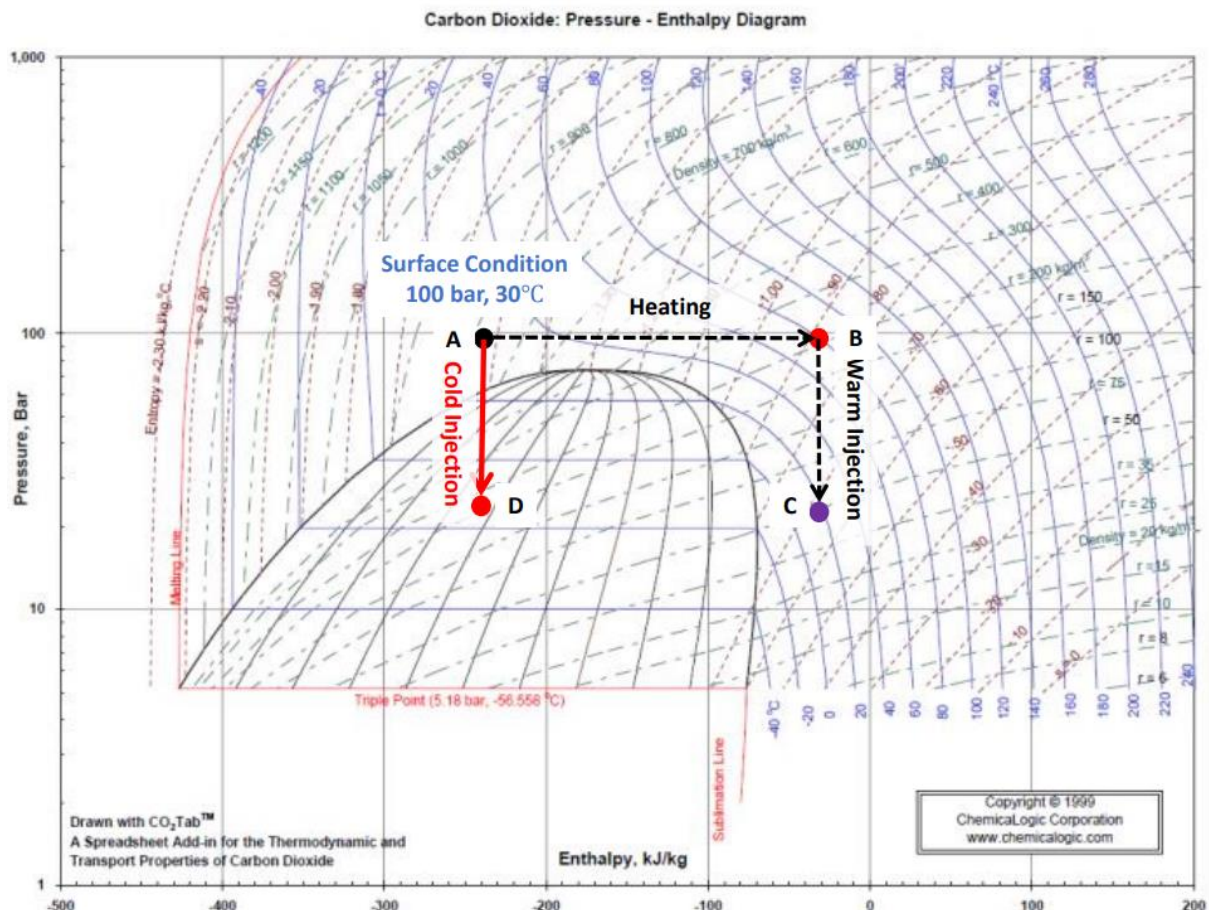
Figure 2-6 Pressure-Enthalpy diagram of CO_2 with states during injection given (assuming no heat transfer) (Chesnokov et al., 2024)

2.2.5   Hydrate dissociation

As discussed in section 1.1.4, hydrate dissociation is a fundamental process essential for the removal of hydrate crystals that often obstruct pipelines within the oil and gas industry. This dissociation process is fueled by the difference between the equilibrium chemical potential and the vapor chemical potential of the gas phase. Notably, hydrate dissociation is an endothermic process, signifying that it requires an input of external heat to effectively eliminate the hydrate crystals. This thermal energy disrupts the hydrogen bonds between water molecules and weakens the van der Waals interactions between the host and guest molecules, ultimately leading to the decomposition of gas hydrate into water and gas molecules. The ability to induce this dissociation process through controlled heat

application is of paramount importance in the prevention and mitigation of pipeline blockages caused by gas hydrate formation in the oil and gas sector (Makwashi et al., 2018).

Various methods are available for inducing dissociation, including depressurization, inhibitor injection, and thermal injection, as depicted in Figure 2-7. Out of these three commonly employed techniques, depressurization is considered the most cost-effective (Makogon, 1997). Consequently, the majority of research has focused on reducing pressure as the dissociation method. Nonetheless, relying solely on depressurization for dissociation is not ideal due to the risk of secondary hydrate formation and ice crystallization during the process.
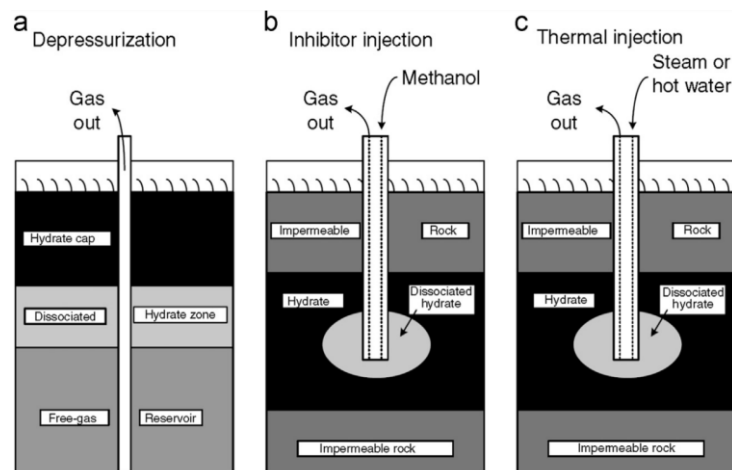
Figure 2-7 The three common ways of hydrate dissociation (Makogon, 1997).

2.2.6   Hydrate morphology

Hydrates can form in many shapes. According to literature, this is due to different geological environments where hydrates can form and achieve different occurrence patterns and distribution morphologies. Based on the relationship between hydrates and skeleton grains in hydrate-bearing sediments, the occurrence patterns of hydrates in porous media can be roughly divided into five main types (Ren et al., 2020), as shown in Figure 2-8.

a) Pore-filling hydrate, which grows freely in the center of the pore without contacting any framework particles;

b) Load-bearing hydrate, which grows in the center of the pore, forms point contact with adjacent framework grains, and bridges them together, becoming part of the framework and providing stability to the sediment;

c) Grain-cementing hydrate, which cements the framework grains together;

d) Grain-coating hydrate, which grows uniformly on and around the surface of the skeleton grains, and eventually wraps the skeleton grains;

e) Patchy hydrate, which is condensed into larger crystals from pore-filling hydrate due to Ostwald ripening. Patchy hydrate is locally clustered and scattered in the pores of sediments.

These five hydrate occurrence patterns belong to the pore-invasive type, which mainly occurs in coarse-grained sediments and in small amounts in fine-grained sediments (Ren et al., 2020). The

occurrence patterns of grain-cementing, load-bearing, and patchy hydrates are relatively rare in hydrate-bearing sediments.
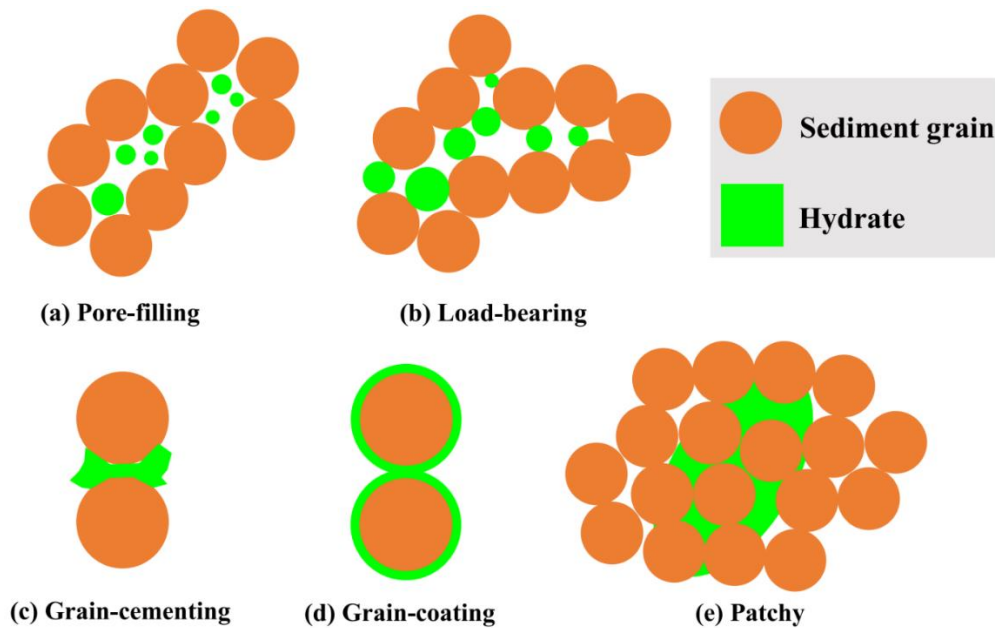
Figure 2-8 Schematic diagram of hydrate occurrence morphologies in hydrate-bearing sediments at pore-scale (Xu et al., 2021)

2.2.7   Impact of salinity on hydrate formation

The impact of salinity on hydrate formation has been a subject of recent research interest. (Gauteplass et al., 2018) delved into the influence of, among others, salinity on the sealing capacity of CO_2 hydrates in consolidated sandstone. Interestingly, their findings indicated that increasing temperature and salinity negatively affected the formation time of CO_2 hydrate seals. In contrast, the impact of flow rate appeared insignificant at lower flow rates. However, it's worth noting that some studies (Yang et al., 2016) have reported no discernible effect of salinity on CO_2 hydrate induction time within a range (0-3.03wt%) of salt concentration in porous media. These findings highlight the complex interplay between salinity and hydrate formation, with potential implications for both energy and environmental applications (Gauteplass et al., 2020).

The study by (Gauteplass et al., 2018) investigated the impact of temperature and brine salinity on hydrate formation and pore plugging in sandstone reservoirs. In their experiments, liquid CO_2 was injected into fully brine-saturated sandstones at different conditions: 3.5 wt% salinity and 4°C, 3.5 wt% salinity and 6°C, and 5.0 wt% salinity and 4°C. In all three cases, hydrates formed and completely blocked the core samples. Notably, increasing the temperature from 4°C to 6°C delayed hydrate formation when 2.5 PV of CO_2 was injected. Similarly, increasing the brine salinity from 3.5 wt% to 5.0 wt% NaCl delayed hydrate formation when 3.5 PV of CO_2 was injected. The pressure gradient across the pore space increased as hydrates grew, with a similar slope in all experiments. The study highlighted that parameters like water availability and heat flow rate significantly influence CO_2 hydrate growth, and increasing salinity and temperature can impact the induction time but have a lesser effect on the hydrate growth rate, particularly in flow-induced CO_2 hydrates within sandstone pores. This effect is shown in Figure 2-9. One can see that the slope of the pressure gradient is very similar in all cases, suggesting equal hydrate growth rate. However, the PV fraction injection before hydrate formation is very different for the three cases.

Furthermore, the research demonstrated that temperature and salinity alterations affect various aspects of hydrate growth in sediments. Higher reservoir temperatures decrease CO_2 solubility in water, potentially affecting hydrate nucleation mechanisms from the aqueous phase. Additionally, initial brine salinity affects the conversion of water to hydrate structure, with increased salinity leading to higher final water volume and reduced hydrate volume. This information sheds light on the complex relationship between temperature, salinity, and CO_2 hydrate formation, offering valuable insights for understanding and managing hydrate-related processes in subsurface environments.
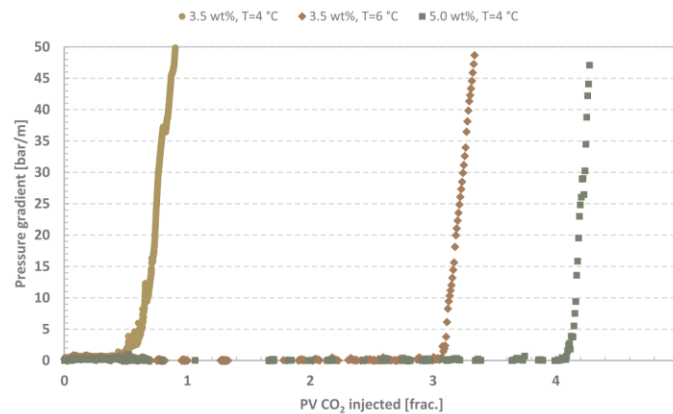
Figure 2-9 Pressure gradients at three different conditions (Gauteplass et al., Hydrate seal formation during laboratory CO2 injection in a cold aquifer, 2018).

2.2.8   Impact of impurities on hydrate formation

The impact of impurities on hydrate formation is a crucial consideration when injecting anthropogenic CO_2 into geological formations. These impurities, which may include CH_4, N_2, and amine residues, can vary depending on the specific carbon capture technology employed. Impurities have the potential to modify the thermodynamic characteristics and phase equilibria of the involved fluids. Numerical simulations have highlighted the significance of this phenomenon, demonstrating that the presence of just 5 mol% CH_4 in the injected CO_2 can extend the Gas Hydrate Stability Zone (GHSZ) by nearly 2°C at a pore pressure of 70 bar (Gauteplass et al., 2018). Figure 2-10 shows this GHSZ for four different gasses. This underscores the importance of understanding and managing impurities when assessing the feasibility and safety of CO_2 injection strategies (Gauteplass et al., 2020).
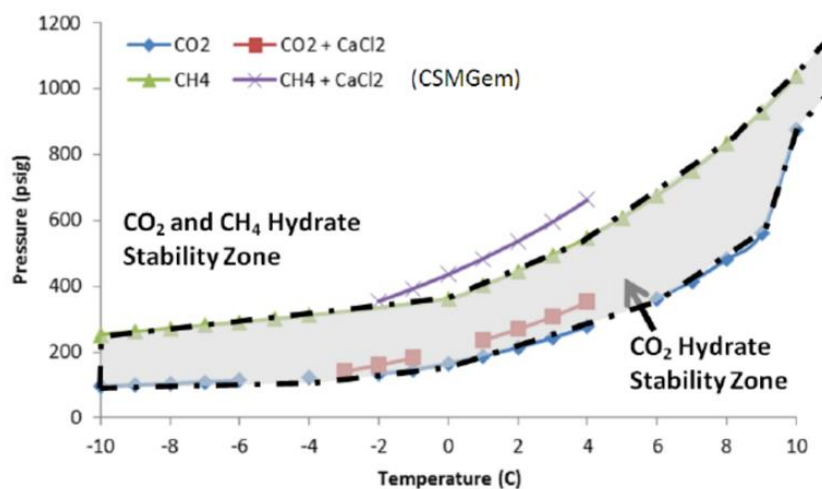
Figure 2-10 Graph shown the hydrate stability zone of 4 different gasses

3 Methodology

3.1 Micromodels

The micromodels, or micro-fluidic chips, used are thin wafers of permeable material. They allow for close study of physical processes that normally occur inside rock formations on pore levels. Micromodels have been used extensively in other papers to study salt dry-out and hydrate formation characteristics at pore levels. Notable studies include (Kim et al., 2013), who researched pore-scale salt precipitation dynamics during CO_2 sequestration, and (Hauge et al., 2016), who investigated pore-level hydrate formation mechanisms using realistic rock structures in high-pressure silicon micromodels. The thinness of micromodels allows for visual tracking of flow and/or crystallization processes, thus not relying on expensive imaging techniques such as CT scanning. The exact properties of the microfluidic chips used are given in the sections corresponding to the two experiments.

A critical aspect of the experimental setups is the requirement for accurate temperature control to simulate the conditions prevalent in boreholes and gas reservoirs. Therefore, all experimental procedures will be conducted within a controlled environment. The temperature settings within the cold box for hydrate formation will be maintained at levels of 0.5°C to 1°C to replicate the frigid conditions essential for CO_2 hydrate formation. The temperature setting for the heating bath of the salt dry-out experiments is set around 50°C. This ensures that every element, including the experimental setup, operates within the specified temperature range. Additionally, the pressure is also important and is measured by multiple sensors across the setup.

3.1.1 Salt dry-out experimental setup

For the salt dry-out experiments, 5 microfluidic chips were utilized, manufactured by Micronit. Among these, 3 microfluidic chips feature a homogeneous pattern, while 2 microfluidic chips exhibit a heterogeneous pattern. The three homogeneous microfluidic chips (Figure 3-1 to Figure 3-3) are characterized by the average pore sizes as 'large', 'medium' and 'small'. The two heterogeneous designs (Figure 3-4 and Figure 3-5) have a mix of two different pore sizes: one with a 50% large pore size and 50% small pore size part, which will be discussed in this paragraph, and the other with a 50% medium pore size and 50% small pore size part. The network designs of these chips are depicted in Figure 3-1 until Figure 3-5. For a clear overview of the pore distribution for these microfluidic chips, see Appendix A.3, The calculations for the pore size of these microfluidic chips are based on a previous calculation made by (Yan et al., 2024).

All these microfluidic chips maintain a porosity of 0.4 and are equipped with both 2 inlet holes and 2 outlet holes. The pattern size of the microfluidic chips is 2 cm by 1 cm, with a microfluidic chip height of 5 micrometers. The permeability varies among the microfluidic chips and is calculated during experimentation, which will be further discussed in paragraph 4.1.
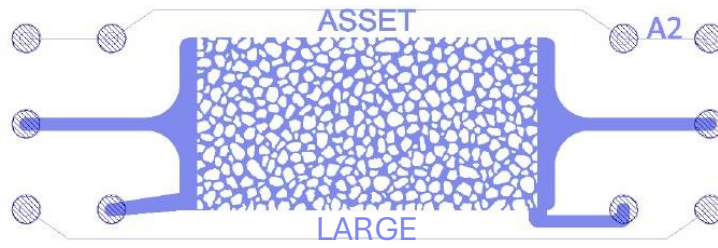
Figure 3-1 Large pore size microfluidic chip
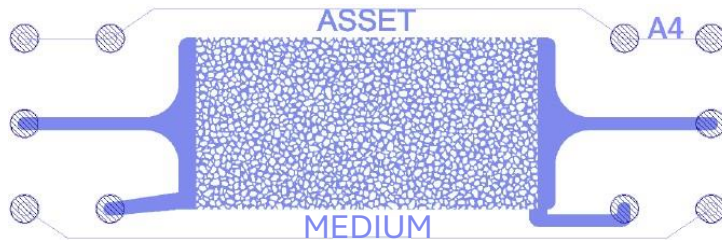
Figure 3-2 medium pore size microfluidic chip
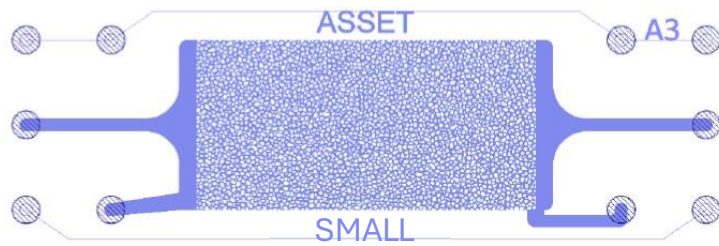
Figure 3-3 Small pore size microfluidic chip
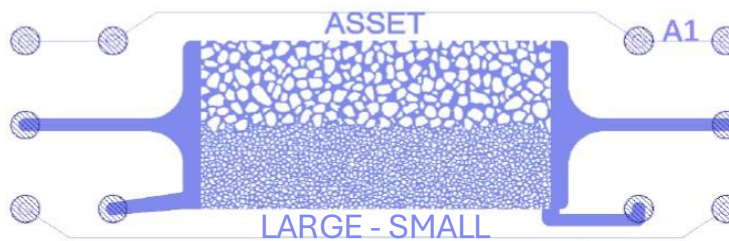
Figure 3-4 Large – Small pore size microfluidic chip
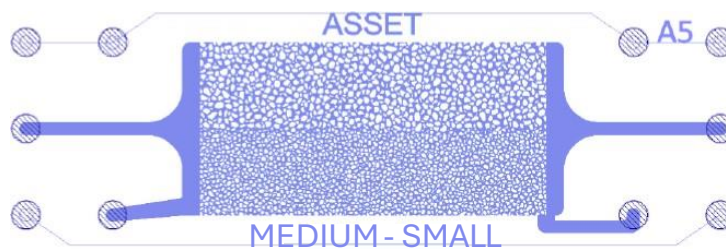
Figure 3-5 Medium – Small pore size microfluidic chip

The chip holder employed for the salt dry-out experiments is the low-pressure Fluidic Connect Pro chip holder, also designed by Micronit. Micronit describes this holder as a versatile tool designed to facilitate fast, effortless, and reliable fluidic connections. Its design incorporates replaceable inserts, ensuring future compatibility and longevity (Micronit, n.d.). Sealing solutions are integrated to prevent microfluidic chip cracking, ensuring consistent performance. Moreover, its design allows for a large microfluidic chip view area, enhancing visibility during experiments. For visual reference, please consult Figure 3-6.

Figure 3-6 Low pressure chip holder (Micronit, n.d.)

The complete test setup for the salt dry-out experiments is shown in Figure 3-7. At the core of the setup lies the chip holder housing the microfluidic chip. CO_2 is injected into the microfluidic chip from the left-middle port, with the flow rate regulated by the mass flow controller (MFC). The right-middle port is linked to a Quizix pump. Both bottom ports feature tubes connected to effluent for saturating and injecting the microfluidic chip with brine or CO_2. This entire process is monitored by a camera suspended above, capturing a photo every two minutes.
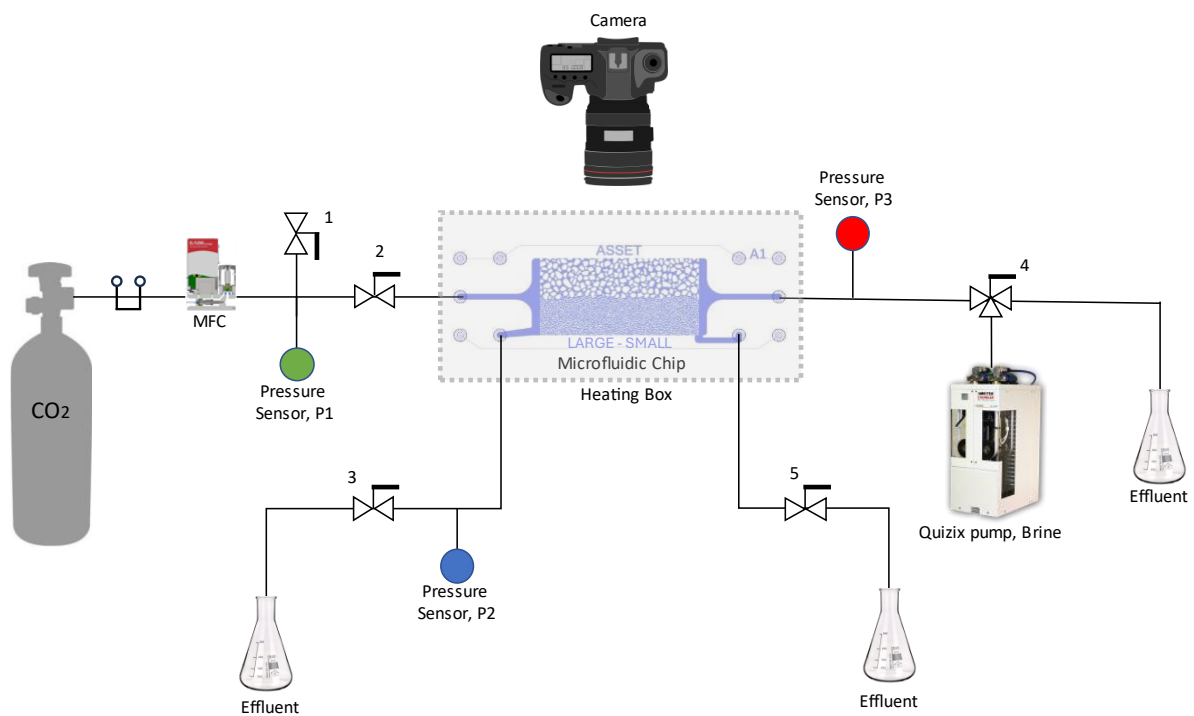
Figure 3-7 Schematic of the micromodel set-up used to conduct salt dry-out experiments.

As shown, the microfluidic chip is placed in a heating box. It is expected that the drying process is faster when compared to previous studies done without the heating box because higher temperatures accelerate the drying process, which aids in studying the behavior of salt precipitates over a shorter time span. Additionally, the temperature condition is controllable: the heating box allows the temperature to be kept consistent and even, which is essential to ensure controlled and reproducible evaporation of the water from the micromodel. Next to this, a heating box serves also a simulation of natural conditions as temperatures in the subsurface can also reach 50°C. The emulation of subsurface conditions is much more realistic, with the heating box aiding in simulating the elevated temperatures often found in underground formations.

3.1.2 Salt dry-out experimental procedure

During the experiments, the outlined steps in Figure 3-8 are followed to explore salt precipitation behavior within a microfluidic system. The main focus is on investigating the effects of the microfluidic chip's pore size on CO_2, brine and salt crystal saturation, leading to a comprehensive understanding of salt behavior under varying conditions. The procedure is structured to ensure precision and accuracy in each experimental phase.

Setup Preparation	→	CO2 Saturation	→	Brine Saturation	→	CO2 Injection	→	Cleaning Microfluidic Chip

Figure 3-8 Flowchart of the steps taken during the salt dry-out experiment.

1. Setup preparation:

Prior to fluid injection, meticulous preparation is essential. This involves cleaning the microfluidic chip with demi water, positioning the microfluidic chip on the stage, and configuring the imaging settings. Additional steps include preparing a brine solution, verifying system connections, and commencing camera recording. Leak testing with the Snoop, a soap-water solution, and generating an Excel file for documentation further contribute to the experimental setup's reliability and repeatability.

2. CO_2 saturation:

A dedicated folder for CO_2 saturation images is created, and valve adjustments are made to facilitate effluent flow. CO_2 is carefully injected with specified flow rates, ensuring the complete saturation of the microchip. This is done by opening closing valves 3 and 4 and opening valves 2 and 5. Using the MFC, the flow rate is set to 0.7 ml/min for around 10 minutes. A picture of the fully-saturated chip is taken. After this, the flow rate is set the 0 and all valves are closes.

3. Brine saturation:

Similar to the CO_2 saturation stage, a dedicated folder is created for photos obtained during brine injection. Put the camera to video mode and start recording. Valves 3 and 4 are open, and the pump is set to 0.01 ml/min to start controlled brine saturation. The process continues until the brine reaches the outlet. Photos are taken every two minutes as the flow rate is increased to 0.05 ml/min. The interaction between brine and CO2 is monitored, and the entire chip becomes saturated with brine within a maximum of 30 minutes. Once saturation is complete, valves 3 and 4 are closed, marking the end of this step.

4. CO₂ injection:

A new folder is created for the images of this step. The camera is set to video mode, and the MFC is adjusted to 0.007 ml/min. Based on the speed of the CO_2 in the lines, this value is fine-tuned to expedite the process. As the CO_2 approaches the microfluidic chip, the pressure in the mass flow controller (MFC) is decreased using Valve 1, and recording begins. When the CO_2 reaches the outlet, the camera is switched to photo mode with a 2-minute interval. The system is then allowed to reach complete dry-out, which may take several days.

5. Cleaning microfluidic chip:

Post-experiment, the microchip is carefully removed and subjected to thorough cleaning using a syringe filled with demi water. The cleaned chip undergoes drying in an oven with a vacuum pump. This step ensures the microchip's readiness for subsequent experiments and maintains the integrity of the experimental setup.

3.1.3   Hydrate experimental setup

For the hydrate experiments, the Physical Rock Network Enhanced Oil Recovery (EOR) chip was used. This chip was also designed by the company Micronit. The pattern of this chip can be seen in Figure 3-9. Micronit describes this chip on their website as featuring randomly positioned rock-shaped structures that closely mimic natural rock formations based on real-life images. These structures create interconnected channels and throats. A 2D mask design is available for simulation purposes. According to Micronit, the chip has a permeability in the range of 6.62-7.79 Darcy (Micronit, n.d.) and has a channel depth of 20µm, composed of Borosilicate glass. It is supplied in a black polymer cartridge (polypropylene), with the glass element measuring 45x15x1.8mm.
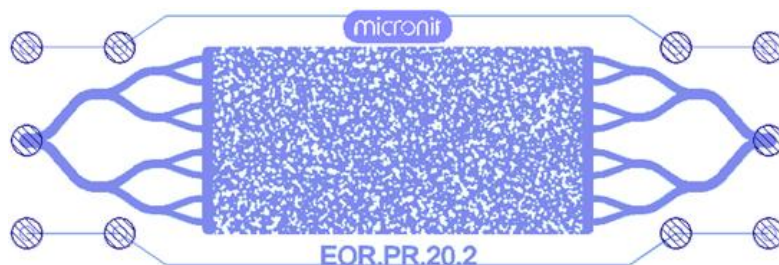
Figure 3-9 Physical rock network microfluidic chip (Micronit, n.d.)

The chip holder employed in the hydrate experiments is the Fluidic Connect 4515. Micronit designed this one specifically for experiments conducted under high pressure conditions (Micronit, n.d.), able to withstand a maximum pressure of 100 bar, with the capacity to handle up to 10 bar for thin bottom chips. In terms of dimensions, the holder measures 80 x 55 x 9.5 mm, crafted from stainless steel 316 for durability and reliability in demanding experimental environments. For visual reference, please consult Figure 3-10.

Figure 3-10 High pressure chip holder (Micronit, n.d.)

The setup for the hydrate experiment closely resembles that of the dry-out experiment. However, there are some notable differences. In the hydrate experiment, the Quizix pump is filled with demi water instead of brine. The microfluidic chip only features two connection points, instead of four. One side is connected to the CO_2 source, while the other side is linked to the Quizix pump. Figure 3-11 illustrates the schematic of the hydrate setup. In contrast to the salt dry-out box, the microfluidic chips is now placed in a cooling box, which closely reproduces the temperature conditions needed for hydrate formation in subsurface reservoirs. The system is capable of reaching -10°C; however, in our experiments the system was cooled down to 1°C.
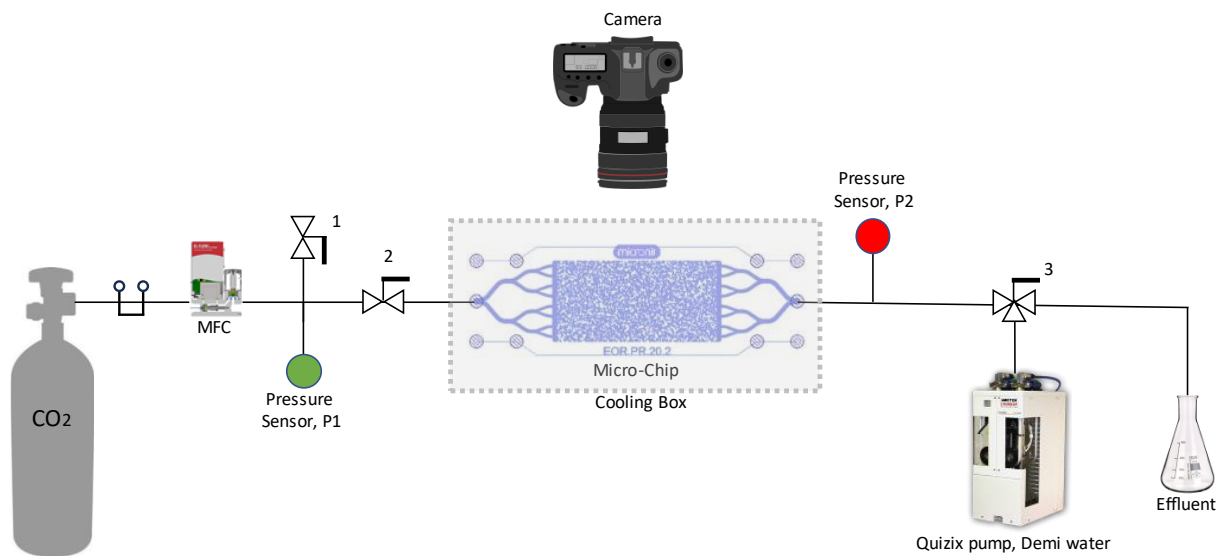
Figure 3-11 Setup hydrate micromodel

3.1.4 Initial development

Initially, nitrogen was used alongside CO_2 as an input, but this did not improve results, so it was later removed. This contrasts with coreflood experiments, also often used in hydrate experiments, where nitrogen is injected during the initial stage of the experiment to reach the desired water saturation in the core. There are several hypotheses why nitrogen seems to inhibit hydrate formation in microfluidic chips. One significant hypothesis is that the micromodel operates as a 2D system instead

of a 3D system. In a 2D system, once a flow path is established, it cannot be broken, preventing crossflow between liquid and gas. Consequently, the liquid cannot move. In a 3D system, crossflow occurs, continuously altering the paths and keeping the water in motion, which could contribute to the system's hydration.

Another hypothesis is that the use of deionized water, which is free of any particles, plays a role. Particles might be necessary as initiation points, but particles inevitably enter the system, making this reason less likely. A third hypothesis concerns the ratio between pore and pore throat in a 2D microfluidic chip. In a 2D microfluidic chip, a pore is a flat structure, and a pore throat has a similar structure but with a smaller channel width. This creates a different volume ratio between pore throat and pore, leading to an inconsistent flow. The flow moves from a small surface area into a large space and slows down. However, the exact impact of particles or inconsistent flow was not investigated further in this thesis.

3.1.5 Hydrate experimental procedure

During the experiments, the outlined steps shown in Figure 3-12, are meticulously followed to explore CO_2 hydrate behavior within a microfluidic system. These steps will be elaborated in paragraphs 1 until 0 below. The primary objectives are to gain critical insights into CO_2 hydrate dynamics, focusing on pore size and the effects of varying conditions. Key aspects of the experiment include ensuring the microfluidic chip's integrity, achieving a leak-free setup, and precise control of critical variables such as pressure, flow rates, and temperature. In Appendix Figure B-1 (in Appendix B.1), a photo of the physical rock chip is shown when it is clean and unused.

| CO₂ Leak Test | → | Demi Water Leak Test | → | Start Hydrate Formation | → | Start Hydrate Dissociation | → | Cleaning Microfluidic Chip |
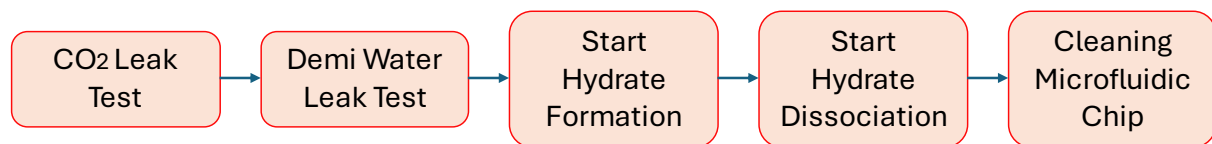
Figure 3-12 Flowchart of the steps taken during the hydrate experiment.

1. CO₂ leak test:

For the CO_2 leak test, the process starts by placing the chip in a water bath for thermal stability. Subsequently, the pressure within the system is gradually increased in steps of 5 bar while closely monitoring for bubbles, particularly around holes and under the chip holder. Any observed bubbles, especially those noticeable, are removed using a needle or similar tool, while tightening the connectors. The process of pressure incrementation and bubble monitoring continues until a pressure of 30 bar is reached. During the leak test, the box is closed to maintain temperature regulation. If the pressure exceeds 30 bar and no leaks are detected, the chip holder is placed on the metal stand, and cleanliness is ensured by cleaning with paper or CO_2. The underside of the chip is checked for cleanliness, as clear and dry surfaces are essential for subsequent photography. Finally, the outside glass of the chip is cleaned with a cotton swab if needed. If the pressure becomes too high at any point during the set-up, valve 1 is briefly opened to reduce it back to 30 bar.

2. Demi water leak test:

For the demi water leak test, the procedure starts by applying 20 bar of pressure to the CO_2 filled microfluidic chip, then increasing to 25 bar, and finally to 30 bar. A wait of 5-10 minutes follows to verify if the pressure remains stable. If stable, the process of retracting the CO_2 begins. Flow is stopped upon observing the interface and resumed when it is nearly in position. Photos are taken at regular intervals. Following the CO_2 leak test, the model is saturated with demi water at a rate of 1000 microliters per minute. Water is injected from right to left by opening valve 2 to the effluent. A temperature sensor is inserted into the microfluidic chip to ensure the temperature remains at 1°C. The box is closed, and the camera is focused. Once the microfluidic chip is fully saturated with water, valve 3 is closed to halt water flow. The system is pressurized by opening valve 2 again and closing the outlet valve. The flow rate is set to 100 microliters per minute, and the pressure is increased. The cooling box is filled with silica gel to reduce moisture and condensation in the box, and the camera is prepared for imaging.

3. Start hydrate formation:

To initiate hydrate formation valve 2 is opened to allow CO_2 flow into the system, and a photo is captured every 5 seconds for documentation. After 15 minutes, the image frequency is reduced to 20 seconds.

To encourage hydrate nucleation, the system is exited using pressure pulses. At random intervals, valve 1 is opened for several tenths of a second. This drops the pressure in the chip to atmospheric levels ($\pm$1bar) in a very short amount of time. After the valve is closed, the system will quickly return to the test pressure($\pm$20bar). When the system has reached steady state, the next step can be initiated.

4. Start hydrate dissociation:

For hydrate dissociation, the flow of CO_2 is stopped using valve 2. The temperature is increased to 5°C, followed by a wait of approximately 15 minutes. Then, the temperature is further increased to 10°C, followed by a wait of an additional 15 minutes to observe the effects on the formed hydrates. The frequency of photography is the same as with the formation step.

5. After injection:

After injection and experimentation, the microchip was carefully removed from the holder and cleaned using demi water via a syringe pump. After being cleaned, the chip is dried in a vacuum oven. This process ensures the chip's readiness for further experiments and preserves the integrity of the experimental setup.

3.2   Imaging techniques and processing

During the execution of these experiments, photos are taken with a Canon EOS camera.

For the dry-out experiment, a gas saturation photo is taken first, in which the chip is fully saturated with CO_2. Then a video is recorded at the beginning of the brine injection. Once the brine has filled from the inlet to the outlet in the chip, the mode is switched to photo, and a photo is taken every 2 minutes until the entire chip is saturated with brine. After this, the mode is switched back to video for the start of the CO_2 injection. When the CO_2 injection has also spread across both sides of the chip, the mode is switched to photo again, and a photo is taken every 2 minutes.

For the hydrate experiments, the procedure is almost the same. First, a CO_2 saturation photo is taken. Then, when the hydrate formation starts, no video is made. Instead, the photo mode is used, taking a photo every 5 seconds because of the high formation rate of the hydrate. This continues for the first ~10-15 minutes. Then the interval is changed to every 20 seconds as the processes slow down. Once the hydrate formation is complete, the dissociation begins. A new folder for the images is created for this, the temperature is increased, and a photo is taken every 5 seconds. Because the hydrate experiment is much shorter overall, it produces approximately the same number of photos, even with the shorter time interval between images.

After the experiments are completed and the photos are collected, they are processed using ImageJ (Schneider et al., 2012). In this program, about 150-200 photos per experiment can be loaded at one time. The steps undertaken are given in appendix C.

3.2.1   Conversion factor

The conversion factor represents the percentage of water molecules that become part of a hydrate. The conversion factor can be calculated with equation 5.2, wherein the hydrate saturation S_H is found using the image processing techniques outlined in the previous paragraph. Two main assumptions are made. The hydrate density is estimated at 804.2 g/l and the molar water/CO_2 ratio at 85/15, resulting from HYDRAFLASH calculations (Aghajanloo et al., 2024). This assumption allows for quantitative comparison of hydrate formation under various circumstances. All other parameters are known.

$$m_H = S_H \cdot PV \cdot \rho_H = conv \cdot n_{H_2O} \left(Mw_{H_2O} + \frac{Mw_{CO_2}}{N_h} \right) \tag{5.2}$$

In this equation, m_h is the mass of the hydrate, S_h the hydrate saturation, PV the total pore volume, ρ_h the hydrate density, *conv* the conversion factor, n_{H_2O} the total number of water moles, Mw the molecular weight, and N_h the number of water molecules per CO_2 molecule.
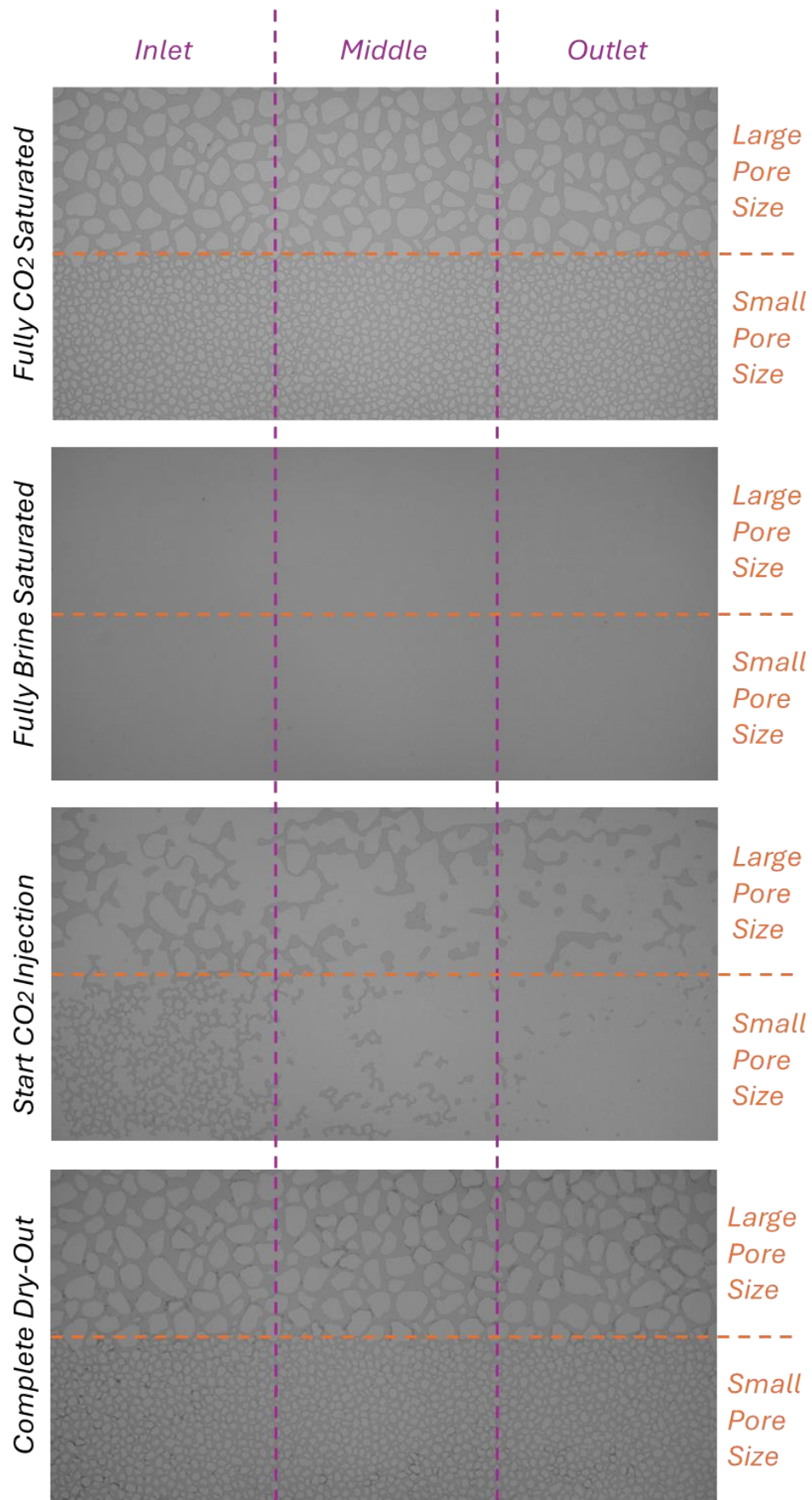
Figure 3-13 The Large-Small chip in the four different stages of the experiment, divided into the regions which are used in the results processing

4 Experimental Results: Salt Dry-Out

4.1 Permeability

The permeability value of each microchip was determined experimentally for use in the calculations. It was found by measuring the pressure drop over the chip at various flow rates, then using Darcy's formula, given in equation 4.1 to calculate the permeability k. Permeability is often used to classify different types of rock, and it was planned to do so in this report as well.

$$q = \frac{kA}{\mu}\frac{P_2 - P_1}{L} \tag{4.1}$$

The measurements; however, lead to unexpected results. As shown in Table 1, all microfluidic chips show very similar measured permeability values. The 'small' microfluidic chip is the most permeable, followed by the 'large', 'medium', 'medium-small', and finally 'large-small' microfluidic chips. This disparity from the expected values (where smaller pores give lower permeability) can be explained due to the nature of the microfluidic chip design itself. The chips are all designed to be 5 μm thick, while previous iterations (such as the physical rock network Figure 3-9) were 20 μm thick. Considering the 'small' microfluidic chip, for example, the median pore size is 93 μm (and the pore size distributions for all chips are shown in appendix A.3). This large size discrepancy, between the pore size and the micromodel thickness, means that the flow is more affected by the length-scale of the thickness of the microfluidic chip than by the size of the grains. Any difference in permeability between microfluidic chips is then explained by the varying tortuosity of the path the water must take around the grains. The small permeability of the composite large-small microfluidic chip compared to the others can be explained by the large differences in pore sizes, perhaps leading to flow disconnection. As the permeability is so similar for all microfluidic chips, it cannot be used for classification. Therefore, the pore size distribution is used to name the microfluidic chips, leading to the five different names used in this thesis, such as in Table 4-1.

Table 4-1 Results of the permeability test on chips used for salt dry-out experiments

Microfluidic chip	Permeability [milli darcy]
Small	588
Medium	545
Large	556
Large – Small	490
Medium– Small	526

4.2   Salt Dry-Out

In this chapter, the results of all experiments will be presented. As discussed in section 3.1.1, five different microfluidic chip designs were utilized for this experiment: three uniform microfluidic chips, a small, medium, and large pore size microfluidic chip, along with two dual pore size microfluidic chips—one with a large/small and the other with a middle/small pore size distribution (Figure 3-1 to Figure 3-5). Two experiments were conducted for each of the different microfluidic chip to verify the repeatability of the experiment.

Due to the difficulty in regulating the flow rate indicated by the mass flow controller, all flow rates were recalculated using the videos captured prior to the experiment in which the speed of the CO_2 front was measured. These range from 0.51 mm/s to 6.65 mm/s revealing a clear pattern: when the flow rate is higher, the initial water saturation level is lower.

The 10 conducted experiments have been visually observed and interpreted and the results are presented below (Figure 4-1 to Figure 4-34). For each of the uniform microfluidic chips, three graphs are presented: the first focuses on the overall microfluidic chip and the water-salt saturation over time, the second focuses solely on the water ratio within the microfluidic chip, distributed across the inlet, middle, and outlet, and the third focuses solely on the salt saturation within the microfluidic chip. For the two dual pore size microfluidic chips, the results are displayed in four graphs. There are two for water and two for salt saturation. For both saturations, the first graph illustrates the saturation per pore size. The other graph divides the microfluidic chip into thirds, representing the CO_2 inlet, middle, and outlet side of the chip. These regions are illustrated in Figure 3-13.

In all graphs, the plotted points represent the absolute data points, while the line displayed is a rolling average of the data. Due to fluctuations in light intensities per photo, differences may sometimes be observed between the points, but the rolling average line renders these differences nearly negligible. Additionally, water backflow is occasionally observed. This is evident when the blue water curve increases, often accompanied by a decrease in the amount of dried salt, as it is partly washed away or solubilized by the water. In almost all experiments, three stages can be observed: pre, during and post salt precipitation, characterized by changing slope on the salt and water saturation graphs.

4.2.1   Small pore size microfluidic chip

The difference between the two experiments conducted with the small pore size microfluidic chip is primarily in the flow rate at which the CO_2 enters the brine-saturated microfluidic chip. In the first experiment, the CO_2 displacement flowrate was higher at 4.38 mm/s compared to the second experiment, which had a flow rate of 0.78 mm/s. Considering the graphs of water and salt saturation, Figure 4-1 and Figure 4-2, it is noticeable in the first experiment water saturation decreases more rapidly, leading to faster salt formation. However, for the final result of salt dehydration, no significant difference can be observed; in both cases, the amount of salt is less than 10% (7% and 4% for the first and second experiment respectively) of the chip pore volume. However, especially in the second experiment, it is clear that as water evaporation intensifies and the saturation drops, the salt saturation increases. Regarding the difference in the location of water and salt within the chips (Figure 4-3 to Figure 4-6), no correlation can be observed because each individual experiment follows its own pattern.
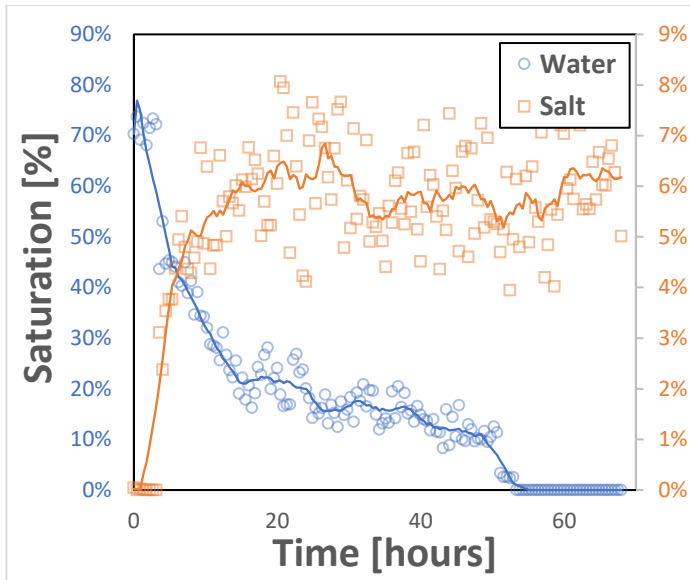
Figure 4-1 Water and salt saturation over time for the small pore microfluidic chip (q = 4.38 mm/s).
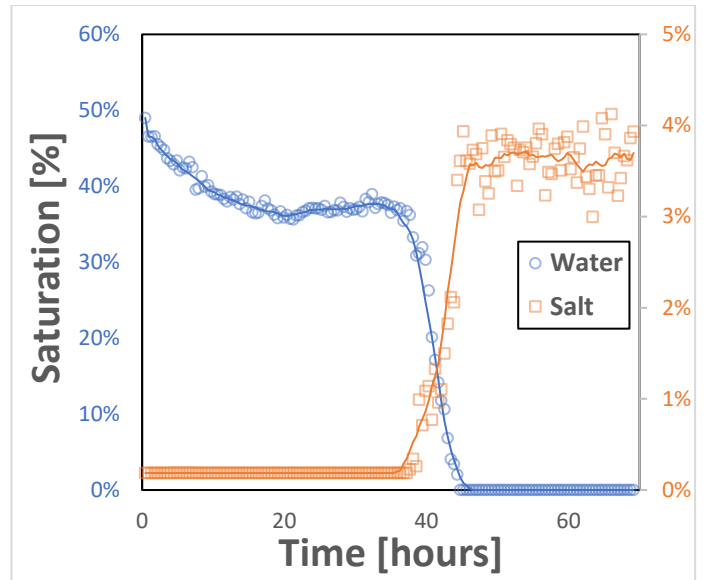
Figure 4-2 Water and salt saturation over time for the small pore microfluidic chip (q = 0.78 mm/s).
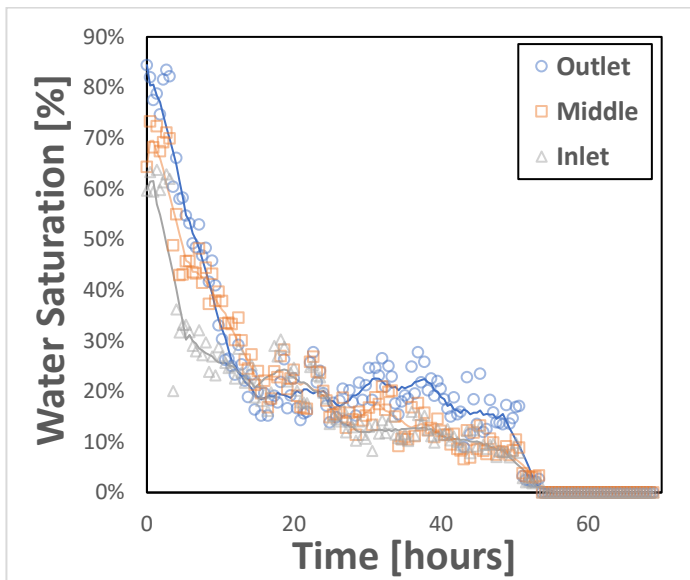
Figure 4-3 Water saturation over time for the small pore microfluidic chip in the inlet, middle and outlet sections (q = 4.38 mm/s).
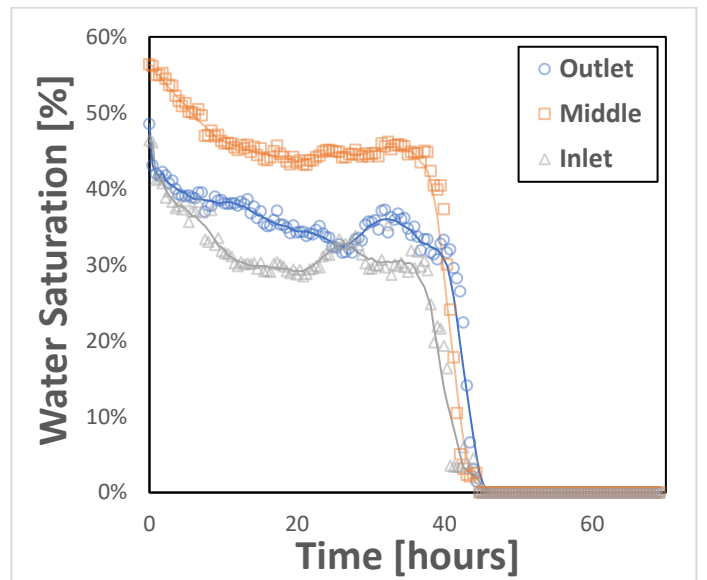
Figure 4-4 Water saturation over time for the small pore microfluidic chip in the inlet, middle and outlet sections (q = 0.78 mm/s).
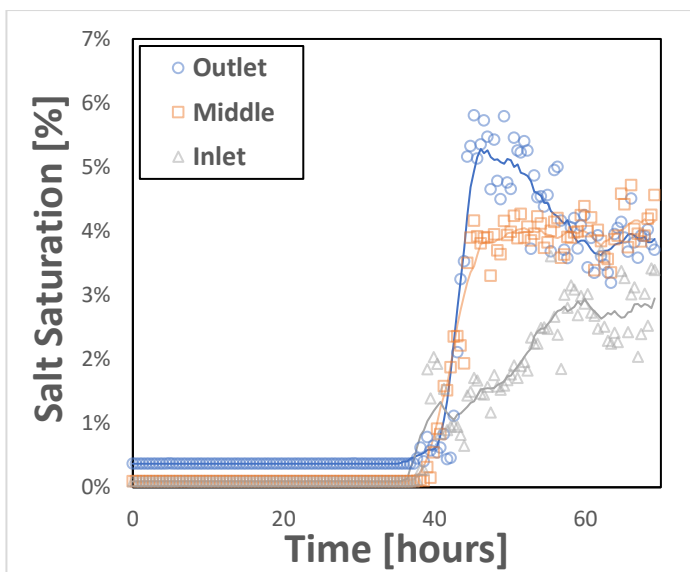
Figure 4-5 Salt saturation over time for the small pore microfluidic chip in the inlet, middle and outlet sections (q = 4.38 mm/s).
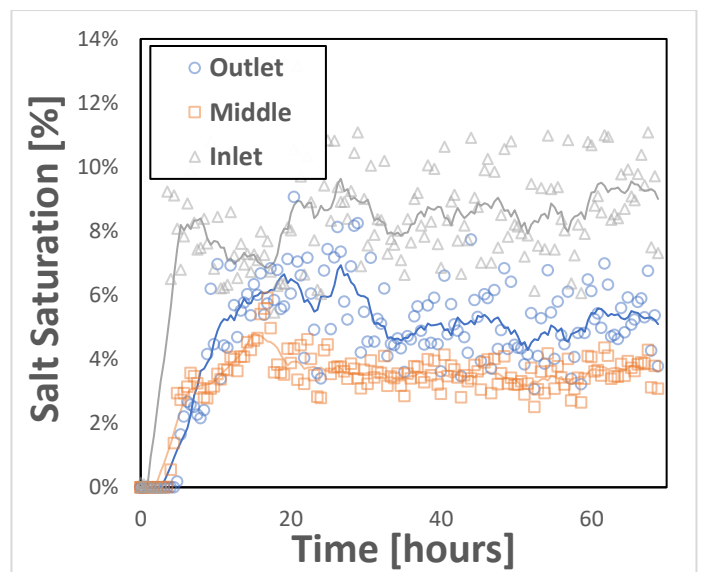
Figure 4-6 Salt saturation over time for the small pore microfluidic chip in the inlet, middle and outlet sections (q = 0.78 mm/s).

4.2.2 Medium pore size chip

For the medium pore size chip, the first experiment was conducted with a measured CO_2 flow rate of 6.65 mm/s, and the second experiment with a measured flow rate of 2.05 mm/s. In Figure 4-7, it can be observed that there was a water backflow after approximately 24 hours causing a delay in salt precipitation. However, this occurred before the salt had started to dehydrate, thus it had no further effect on the results. The second experiment (Figure 4-8) with the lower starting flow rate exhibits a more gradual curve, neatly illustrating that as the water evaporates, the salt begins to grow. For the graphs showing a distribution over inlet, middle, and outlet, (Figure 4-9 to Figure 4-12) a pattern is visible in this case. Looking at the water saturation for both experiments, it is highest at the outlet, followed by the middle, and lowest at the inlet. Regarding salt saturation, in both cases, it is highest at the inlet side. This is surprising, as one would expect the highest salt saturation where the brine saturation is also highest. To explain this phenomenon, more research is needed.
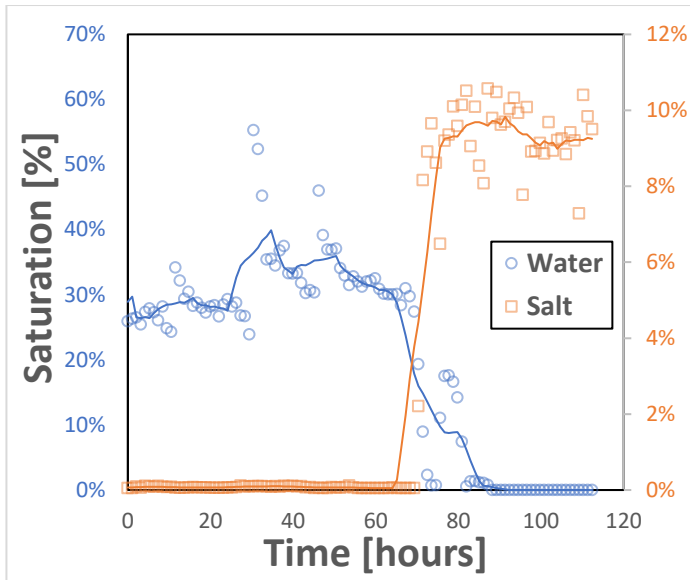
Figure 4-7 Water and Salt saturation over time for the medium pore microfluidic chip (q = 6.65 mm/s).
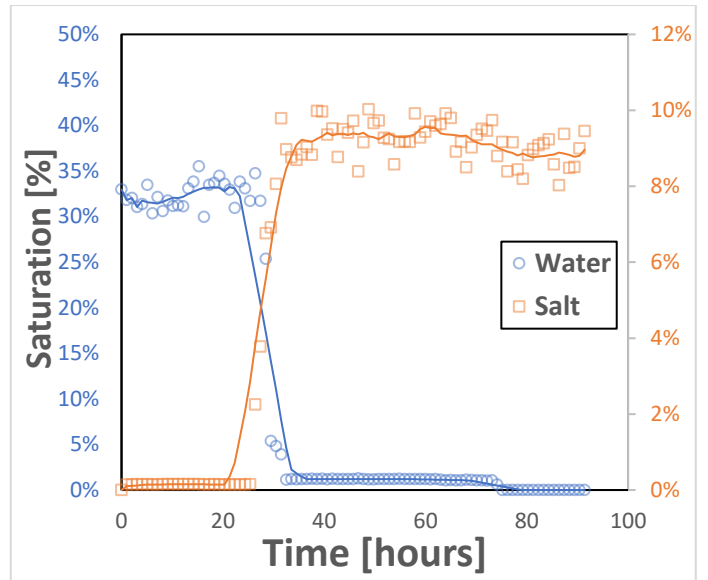
Figure 4-8 Water and Salt saturation over time for the medium pore microfluidic chip (q = 2.05 mm/s).
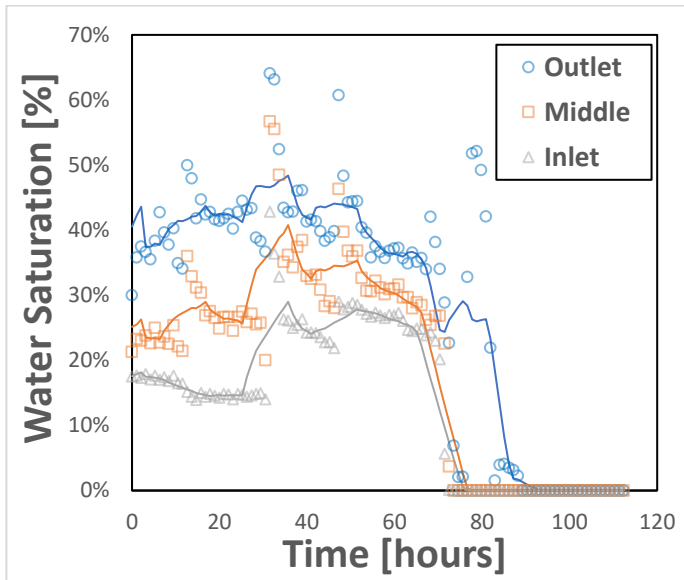
Figure 4-9 Water saturation over time for the medium pore microfluidic chip in the inlet, middle and outlet (q = 6.65 mm/s).
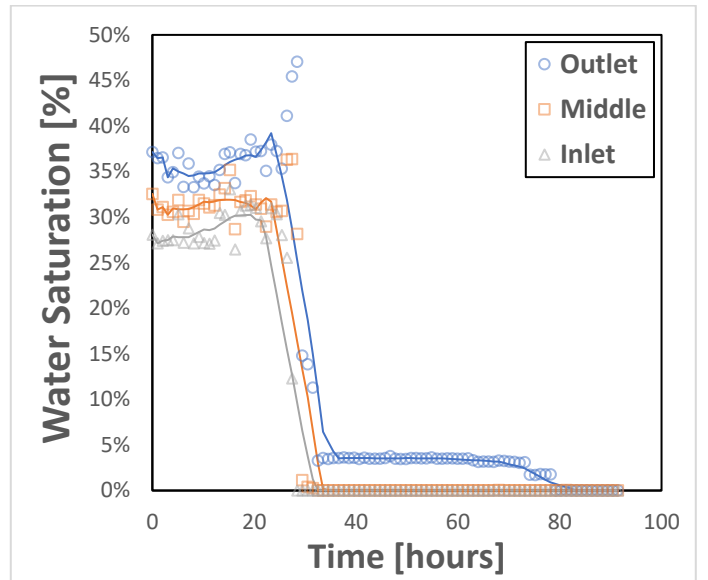
Figure 4-10 Water saturation over time for the medium pore microfluidic chip in the inlet, middle and outlet (q = 2.05 mm/s).
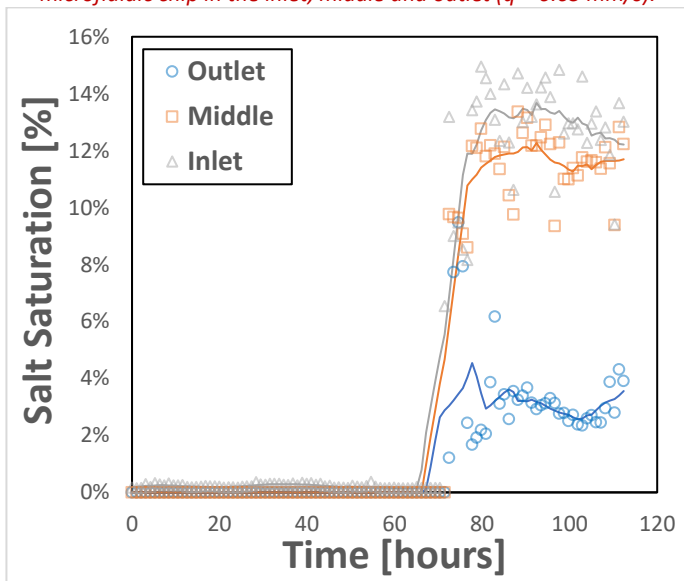
Figure 4-11 Salt saturation over time for the medium pore microfluidic chip in the outlet, middle and inlet sections (q = 6.65 mm/s).
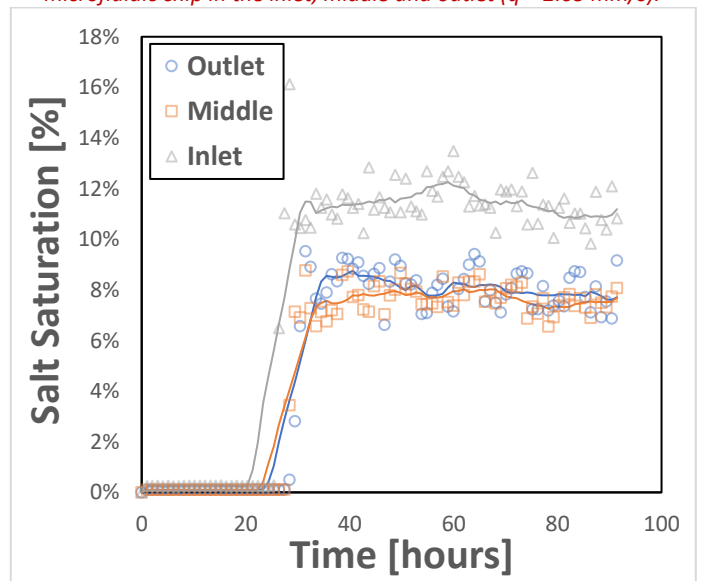
Figure 4-12 Salt saturation over time for the medium pore microfluidic chip in the outlet, middle and inlet sections (q = 2.05 mm/s).

4.2.3 Large pore size microfluidic chip

For the experiments with the large pore size microfluidic chip, the first experiment had a CO_2 flow rate value of 1.64 mm/s, and the second experiment had a value of 0.51 mm/s. These values are relatively close to each other, when compared to the previous two tests.

In both experiments, there was a moment of water backflow. In the first experiment (Figure 4-13), this occurred only once, during the evaporation of water and the precipitation of salt. Due to the water backflow, some of the salt was re-dissolved and the saturation levels were reduced, but after the backflow had evaporated, the amount of salt that had formed was around 10%. The situation was slightly different for the second experiment (Figure 4-14). Here, the water backflow had already occurred once before the salt precipitation began. After about 13 hours, the first salt dry-out session was essentially complete, but it continued to run to observe the long-term effects. At around 25 hours another water backflow occurred, shown by a sudden increase in water, which reduced the amount of salt. Ultimately, the salt saturation never exceeded around 10%.

Regarding the distribution of water within the microfluidic chip, a pattern can be observed in both experiments (Figure 4-15 to Figure 4-18) where it is highest at the outlet, followed by the middle, and least at the inlet side of the microfluidic chip. In both cases the water backflow occurred, causing most of the salt disappeared at that time. There is no discernible pattern in the final salt distribution of both experiments.
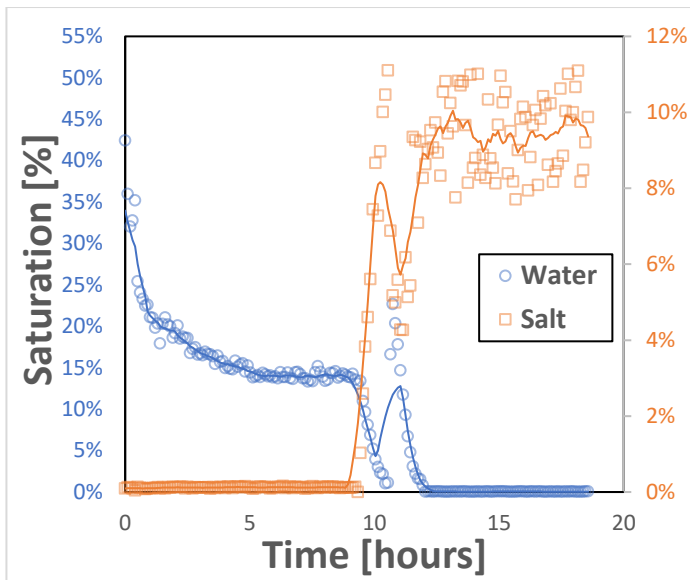
Figure 4-13 Water and salt saturation over time for the large pore microfluidic chip (q = 1.64 mm/s).
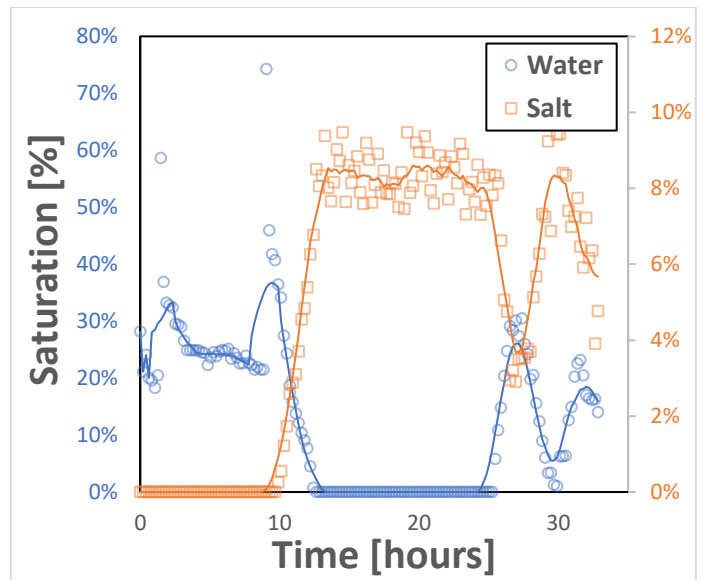
Figure 4-14 Water and salt saturation over time for the large pore microfluidic chip (q = 0.51 mm/s).
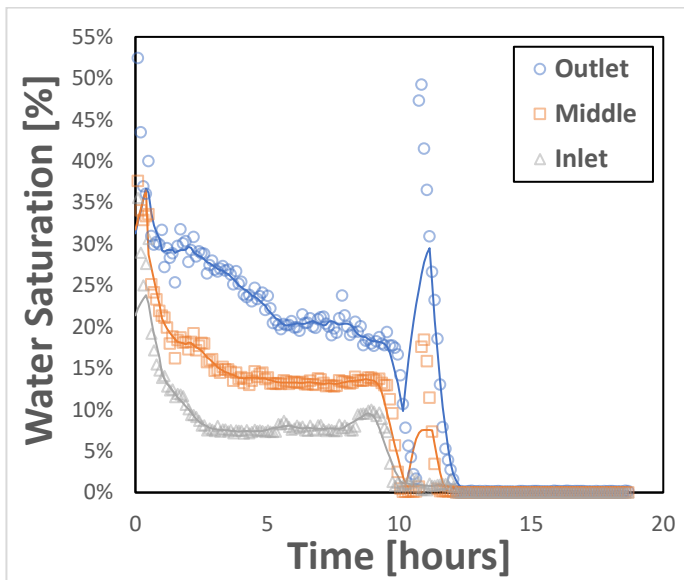
Figure 4-15 Water saturation over time for the large pore microfluidic chip in the inlet, middle and outlet sections (q = 1.64 mm/s).
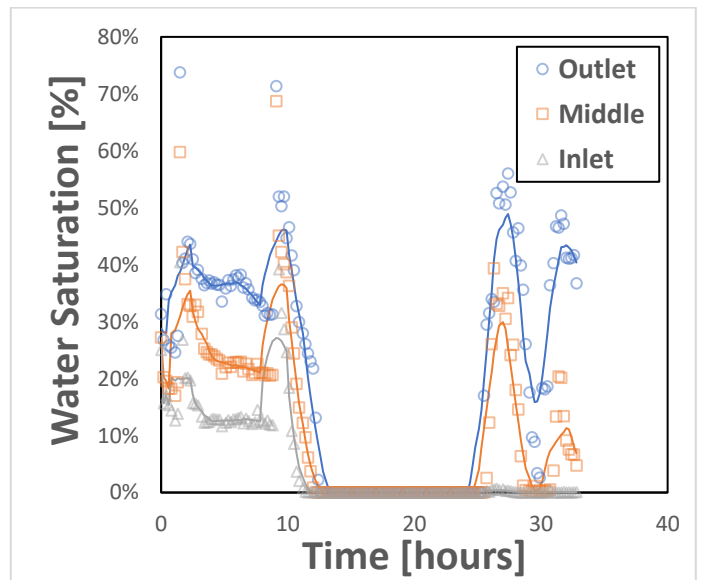
Figure 4-16 Water saturation over time for the large pore microfluidic chip in the inlet, middle and outlet sections (q = 0.51 mm/s).
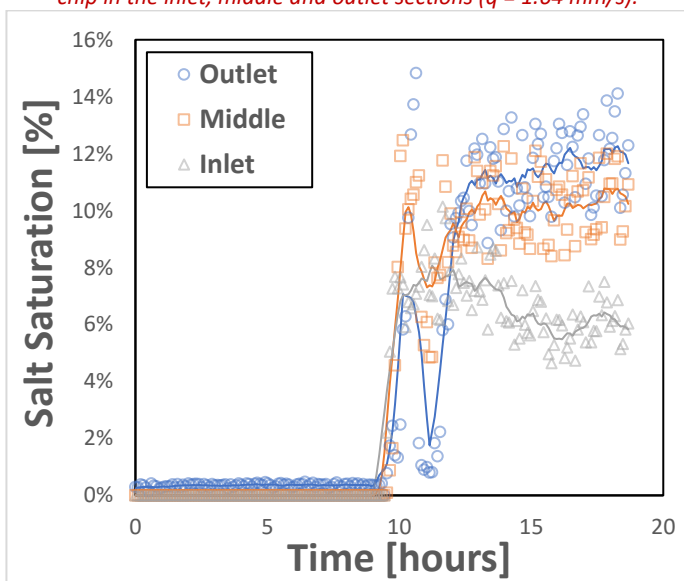
Figure 4-17 Salt saturation over time for the large pore microfluidic chip in the inlet, middle and outlet sections (q = 1.64 mm/s).
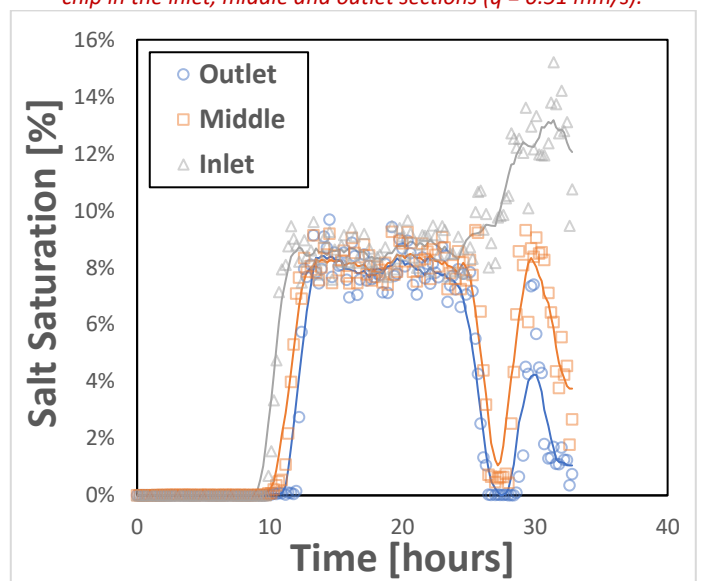
Figure 4-18 Salt saturation over time for the large pore microfluidic chip in the inlet, middle and outlet sections (q = 0.51 mm/s).

4.2.4   Large-small pore size microfluidic chip

For the two experiments with the large-small pore size microfluidic chip, the first had a CO_2 flow rate measured at 1.93 mm/s, and the second experiment had one at 1.03 mm/s. In both experiments, it can be observed in Figure 4-20 and Figure 4-21 that in the small pore size section, water saturation starts higher and remains higher than the water saturation in the large pore size section. In the first experiment, a significant water backflow is observed starting after approximately 15 hours, however, this occurred before salt dehydration took place, thus not showing any notable events in the salt saturation curve. In this first experiment, water backflow also occurred during salt dehydration, after approximately 30 hours, albeit of much lesser magnitude but still during dehydration, causing a reduction in the salt curve around this time. After this, it started dehydrating again, but the salt never reached the value of 10% for the backflow; it reached a final value of 7% in the total microfluidic chip. In the second experiment, small water backflows can be observed but are not particularly noteworthy. The salt shows a steady growing curve (Figure 4-24 and Figure 4-25) until the water is completely dried out. This experiment lasted longer because a sort of water reservoir, visible in Figure 4-19 in the Small-Outlet corner, had formed in the middle of the microfluidic chip, which slowly dries out. In both experiments, the salt was distributed quite evenly over the chip(see Figure 4-26 and Figure 4-27). Interestingly, the water distribution (Figure 4-22 and Figure 4-23) show a different distribution, with most water present at the outlet side for most of the experiment.
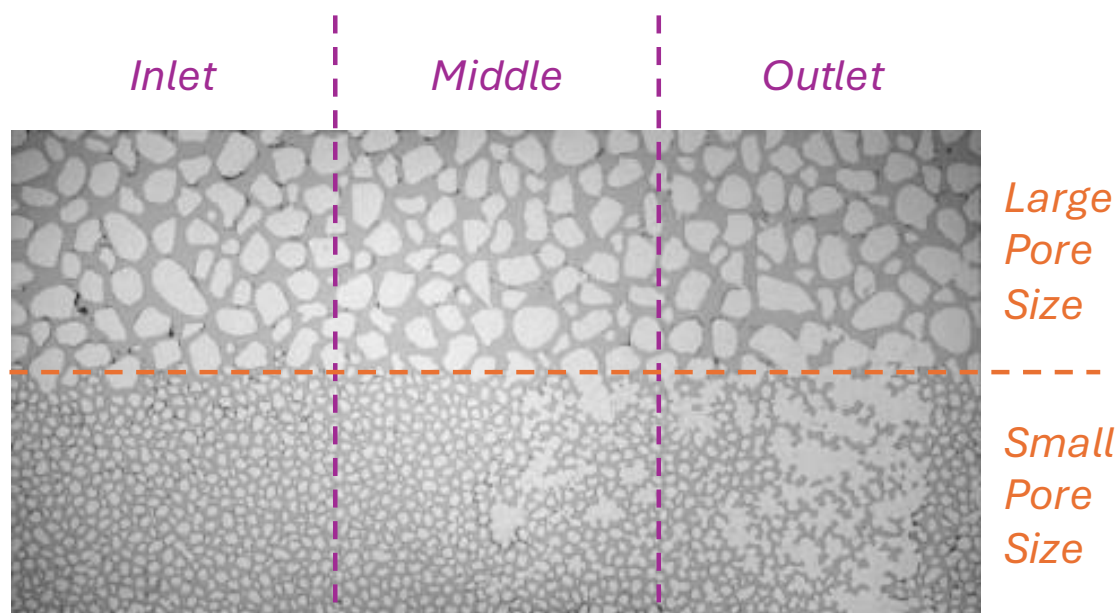
Figure 4-19 Picture of the chip, with the water 'reservoir' shown in the bottom right corner
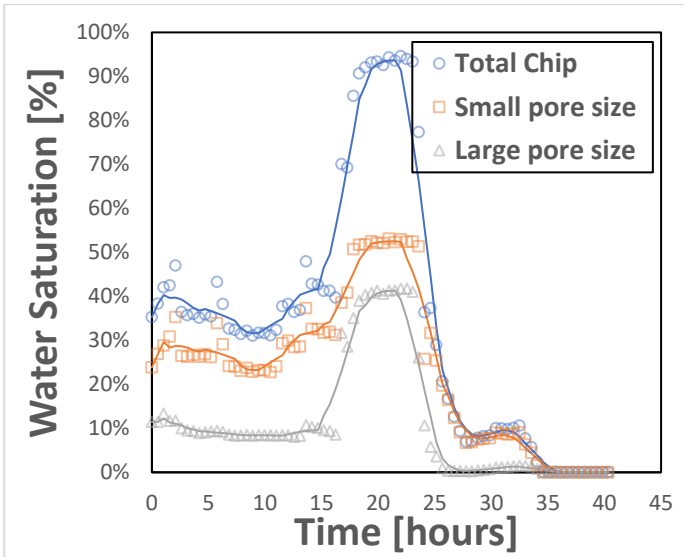
Figure 4-20 Water saturation for the large-small pore chip in the entire chip, the small pores and large pores sections (q = 1.93 mm/s)
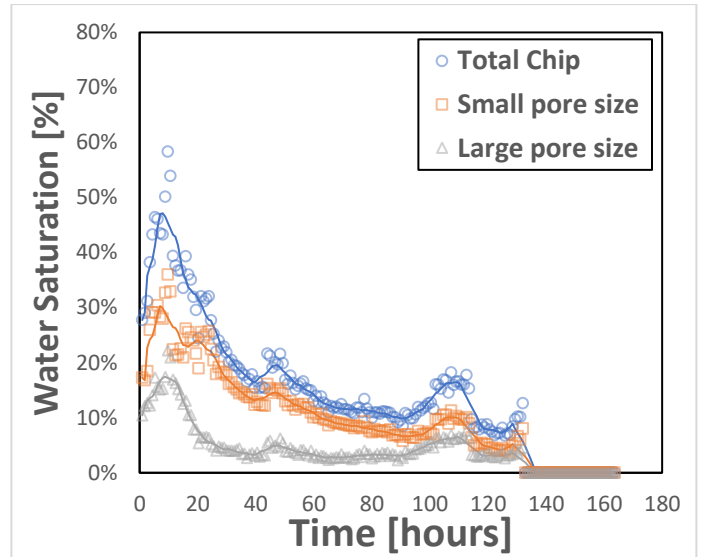
Figure 4-21 Water saturation for the large-small pore chip in the entire chip, the small pores and large pores sections (q = 1.03 mm/s)

45
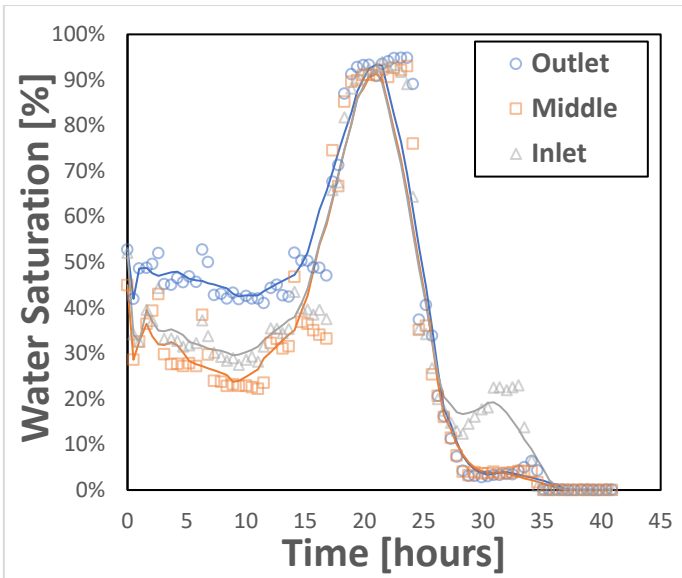
Figure 4-22 Water saturation over time for the large-small pore chip in the inlet, middle and outlet sections (q = 1.93 mm/s).
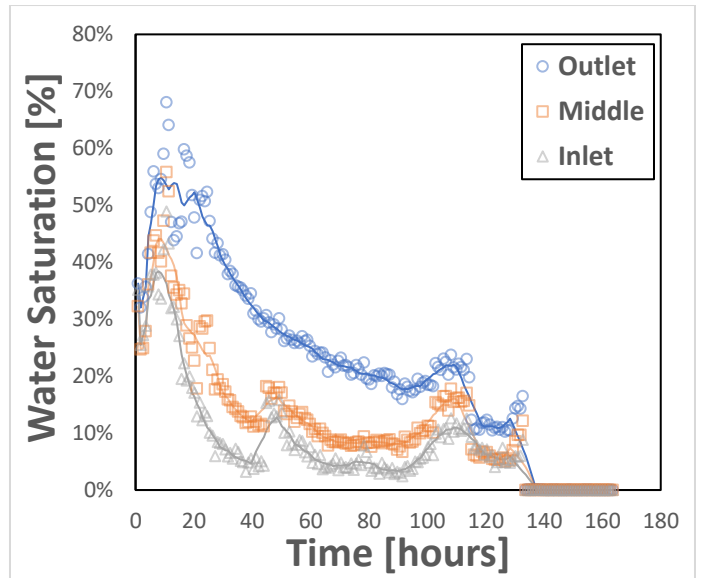
Figure 4-23 Water saturation over time for the large-small pore chip in the inlet, middle and outlet sections (q = 1.03 mm/s).
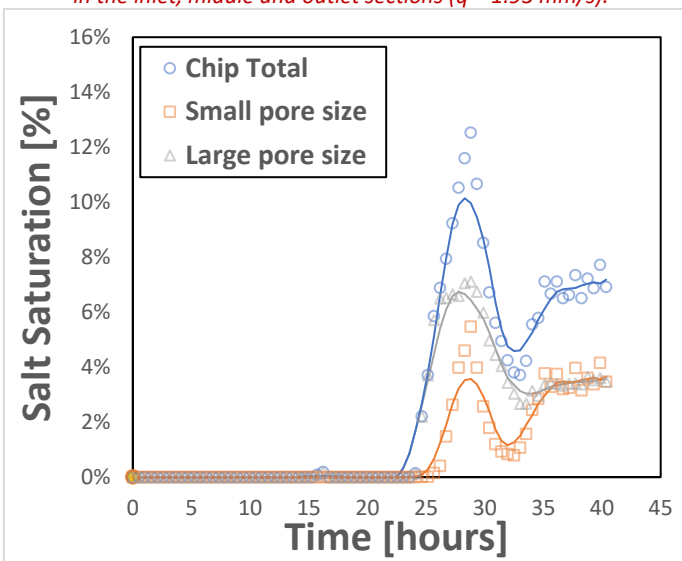
Figure 4-24 Salt saturation for the large-small pore chip in the entire chip, the small pores and large pores sections (q = 1.93 mm/s)
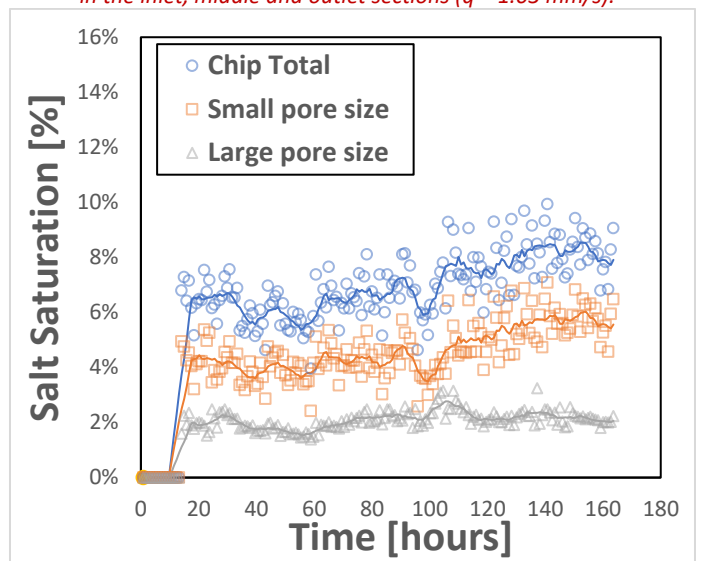
Figure 4-25 Salt saturation for the large-small pore chip in the entire chip, the small pores and large pores sections (q = 1.03 mm/s)
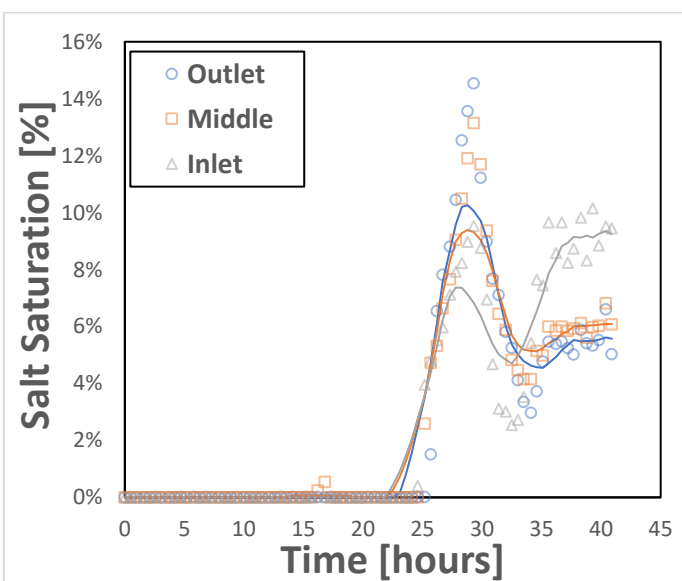
Figure 4-26 Salt saturation over time for the large-small pore chip in the inlet, middle and outlet sections (q = 1.93 mm/s).
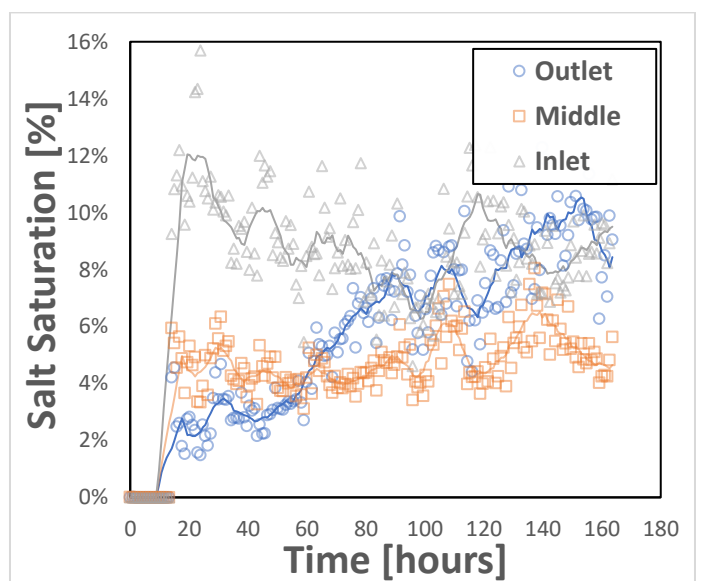
Figure 4-27 Salt saturation over time for the large-small pore chip in the inlet, middle and outlet sections (q = 1.03 mm/s).

4.2.5   Medium-small pore size microfluidic chip

For the medium-small pore size microfluidic chips, the first experiment had a measured flow rate of 2.79 mm/s, while the second experiment had a flow rate of 0.86 mm/s. In both experiments with these microfluidic chips, the majority of salt was measured in the small pore size side (Figure 4-32 and Figure 4-33). The water flow followed a similar pattern in both experiments, starting around 30% and gradually decreasing until salt precipitation occurred (Figure 4-28 and Figure 4-29). There was no occurrence of water backflow in either experiment. Moreover, there was no significant difference observed in the water saturation between the small and medium sections in both situations; it remained around the same value. Similarly, the distribution of salt between the small and medium sections was consistent. However, regarding the distribution between outlet, middle, and inlet, a difference can be noted (Figure 4-34 and Figure 4-35). In the first experiment, the most salt was formed in the middle, followed by the inlet, and the least in the outlet. Conversely, in the second experiment, the most salt was precipitated in the outlet. This is also corroborated by the water distribution in Figure 4-31.
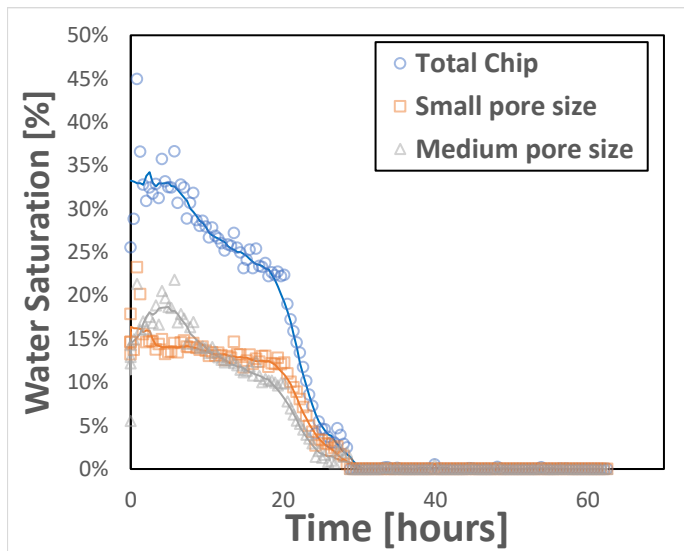
Figure 4-28 Water saturation for the medium-small pore chip in the entire chip, the small pores and large pores section (q = 2.79 mm/s)
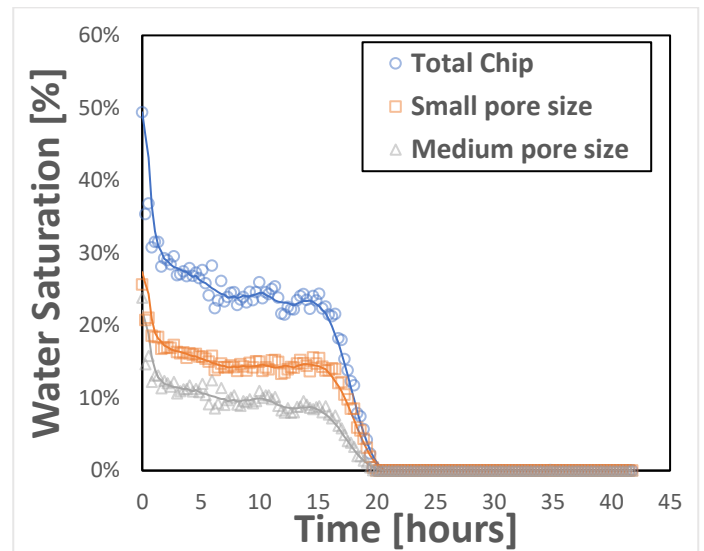
Figure 4-29 Water saturation for the medium-small pore chip in the entire chip, the small pores and large pores section (q = 0.86 mm/s)
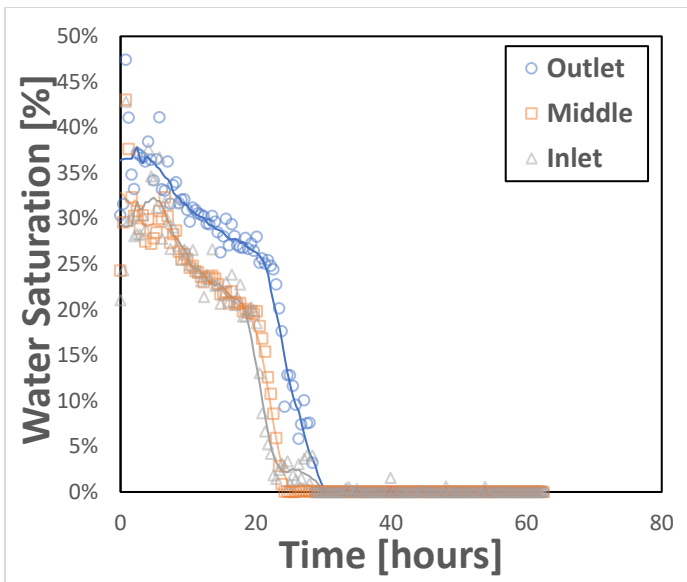
Figure 4-30 Water saturation over time for the medium-small pore chip in the inlet, middle and outlet sections (q = 2.79 mm/s).
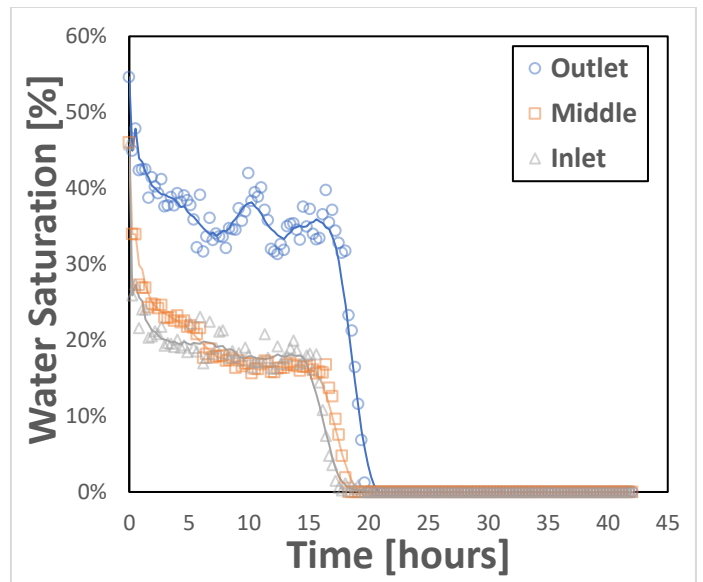
Figure 4-31 Water saturation over time for the medium-small pore chip in the inlet, middle and outlet sections (q = 0.86 mm/s).
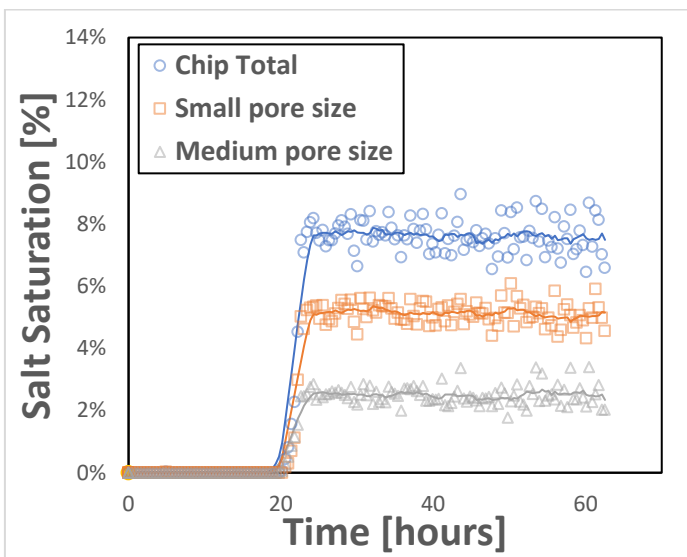
Figure 4-32 Salt saturation for the medium-small pore chip in the entire chip, the small pores and large pores sections (q = 2.79 mm/s)
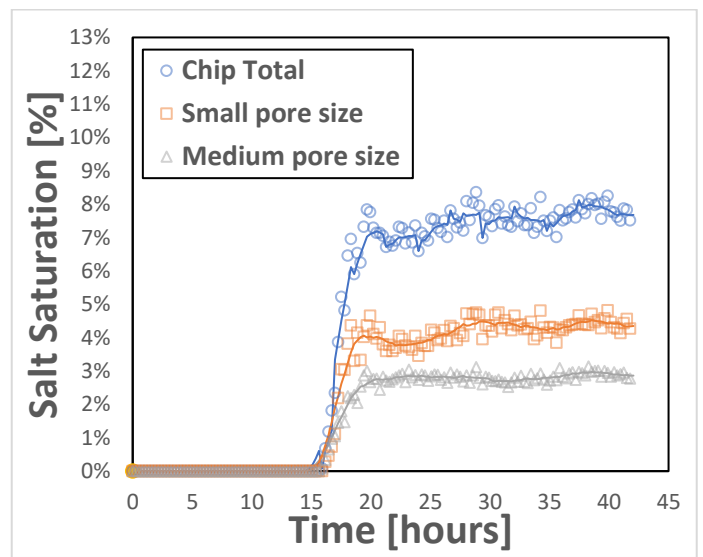
Figure 4-33 Salt saturation for the medium-small pore chip in the entire chip, the small pores and large pores sections (q = 0.86 mm/s)
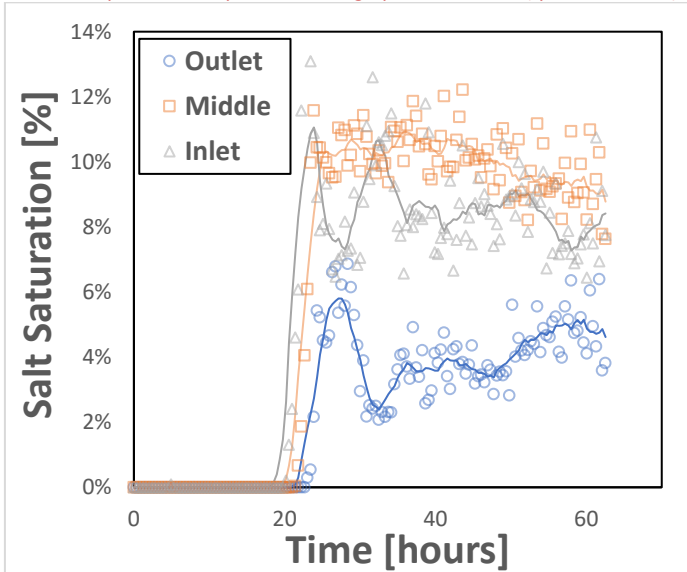
Figure 4-34 Salt saturation over time for the medium-small pore chip in the inlet, middle and outlet sections (q = 2.79 mm/s).
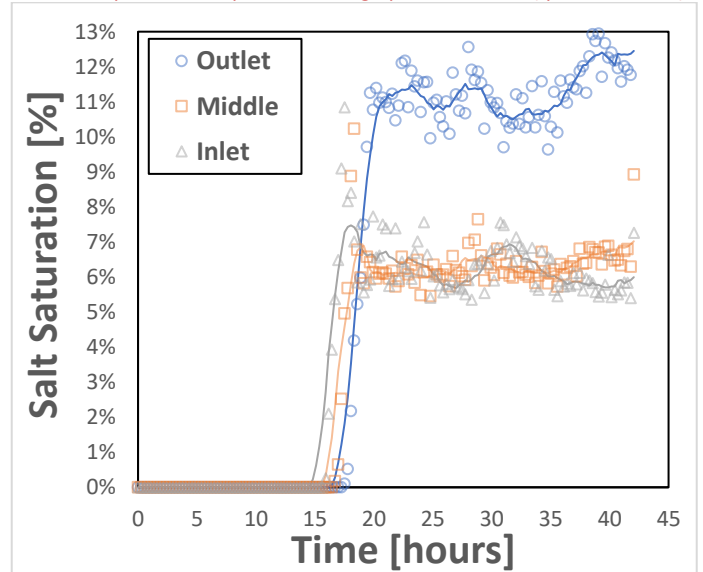
Figure 4-35 Salt saturation over time for the medium-small pore chip in the inlet, middle and outlet sections (q = 0.86 mm/s).

48

4.3 Effect of heterogeneity

The results of the homogeneous microfluidic chip show that for a given water saturation, a larger pore size will result in a higher salt saturation. Yet the inverse seems to hold true for the heterogenous microfluidic chips. For both the large-small as the medium-small microfluidic chip, the salt saturation in the small part of the microfluidic chip (7 and 5%) exceeds the salt saturation in the large or medium pore size part (5 and 3%). Again, the salt saturation is higher in the large pore size part than in the medium pore size part.

This phenomenon can be explained by the capillary number and capillary suction, as a thin tube absorbs liquid very quickly. The small pores are more dominated by capillary action, and therefore might attract more brine.

Additionally, the presence of multiple pore size might have an influence of the path of CO_2 flow. The CO_2 undergoes less resistance when navigating through the larger pore sizes, resulting in more brine being flushed out and consequently less salt precipitation in the larger pore size areas, while more salt is precipitated in the smaller pore size areas. This can be observed in Figure 4-36, which is the first image of a medium-small pore size microfluidic chip after CO_2 injection. In this image, it is evident how the CO_2 flow enters and causes more brine to be flushed out in the larger pore sizes. Figure 4-37 shows the situation 7 minutes later, where it is apparent that only after several minutes of flow does the brine distribution become more even across the two different pore size areas.
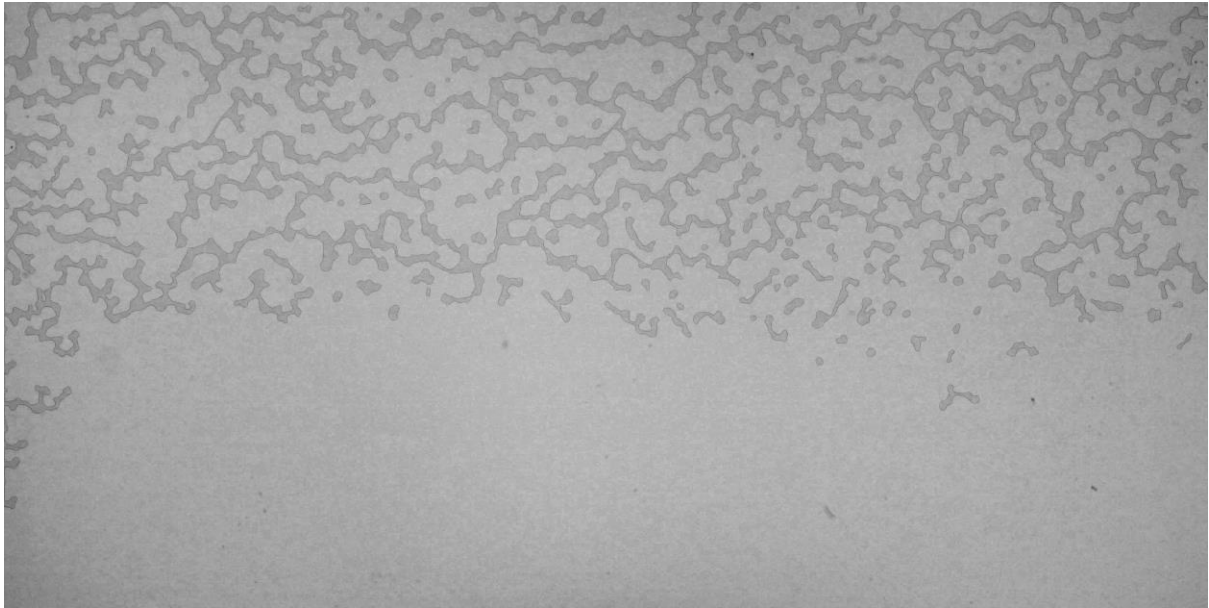
Figure 4-36 First image after beginning the CO$_2$ injection in the heterogenous medium-small pore size microfluidic chip
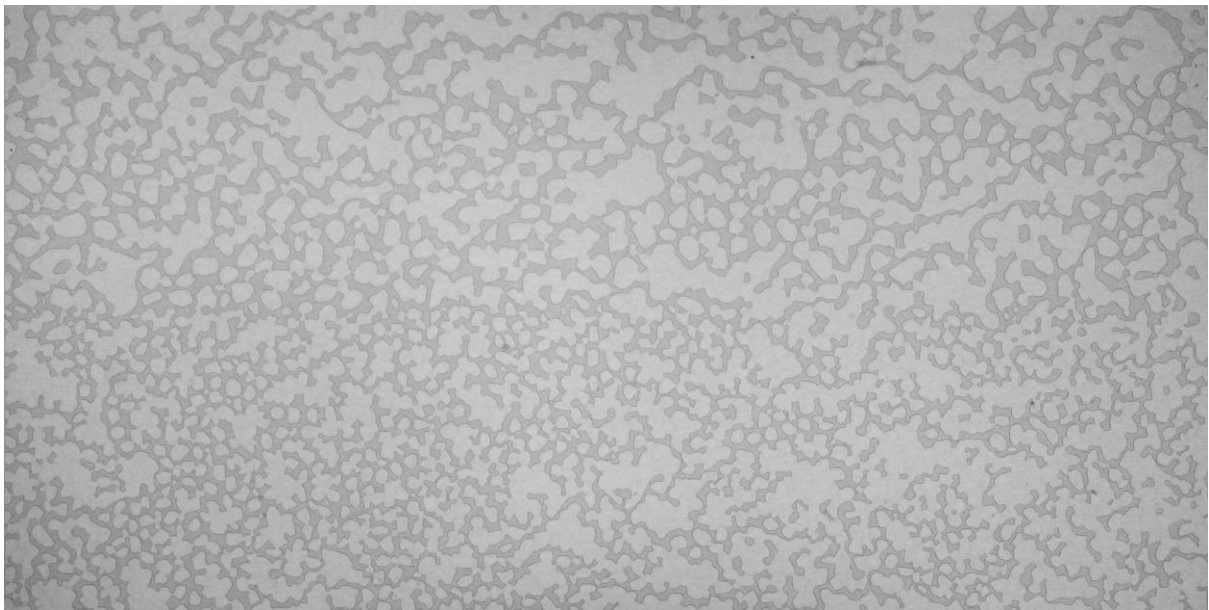
Figure 4-37 Image after 7 minutes the CO$_2$ injection in the heterogenous medium-small pore size microfluidic chip

4.4   Summary of Salt Dry-Out Results

In Table 4-1 an overview of all the experiments and their results is provided. This table can also be found in appendix D.

Table 4-2 Overview of all salt dry-out experiments and obtained results

Experiment	Flowrate mm/s	Hours till dry-out	Longest lasting water location	Highest salt concentration location	Max. water	Max. salt	Max. water large/ medium	Max. salt large/ medium	Max. water small	Max. salt small	Water backflow	Bigger than initial value	Initial max. water value
Small 1	4.38	54	outlet	inlet	74%	7%					no		
Small 2	0.78	45	middle	outlet	49%	4%					no		
Medium 1	6.65	89	outlet	inlet	40%	10%					yes	yes	29%
Medium 2	2.05	76	outlet	inlet	36%	10%					no		
Large 1	1.64	12	outlet	outlet	42%	11%					yes	no	
Large 2	0.51	13	outlet	inlet	38%	9%					yes	yes	32%
Large-Small 1	1.93	35	outlet	Inlet	94%	12%	42%	5%	53%	7%	yes	yes	40%
Large-Small 2	1.03	133	outlet	Inlet	53%	9%	22%	3%	33%	6%	yes	no	
Medium-Small 1	2.79	29	outlet	middle	37%	8%	21%	3%	16%	5%	no		
Medium-Small 2	0.86	20	outlet	outlet	31%	8%	19%	3%	13%	5%	no		

5   Experimental Results: Hydrates

As mentioned earlier, all hydrate experiments in this thesis were conducted using the physical rock network microfluidic chip. This thesis encompasses three experiments, each performed using different pressure pulse triggers. In the first experiment, the pressure-pulse was controlled manually. In the second experiment, we utilized an electronic trigger, which gave a pressure-pulse of 0.5 seconds duration. As detailed in section 5.2.2, this did not yield significant hydrate formation. Based on these findings, we conducted the final experiment again using the trigger mode, but with a reduced duration of 0.2 seconds for the pressure pulse. Each experiment was conducted a second time in the same manner as the first: this is referred to as the second cycle. These second cycle experiments will also be described in detail.

The moments of triggering a pressure pulse are discernible on the absolute pressure curve, marked by spikes in the graphs, as depicted in Appendix Figure B-3, Appendix Figure B-4 and Appendix Figure B-5 in appendix B.3.

In some situations, it was observed that hydrates formed and quickly dissipated or shifted slightly in position. This phenomenon can be attributed to their proximity to, or even location on, the phase boundary. Thus, tiny variations in temperature and pressure can cause them to oscillate back and forth between different sides of the phase boundary. When hydrates form, they release heat, and even the slightest fractional change in temperature can lead to crossing the boundary. Consequently, a weak hydrate is likely to reside close to the phase boundary, making it susceptible to minor fluctuations and movement.

5.1 Hydrate morphologies in micromodel

In Appendix B.2, Appendix Figure B-2, an image is shown that depicts how the hydrates form in the micromodel. Notably, unlike the drying experiments where all formed salt crystals appeared as a kind of an amorphous interface, the hydrates manifest in various structures within the micromodel.

When zooming in on Appendix Figure B-2, these described hydrate structures from the literature, as described in section Hydrate morphology 2.2.6 and shown in Figure 2-8, can indeed be identified. However, the image results also show a remarkable occurrence of a 'sheet-like' hydrate structure that is not present in hydrate descriptions found in literature. However, a similar structure to this is known to occur in ice formation. This form is categorized under the 'column' type of snow crystals, which is further subdivided into various types in snow crystal morphology: needles, hollow columns, and solid prisms. These column structures form at a temperature of approximately -5°C. The different types of ice crystals are shown in Figure 5-1 (Libbrecht, 2005). However, because our result shows only one form in this structure, and it does not exactly match the detailed ice structures in shape or appearance characteristics, we refer to it in our context as the 'sheet-like' hydrate. When zoomed in on the photo from the attachment, these differences are clearly illustrated, as seen in the Figure 5-2 below.
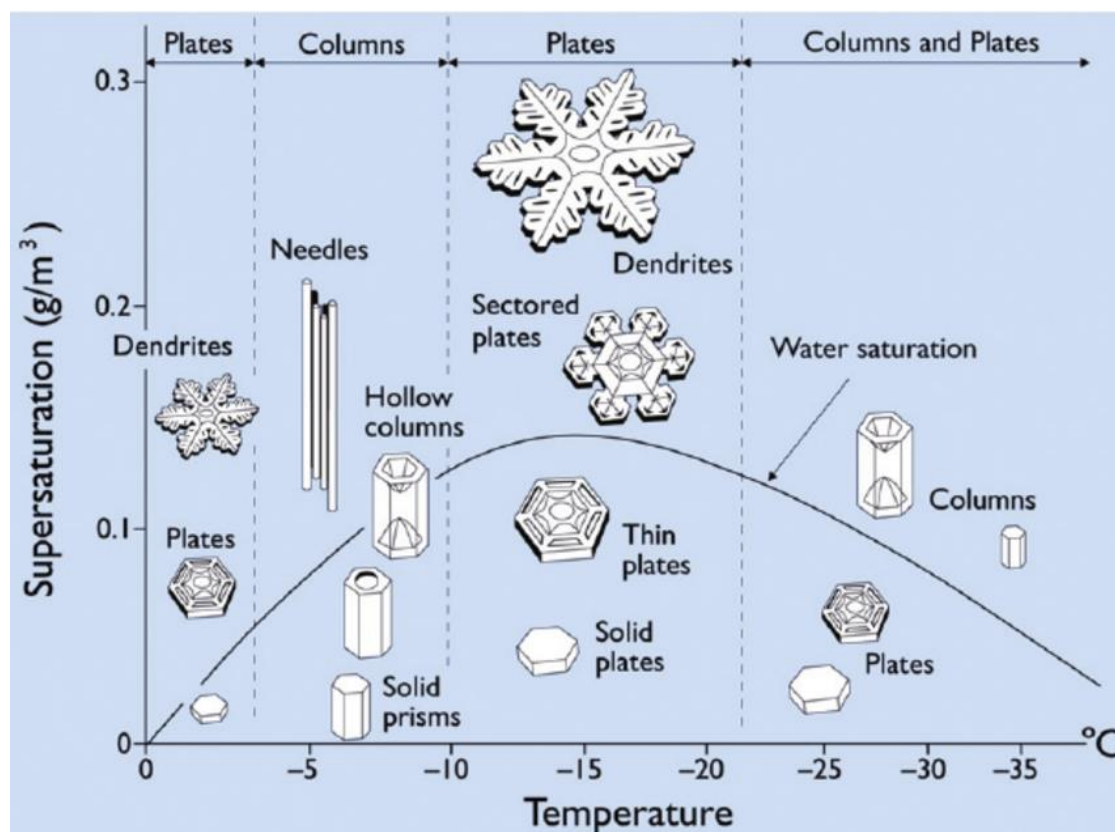
Figure 5-1 The snow crystal morphology diagram, showing different types of snow crystals that grow in air at atmospheric pressure, as a function of temperature and water supersaturation relative to ice (Libbrecht, 2005).

'Load-bearing'   'Pore-filling'   'Sheet'

'Patchy'   'Grain-coating'   'Grain-cementing'
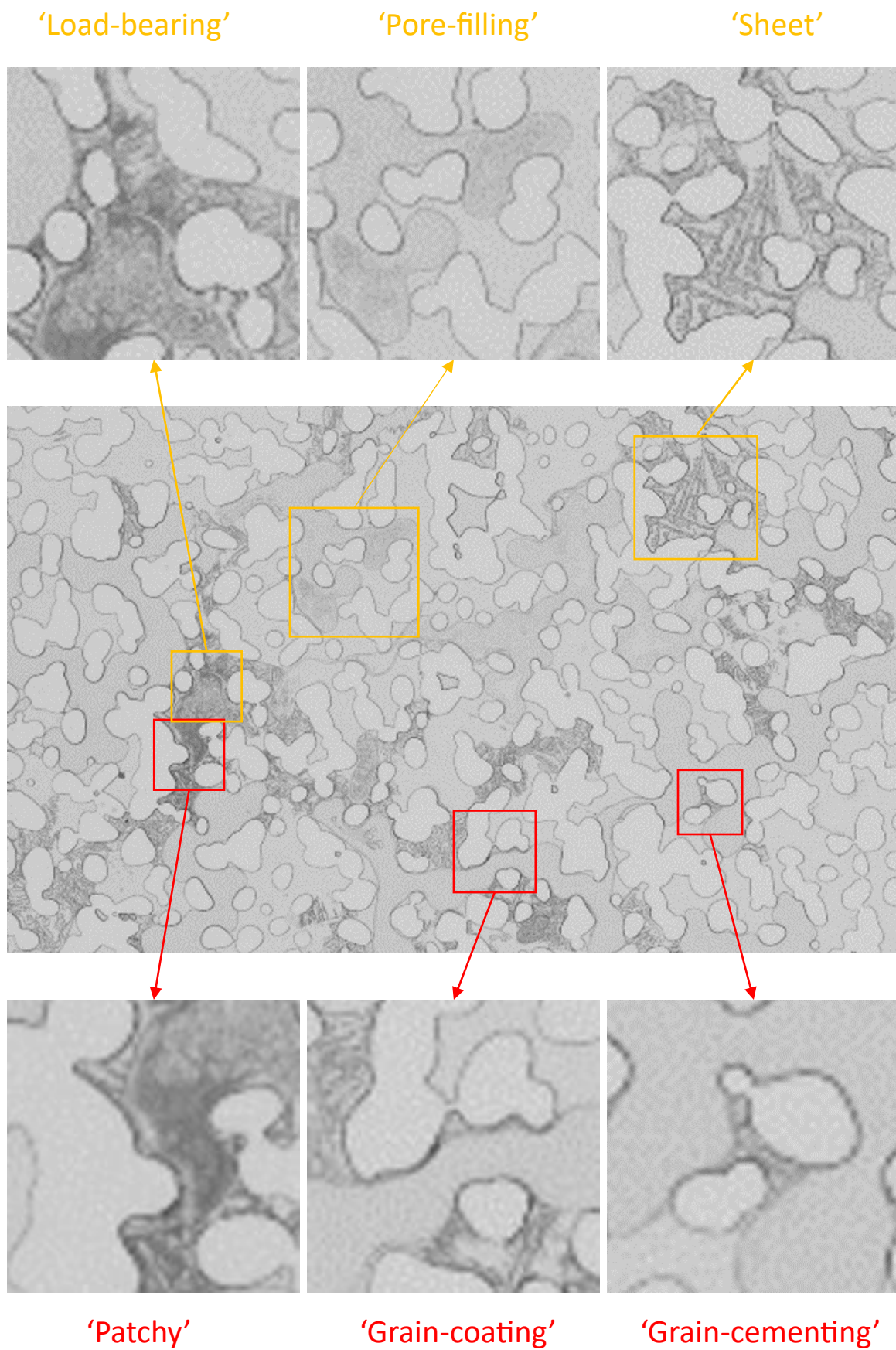
Figure 5-2 Hydrates morphologies in micromodel physical rock network EOR microfluidic chip

5.2 Physical rock network EOR microfluidic chip

In this section, the three experiments and their results will be discussed in three subsections. Each of these subsections presents six graphs that are explained in detail. The first three graphs per experiment are from the first cycle of hydrate formation, and the second three graphs are from the second cycle of hydrate formation. The first graph in each case focusses on the initial part of the experiment, clearly illustrating the hydrate saturation starting from time zero. The second graph provides an overview of the hydrate saturation over the whole period of the experiment. The third graph shows the hydrate saturation during dissociation, and this graph depicts the behavior of the hydrates when the temperature is increased. The temperature was raised in steps, and this is indicated on the graphs with a vertical line to indicate the time for each step.

5.2.1 First experiment with manually controlled pressure

As mentioned earlier, the first experiment was conducted with manual control of the pressure pulse used to trigger the hydrate formation. The initial water content during the first cycle of hydrate formation was around 90%. Within the first minute of CO_2 flow the water content decreased to about 70% and then gradually towards 60%, the hydrates immediately formed, filling around 15% of the microfluidic chip's pore area. This behavior occurred in the first 8 minutes of the experiment, as shown in Figure 5-3.

In Figure 5-4, the subsequent progression of the hydrate formation during the first cycle is illustrated. The trend appears to be fairly consistent. The water content shows a slight upward trend from around 55% to 60%, while the hydrates exhibit a downward trend from 15% to approximately 5%. In total, the first cycle achieved a conversion factor of 9.4%. The rest of the water was displaced from the chip.

Figure 5-5 shows the dissociation process. For this, the temperature was increased in two steps. First, the circulating bath temperature was raised to 5°C. However, no significant change was observed. Subsequently, the temperature was increased to 10°C, where the hydrates started dissolving after reaching at 8.7°C, completely disappearing at 8.8°C, causing an increase in water content. To determine the exact temperature at which the hydrates started to dissociate during this temperature increase, the temperature graph was examined, see Figure 5-9.
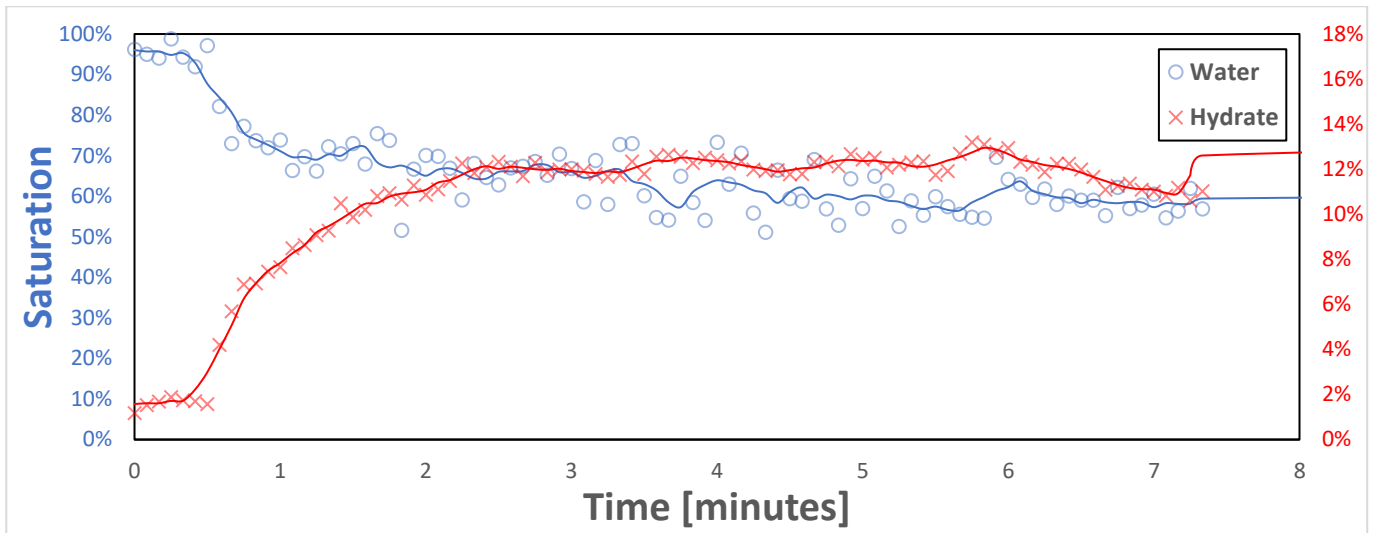
Figure 5-3 First experiment, first cycle, focused on the initial minutes of hydrate formation with the water saturation plotted on the left y-axis in blue and the hydrate saturation plotted in the right y-axis in red.
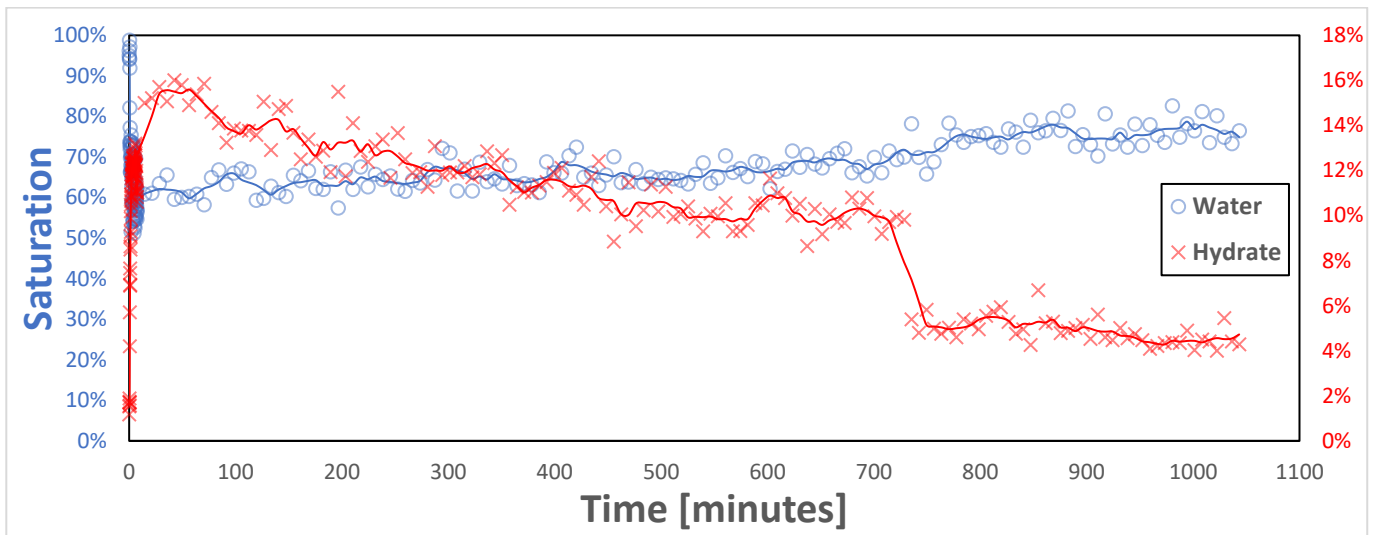
Figure 5-4 First experiment, first cycle, behavior over the complete cycle with the water saturation plotted on the left y-axis in blue and the hydrate saturation plotted in the right y-axis in red.
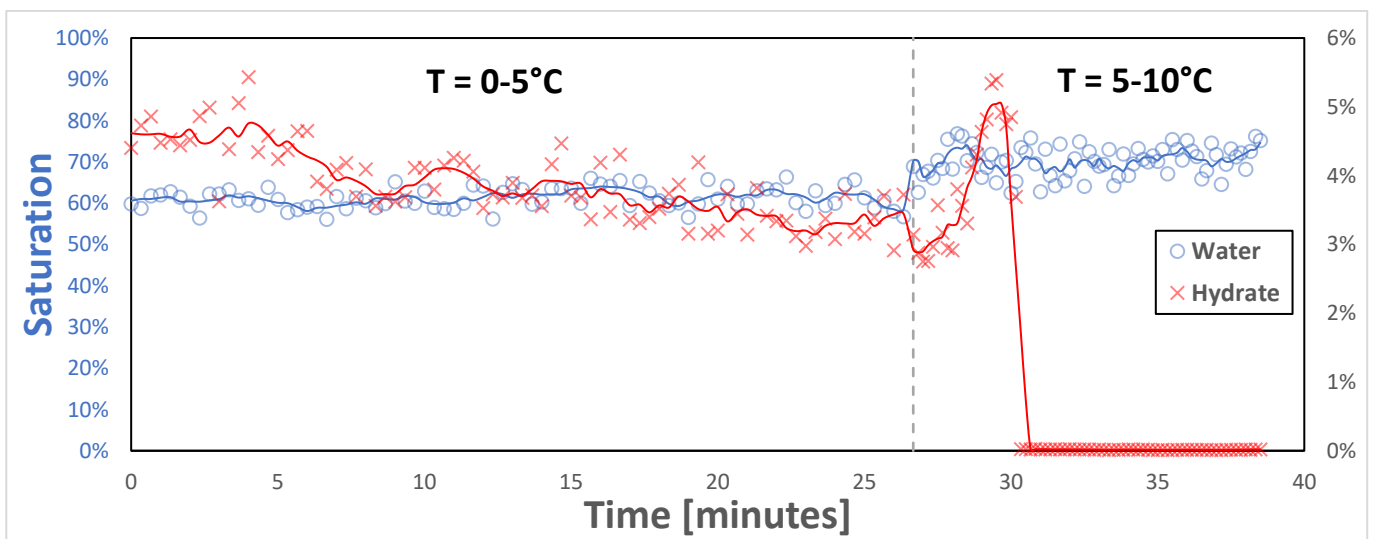
Figure 5-5 First experiment, first cycle, dissociation phase with the water saturation plotted on the left y-axis in blue and the hydrate saturation plotted in the right y-axis in red.

The second cycle differed from the first, as the initial water saturation was lower, which is logical for a subsequent cycle. As shown in Figure 5-6, it began with a water saturation slightly over 60%. Hydrates formed rapidly, in less than a minute, with the amount of hydrate stabilizing quickly, after about 1 minute, at around 3%. This would suggest a positive correlation between water saturation and hydrate formation. The decrease in water also stabilized quickly, aligning well with the hydrate formation, as both the increase in hydrates and the decrease in water became steeper within approximately half a minute to a minute. The second cycle obtained a conversion factor of 3.8%.

Looking at the overall trend of the experiment depicted in Figure 5-7, a relatively stable situation is observed for both water and hydrates. An interesting observation occurs around 800 minutes (approximately 13 hours), where there's a slight increase in water saturation and a corresponding decrease in hydrates, but around 900 minutes (150 hours), they seem to balance out again as they did before this observation. This experiment ran for almost 1400 minutes (23 hours).

Finally, in Figure 5-8, the dissociation saturation graph of the first experiment, 2nd cycle, is displayed. Here, the temperature was increased in three steps. Initially, from 0 to 5°C. However, no significant change seems to have occurred. Subsequently, the temperature was raised to 8°C, gradually causing all hydrates to disappear. The temperature was further increased to 15°C to ensure complete removal, though this proved unnecessary as indicated by the results graph. The water shows a consistent pattern throughout. The dissociation started at 7.2 and ended at 7.3°C.
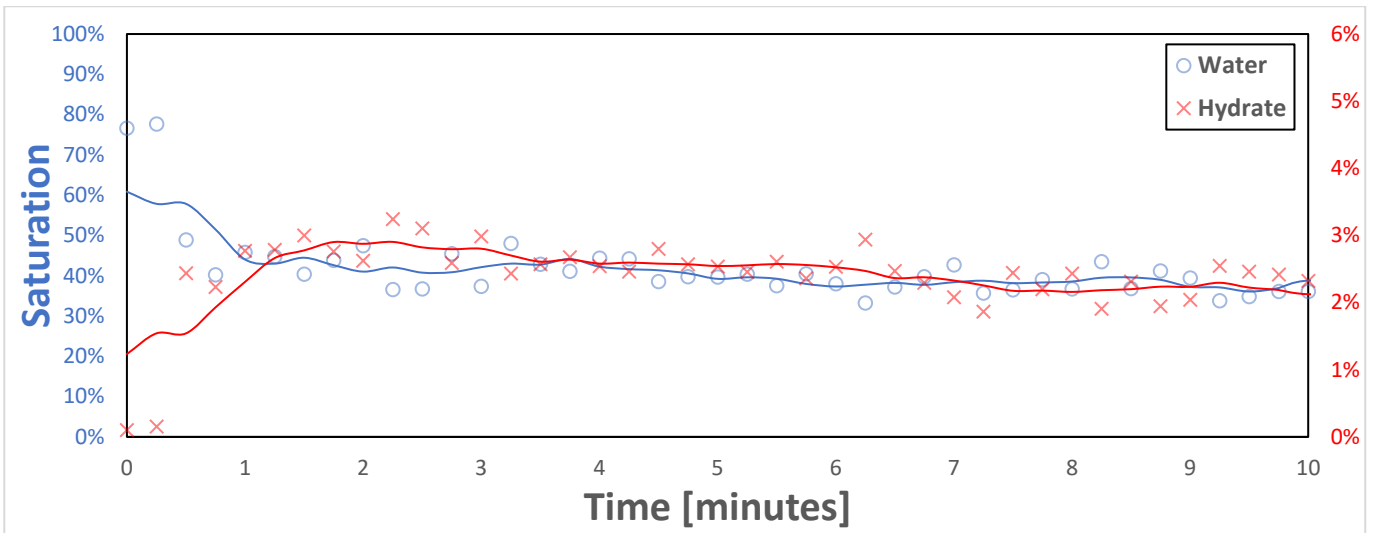
Figure 5-6 First experiment, second cycle, focused on the initial minutes of hydrate formation with the water saturation plotted on the left y-axis in blue and the hydrate saturation plotted in the right y-axis in red.
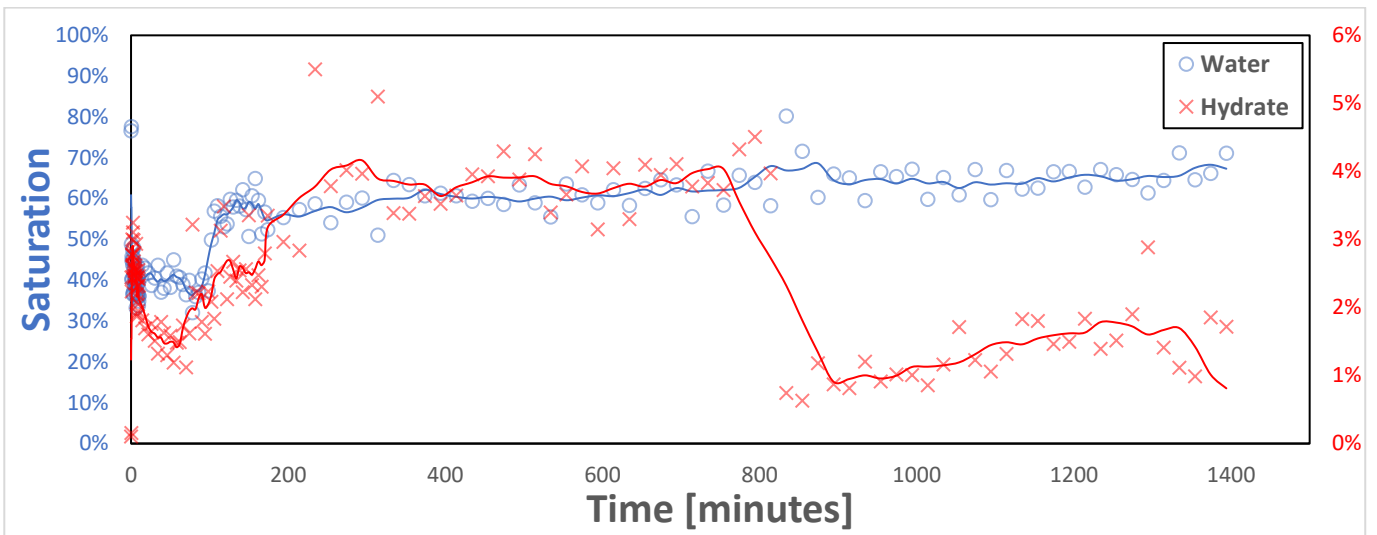
Figure 5-7 First experiment, second cycle, behavior over the complete cycle total with the water saturation plotted on the left y-axis in blue and the hydrate saturation plotted in the right y-axis in red.
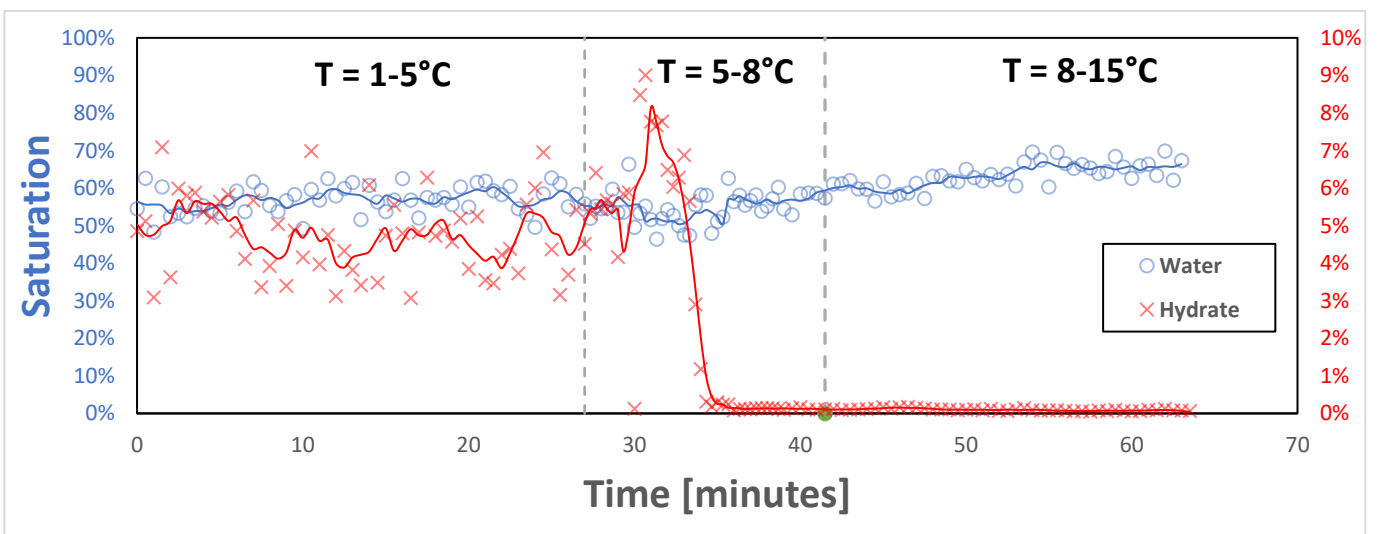
Figure 5-8 First experiment, second cycle, dissociation phase with the water saturation plotted on the left y-axis in blue and the hydrate saturation plotted in the right y-axis in red.
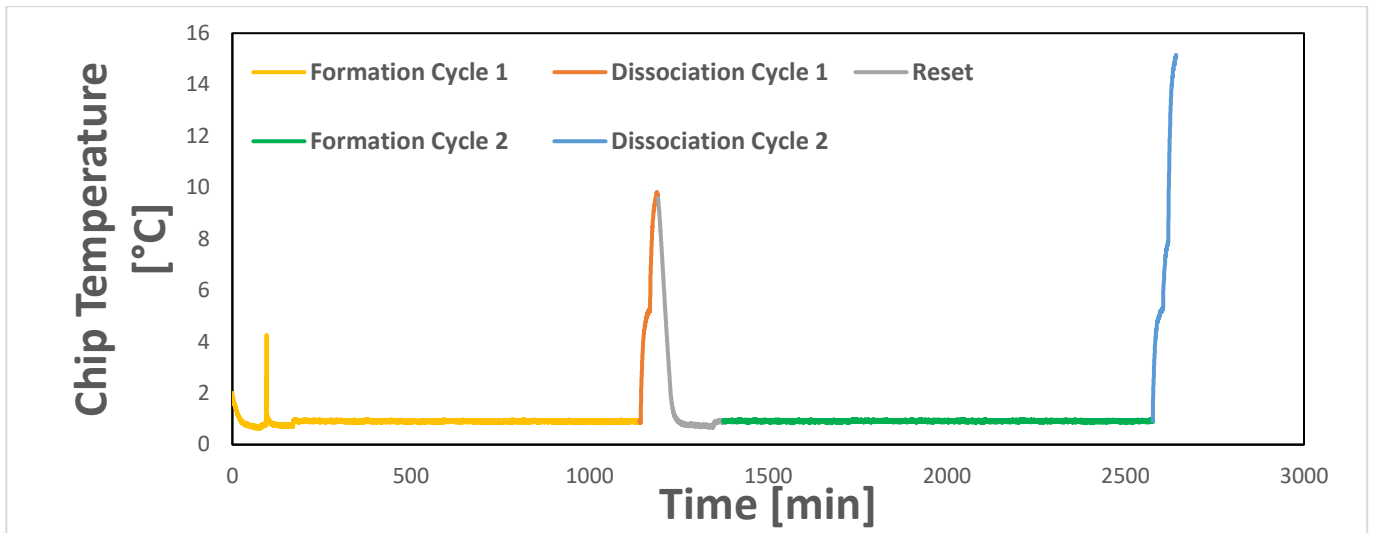
Figure 5-9 Temperature curve from the first experiment with manually controlled pressure

5.2.2 Second experiment with pressure pulse of 0.5 seconds

As previously mentioned, the second experiment was conducted with an electronic trigger giving a pressure pulse of 0.5 seconds. This method ultimately led to the least hydrate formation. However, this could also be partly due to a lower initial water saturation. As shown in Figure 5-10, which displays the first ~11 minutes of the formation saturation, this experiment had an initial water saturation of slightly less than 70%. It is clearly visible in the graph that as the water saturation decreases, after less than 2 minutes, the hydrate formation increases. The amount of hydrates remains fairly constant for the rest of the experiment. The whole formation is shown in Figure 5-11. The conversion factor is calculated to be 7%.

In Figure 5-12, the dissociation of this experiment is shown. It is observed that increasing the temperature to 5°C does not cause any change in the hydrate. However, when the temperature is increased from 5 to 10 degrees, a change is visible. First, a small narrow increase in hydrates is observed, which may have been caused by a blockage in the line that was resolved by the temperature increase, resulting in a small pressure pulse that triggered some hydrate formation. But shortly after this time the total dissociation of hydrates is observed. The dissociation started at 8.7 and ended at 8.9°C. The temperature graph is shown in Figure 5-16.
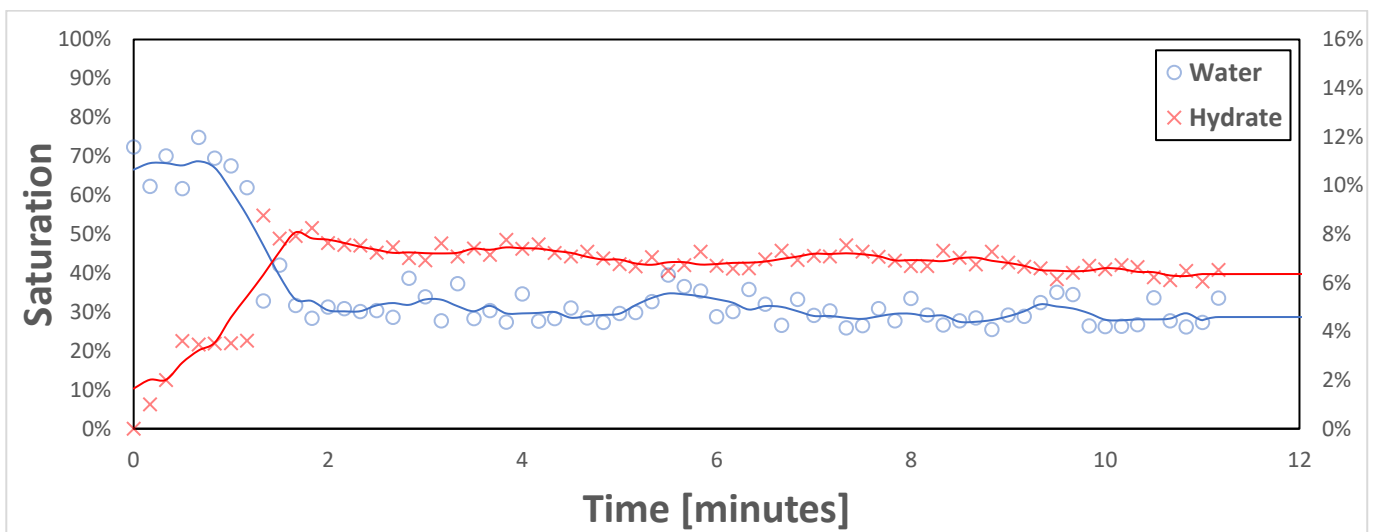
Figure 5-10 Second experiment first cycle, focused on the initial minutes of hydrate formation with the water saturation plotted on the left y-axis in blue and the hydrate saturation plotted in the right y-axis in red.
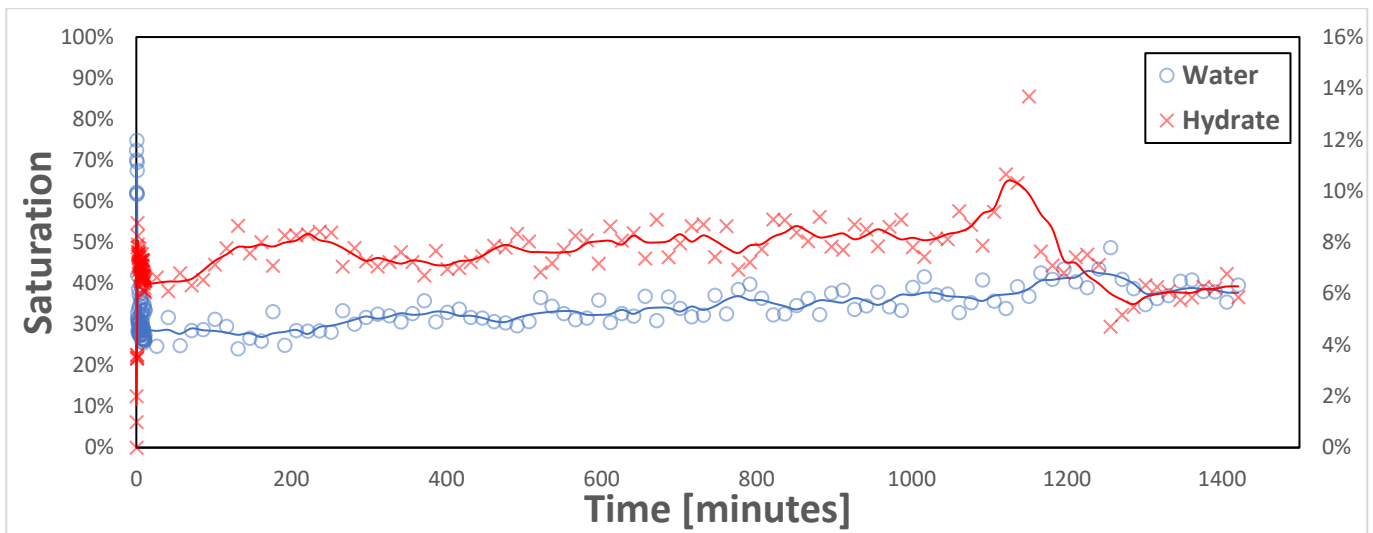
Figure 5-11 Second experiment, first cycle, behavior over the complete cycle with the water saturation plotted on the left y-axis in blue and the hydrate saturation plotted in the right y-axis in red.
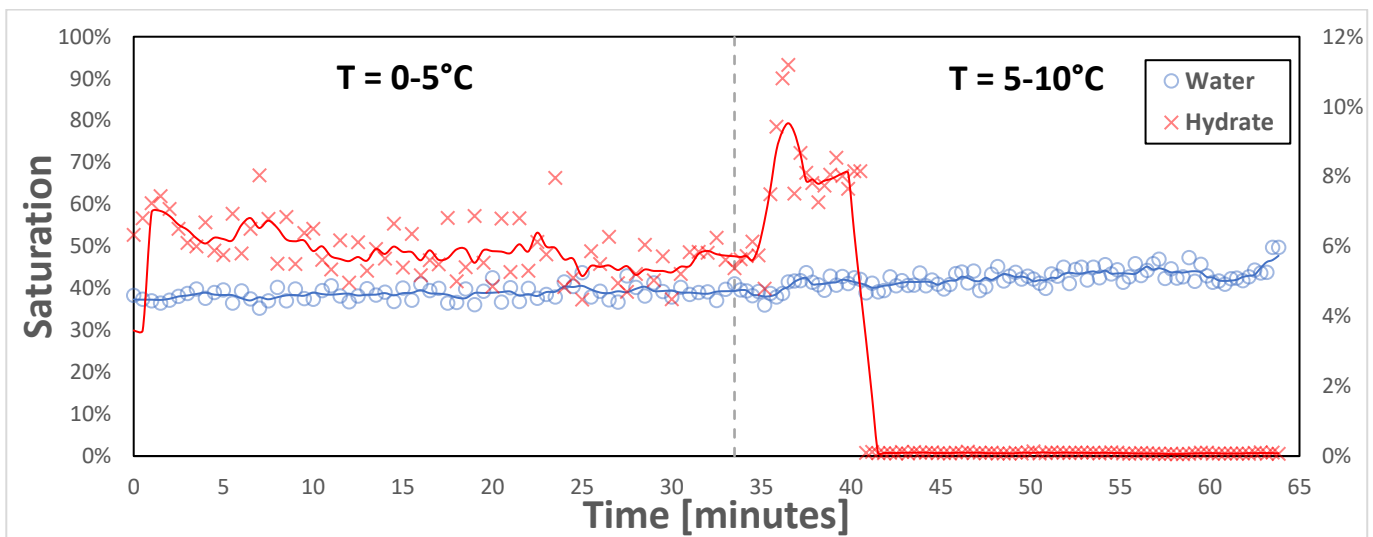
Figure 5-12 Second experiment, first cycle, dissociation phase with the water saturation plotted on the left y-axis in blue and the hydrate saturation plotted in the right y-axis in red.

The second cycle did not yield results that were significantly different to the first cycle, but the amount of hydrate was even lower than in the first cycle. Although the hydrate formed quickly, they only covered about 3.5% of the total microfluidic chip. The initial water saturation was also much lower, around 33%, and remained the same throughout the experiment. The overall progression remained constant. The results for the first 8 minutes are shown in Figure 5-13, and the entire formation is shown in Figure 5-14. The conversion factor is calculated to be 9.1%.

In Figure 5-15, the dissociation of this experiment is shown. For this experiment, it was divided into four temperature step increases. This was done because it was very unclear from the images whether there were hydrates or not, so the cautious approach was taken. However, the processed images indicate that this was unnecessary and that everything had already dissociated during the temperature increase from 5 to 8°C. The actual dissociation started at 7.1 and ended at 7.3°C. The temperature curve is given in Figure 5-16.
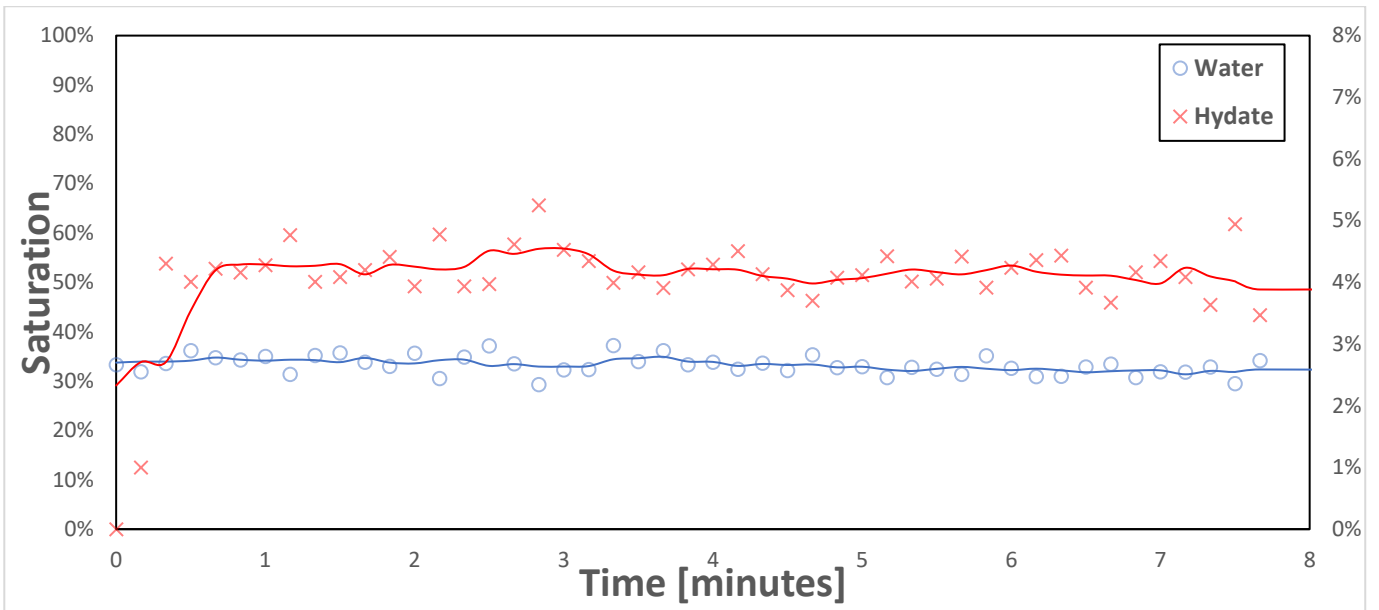
Figure 5-13 Second experiment, second cycle, focused on the initial minutes of hydrate formation with the water saturation plotted on the left y-axis in blue and the hydrate saturation plotted in the right y-axis in red.
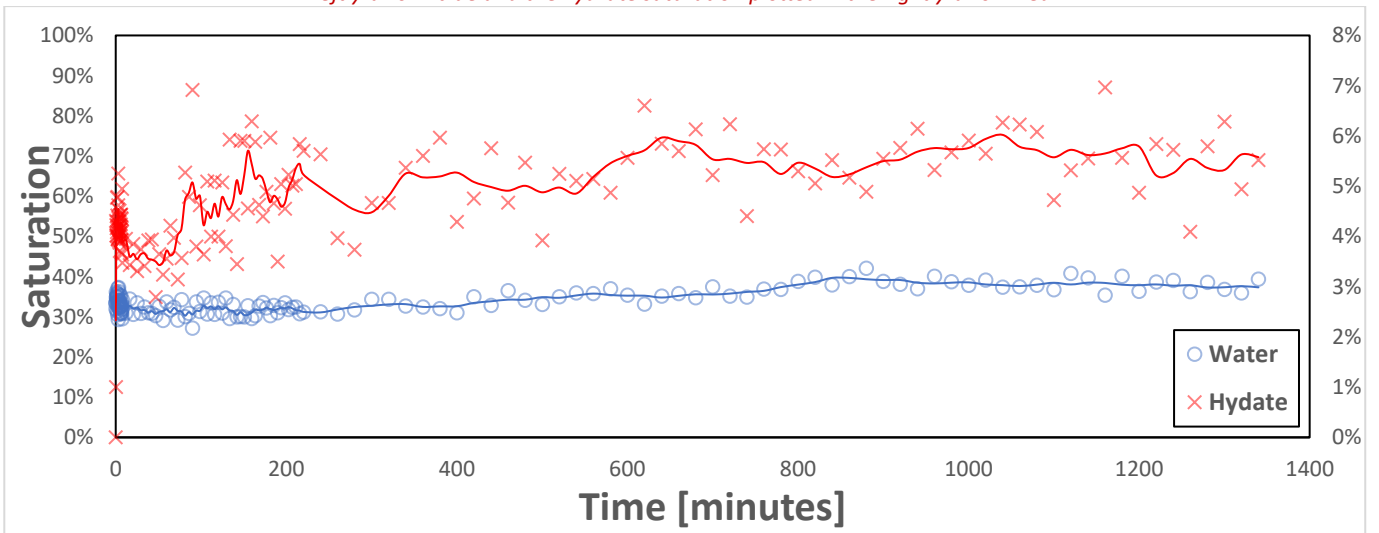
Figure 5-14 Second experiment, second cycle, behavior over the complete cycle with the water saturation plotted on the left y-axis in blue and the hydrate saturation plotted in the right y-axis in red.
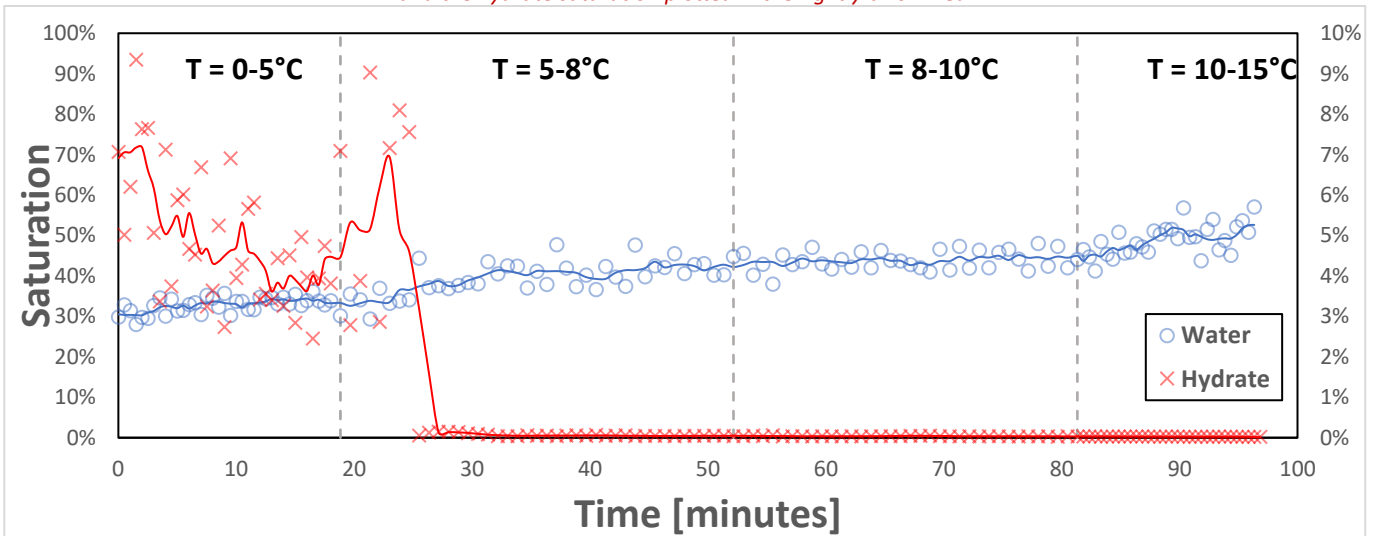
Figure 5-15 Second experiment, second cycle, dissociation phase with the water saturation plotted on the left y-axis in blue and the hydrate saturation plotted in the right y-axis in red.
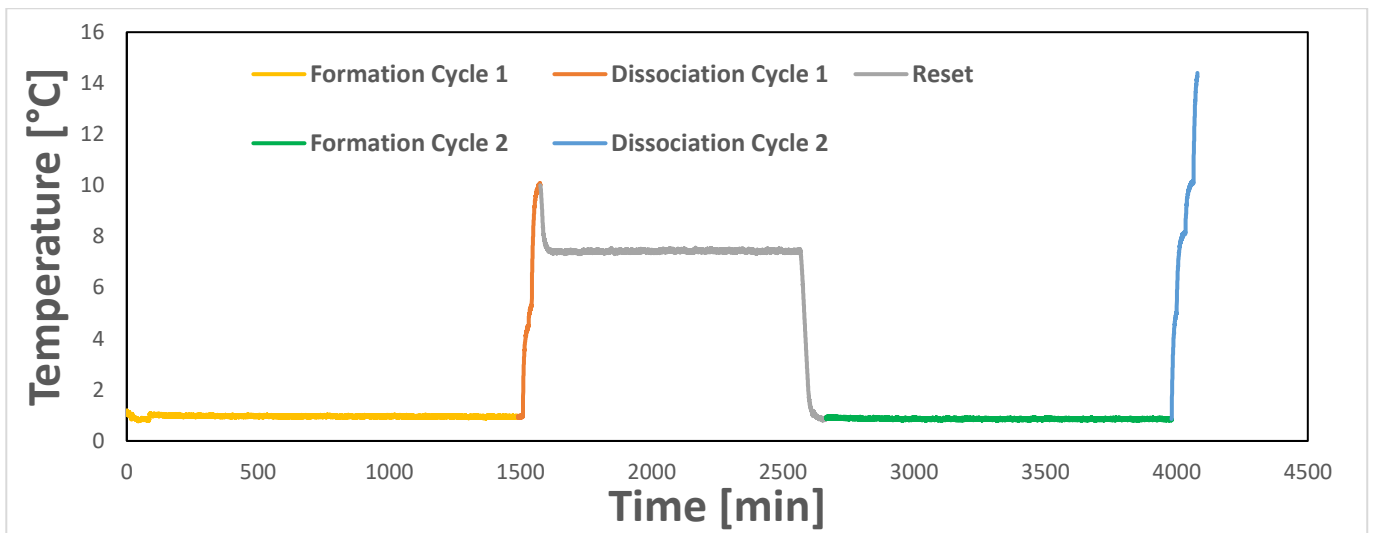
Figure 5-16 Temperature curve from the second experiment with pulse trigger mode of 0.5 seconds

5.2.3   Third Experiment with pressure pulse duration of 0.2s

The third experiment was conducted using a pressure pulse of 0.2 seconds. Hydrate formation in this experiment did not occur in the first minute but started around the 5-minute mark. The amount of hydrates reached about 8% and remained stable until around 14 minutes. After this, a slight decrease is observed in the curve in Figure 5-17. The saturation then continued to drop to about 5% as seen in Figure 5-18, which shows the rest of the experiment's progress. The situation stabilized again around 200 minutes (around 3 hours). The initial water content was 80%, which had a slightly declining trend even before the hydrates formed and remained stable at ~55% during the formation of the hydrates until 15 minutes, when the hydrates showed a weak decrease, after which the water showed a slight increase. The rest of the experiment, shown in Figure 5-18, indicates that the water then found a balance again at about 60%. The conversion factor is 5.9%.

The dissociation of this experiment can be seen in Figure 5-19. It shows that the experiment was held at a temperature increase from 0 to 5°C for half an hour, which had no effect. When the temperature was raised to 10°C, it is observed that the hydrates began to dissociate. This occurred quite quickly; the dissociation started at 5.3°C and continued until it reached 7.3°C, after which all hydrates from the experiment were gone. The temperature graph of this experiment is shown in Figure 5-23.
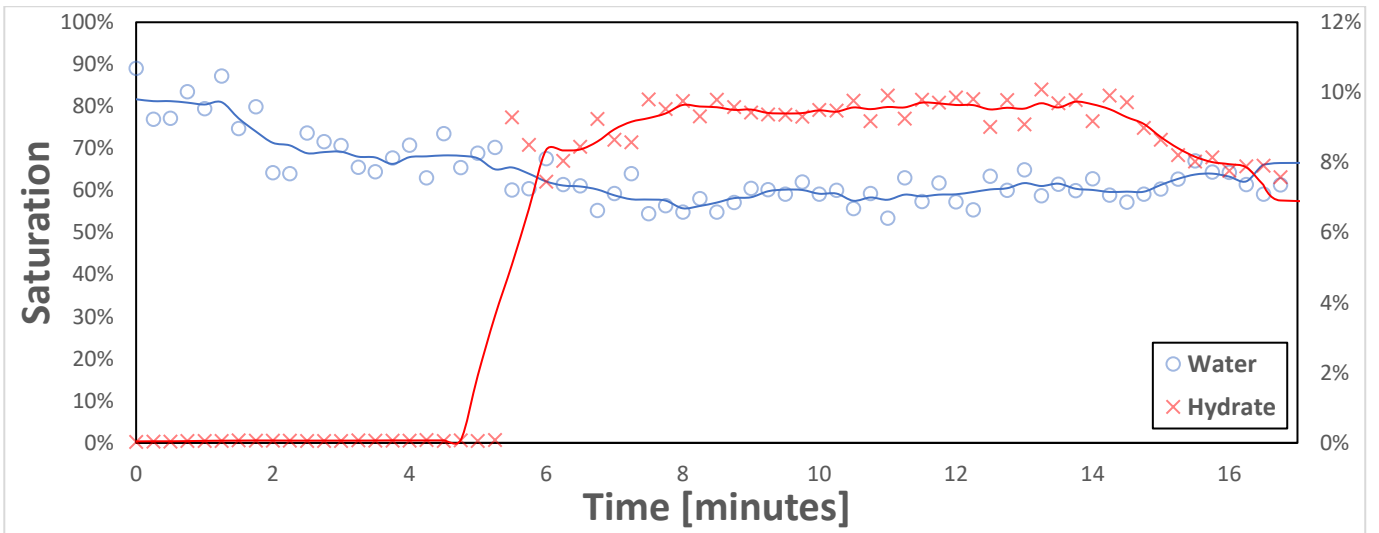
Figure 5-17 Third experiment, first cycle, focused on the initial minutes of hydrate formation with the water saturation plotted on the left y-axis in blue and the hydrate saturation plotted in the right y-axis in red.
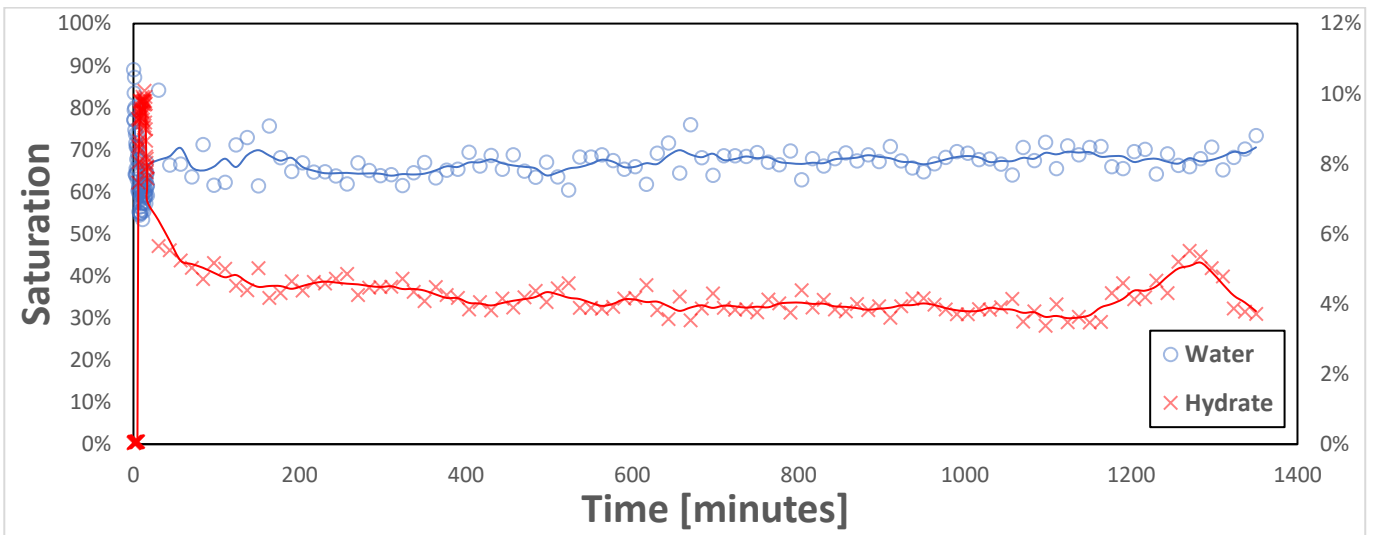
Figure 5-18 Third experiment, first cycle, behavior over the complete cycle with the water saturation plotted on the left y-axis in blue and the hydrate saturation plotted in the right y-axis in red.
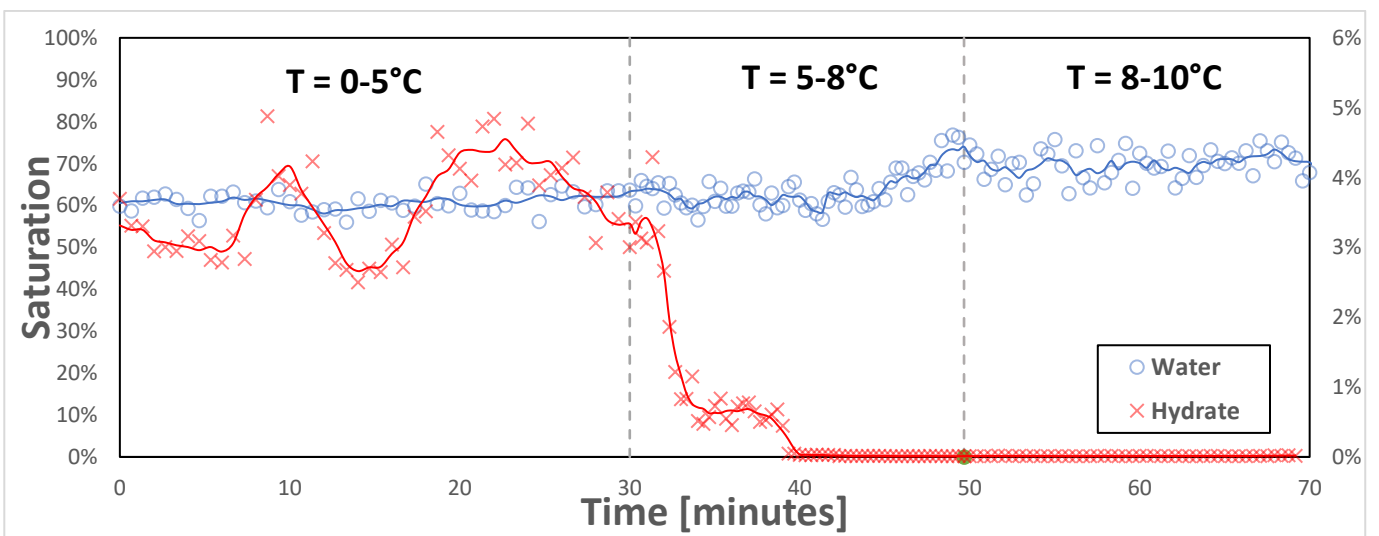
Figure 5-19 Third experiment, first cycle, dissociation phase with the water saturation plotted on the left y-axis in blue and the hydrate saturation plotted in the right y-axis in red.

The second cycle of the third experiment was particularly noteworthy. The water started at 60% and immediately began to decrease after initiation of hydrate formation, resulting in a significant amount of hydrates. However, this large saturation of hydrate formed a peak, as the hydrate saturation subsequently decreased to around 10%, and the water saturation increased to around 80%, as shown in Figure 5-20. Figure 5-21 then illustrates the remainder of the experiment's progression. The water content slightly increased to around 90%, and the system remained constant up to approximately 750 minutes, or 12.5 hours. After this point, both the water and hydrate levels decreased, which is unusual and suggests that more gas entered the system. However, it could also indicate that the water and hydrates moved more into the inlet and outlet, which are not accounted for in the image processing and thus not reflected in the graph. The hydrates quickly reformed to around 8%, and the water experienced a peak rise at approximately 1220 minutes, or 20 hours. During this increase, the water reached a value of around 90%, similar to the initial value. Afterward, the water content fluctuated but less severely, and by around 2000 minutes, or 33 hours, the water content stabilized at around 80%. The maximum conversion factor for this experiment was calculated to be 10.4%.

Figure 5-22 shows the dissociation of this experiment. It can be seen that heating to 5°C had no effect. When the temperature was increased to 8°C, there was a sudden increase in hydrates when the temperature reached 5.5°C. This can be explained by a blockage in the line that was resolved by the temperature increase, leading to a pressure pulse. After reaching 6.72°C, all hydrates were dissolved. However, when the temperature was further increased to 10°C, there was another increase in hydrates at 9.3 degrees, which can be explained by the same principle. After reaching 9.5 degrees, all hydrates in the entire experiment were dissolved again.
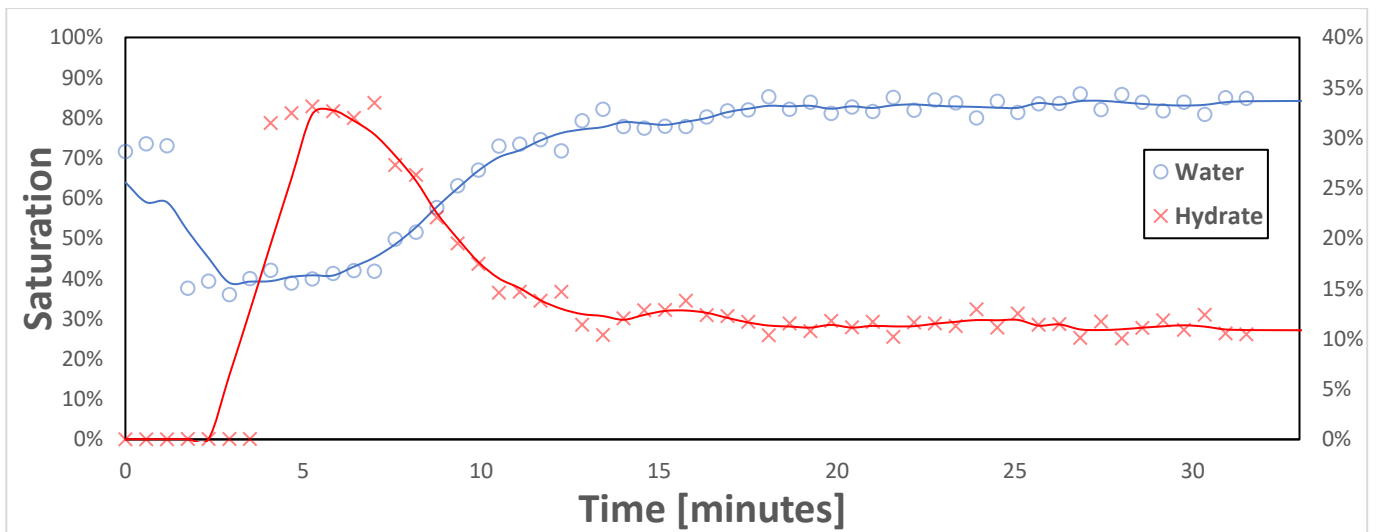
Figure 5-20 Third experiment, second cycle, focused on the initial minutes of hydrate formation with the water saturation plotted on the left y-axis in blue and the hydrate saturation plotted in the right y-axis in red.
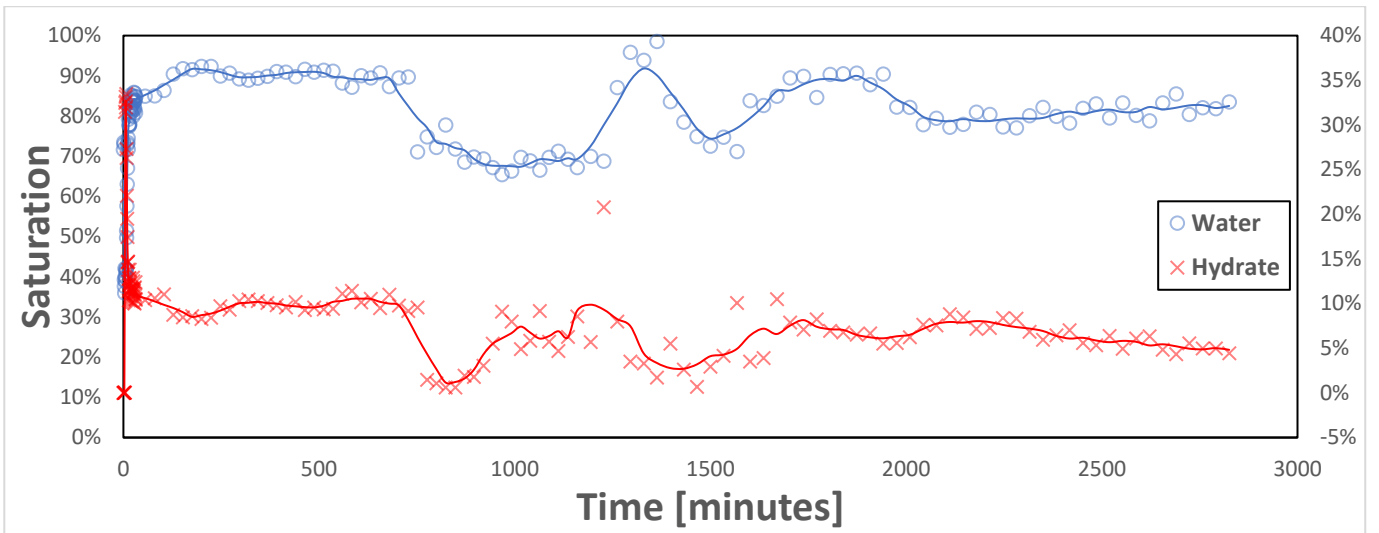
Figure 5-21 Third experiment, second cycle, behavior over the complete cycle with the water saturation plotted on the left y-axis in blue and the hydrate saturation plotted in the right y-axis in red.
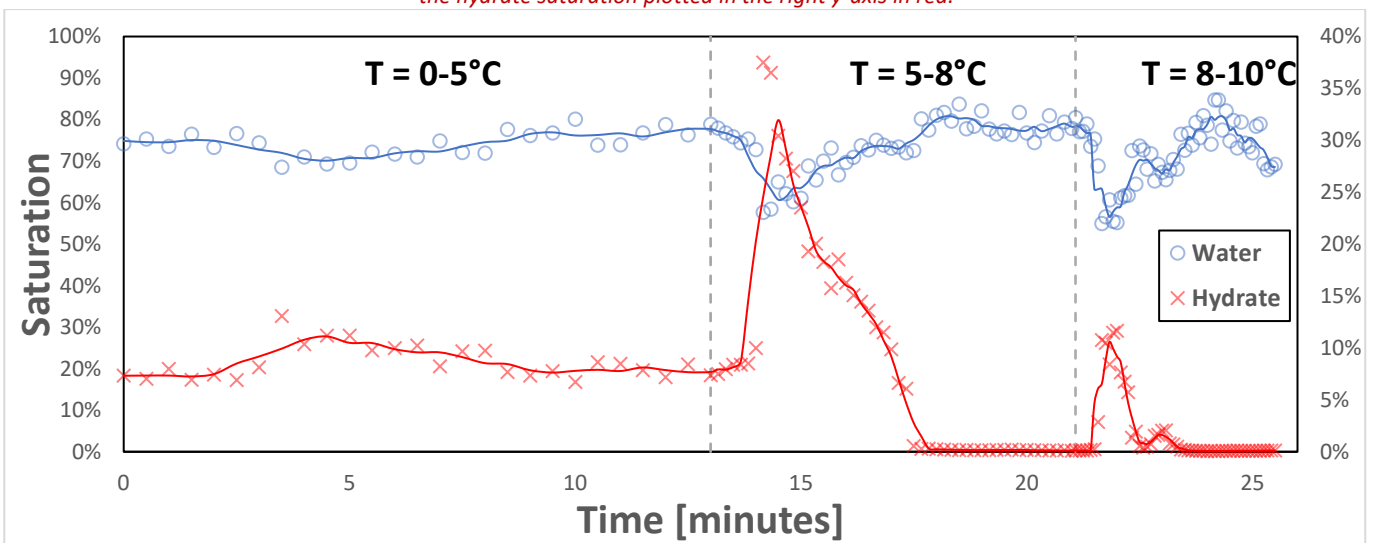
Figure 5-22 Third experiment, second cycle, dissociation phase with the water saturation plotted on the left y-axis in blue and the hydrate saturation plotted in the right y-axis in red.
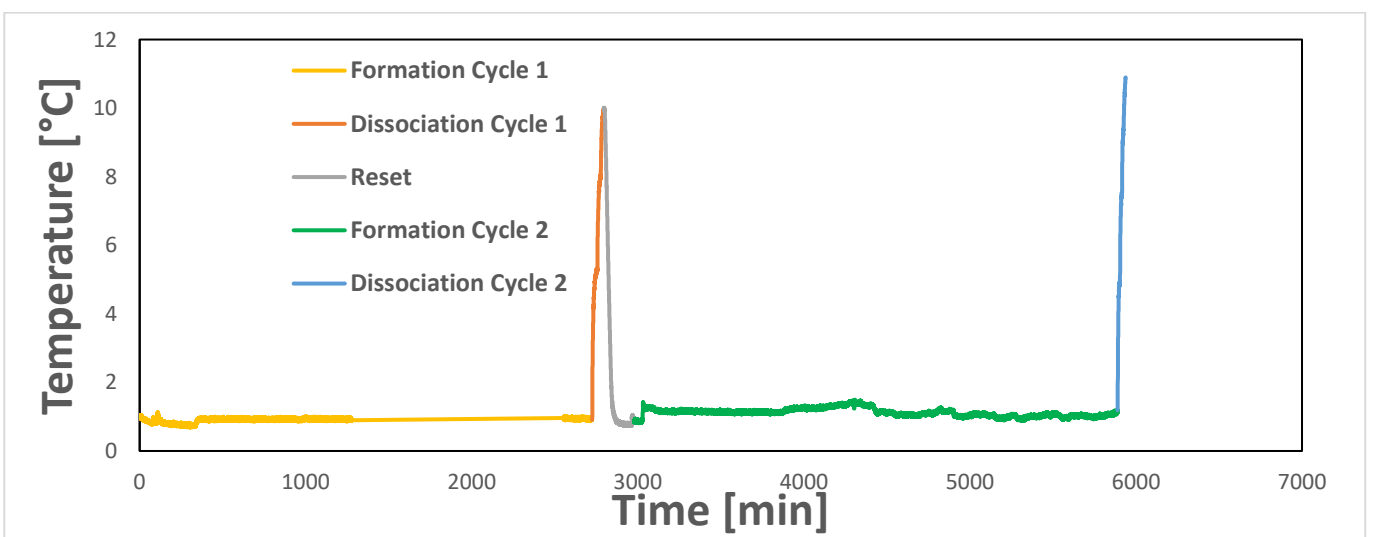
Figure 5-23 Temperature curve from the third experiment with pulse trigger mode of 0.2 seconds with the water saturation plotted on the left y-axis in blue and the hydrate saturation plotted in the right y-axis in red.

5.3 Summary of Results Hydrates

In Table 5-1, an overview of all the experiments and their results is provided. This table can also be found in appendix D.

Table 5-1 Overview of all hydrate experiments with obtained results

Experiment	Cycle	Flowrate [mm/s]	Max. water	Max. Hydrate	Conversion factor	Dissociation start temperature [°C]	Dissociation end temperature [°C]
1st	1	0.237	90%	16%	10.0%	8.7	8.8
1st	2	0.237	60%	3%	3.8%	7.2	7.3
2nd	1	0.365	70%	8%	7.0%	8.7	8.9
2nd	2	0.365	35%	5%	9.1%	7.1	7.3
3rd	1	0.217	80%	9%	5.9%	5.3	7.3
3rd	2	0.217	70%	33%	10.4%	5.5	6.7

6   Discussion

In this chapter, the research questions and corresponding sub-questions posed in the introduction are discussed. First, all questions regarding the salt dry-out will be reviewed, followed by the questions regarding the Hydrates.

6.1   Salt dry-out

6.1.1   Sub-questions

6.1.1.1   *How do these mechanisms affect the spatial distribution of salt precipitation?*

From the distribution of the locations of both water and salt precipitation from the various experiments, a trend is evident as shown in Figure 6-1. Where the most water remained present for the longest duration is very often, nine out of ten times, on the outlet side. The occurrence of the most salt is somewhat more evenly distributed, but still predominantly on the inlet side. This is due to the decrease in local porosity and permeability as a result of salt nucleation and aggregation, leading to differences in capillary forces that causes water movement from the region with higher water saturation to the region with lower water saturation (Yan et al., 2024). As discovered in earlier experiments conducted by Lifei Yan without the heating box (using a simple heating plate instead), these distributions remained the same, indicating that the heating box had no effect on the locations of salt precipitation (Yan et al., 2024).
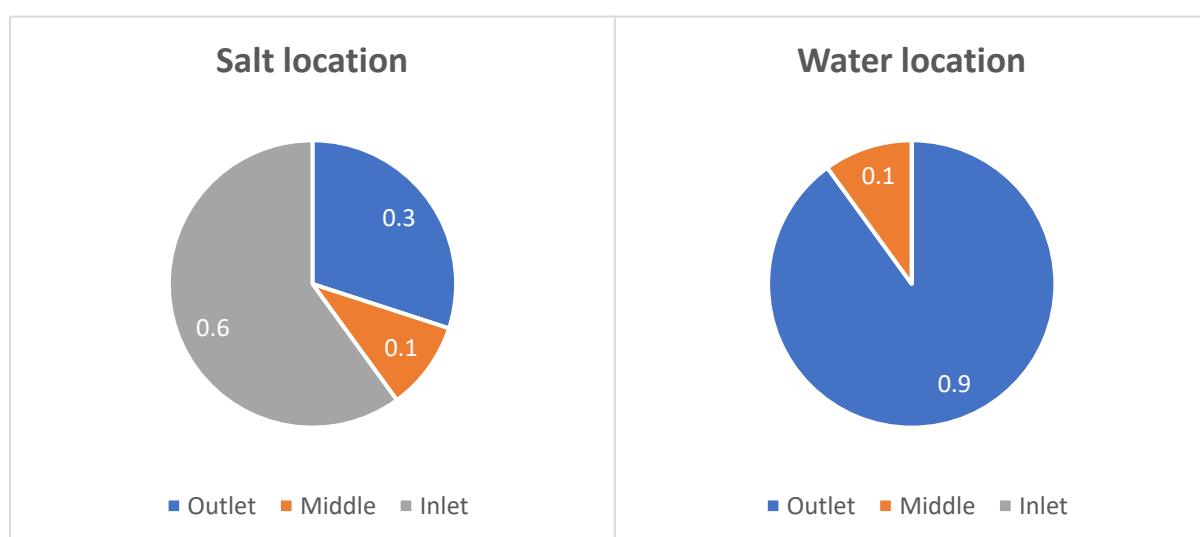
Figure 6-1 Pie charts showing the location of the higher salt or water saturation for all experiments.

Another notable observation is that in some situations when the water backflow was small, it did not affect the total amount of salt precipitation. However, when it exceeded the initial maximum water value, it became the dominant factor influencing the resulting amount of salt.

It was seen that the time until total dry-out showed a large variance with values ranging from 12 to 133 hours. This can be explained by the differences in water distribution in the microfluidic chips. If the water is better distributed throughout the microfluidic chip, the evaporation is faster compared to when all the water accumulates on one side or in one spot of the microfluidic chip. Yet interestingly, the experimental duration is quite constant per chip, with only one exception. This exception was

caused by a water reservoir in the middle of the chip resisting dry-out. This high variance of dry-out time between chips, combined with the low variance per chip, show the large influence of pore geometry on salt precipitation processes.
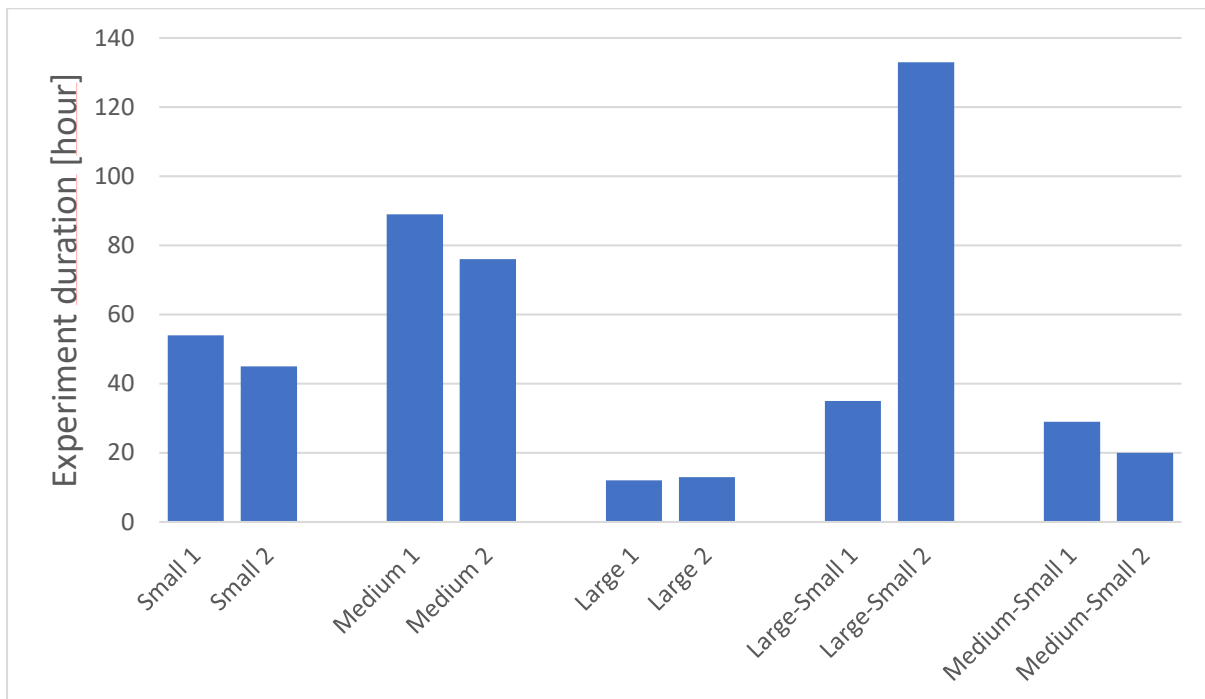
Figure 6-2 Experimental duration in hours for all experiments.

6.1.1.2   *What is the impact of rock pattern and pore geometry on salt precipitation?*

The more water measured in the same microfluidic chip, the higher the salt content. In all the microfluidic chips, a higher salt percentage was measured in the experiments with more water. For example, the difference between the two small pore size microfluidic chips is very clear. As shown in Figure 6-3, the first experiment of these had a maximum water saturation measured at 74%, resulting in a salt precipitation of 7%, while the second experiment had a maximum water saturation measured of 49%, resulting in a salt precipitation of 4%. This is also the case with the heterogeneous microfluidic chips, for example looking at the large-small pore size microfluidic chips, the first experiment had a maximum water saturation of 94%, resulting in a salt precipitation of 12%, and the second experiment had a maximum water saturation of 53%, resulting in a salt precipitation of 9%. The medium-small pore size microfluidic chips both had lower maximum water saturation but close to each other (37% and 31%), this resulted in a total microfluidic chip salt precipitation of 8% in both cases. In the homogeneous microfluidic chips, it has been shown that the larger the pore size of the microfluidic chip, the more salt precipitates. In the heterogeneous microfluidic chips, the opposite is true i.e. the large the pore size, the smaller the amount of salt that precipitates. This is further explained in sub-question 6.1.1.3.
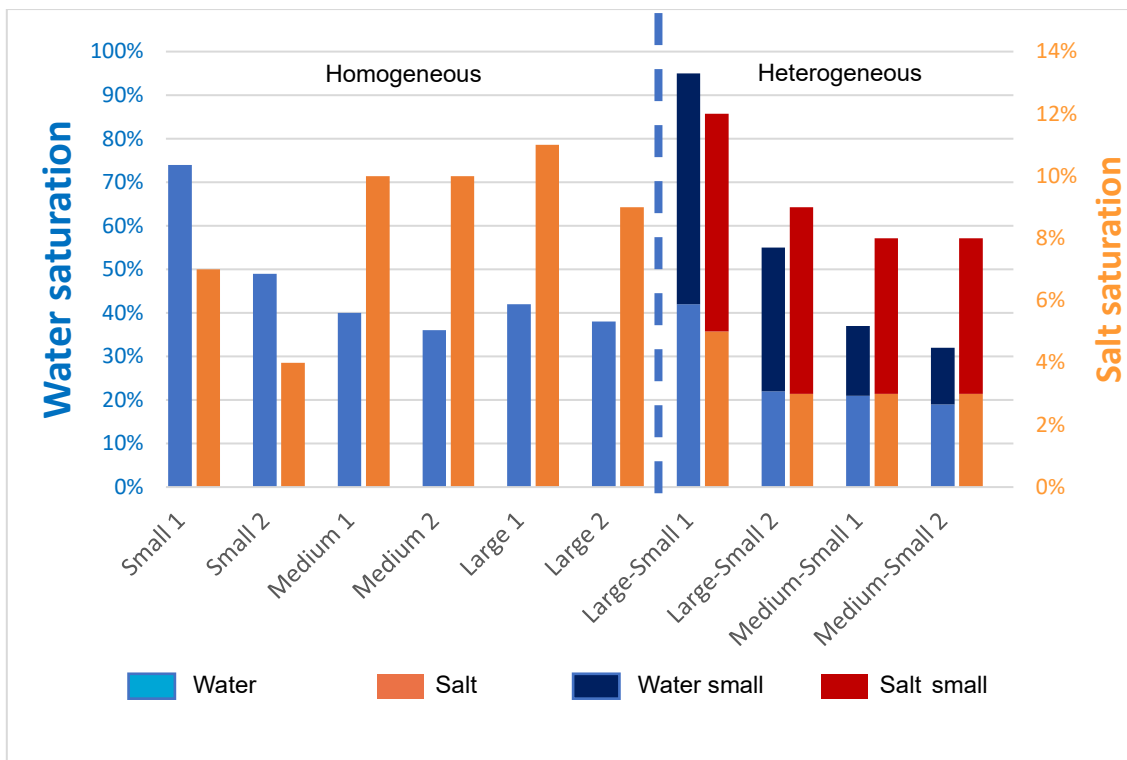
Figure 6-3 Overview measurements, in blue the water saturation with values on the left y-axis, in orange the salt saturation with values on the right y-axis. The stack bars represent the heterogeneous chips, divided into the two pore size regions.

6.1.1.3   How does the heterogeneity affect dynamics of salt precipitation?

The homogeneous and heterogeneous microfluidic chips show a striking difference in dehydration behavior. Figure 6-3 shows that whereas the homogeneous microfluidic chips exhibit a higher or equal percentage of salt as the pore size microfluidic chip increases (the percentages of the medium pore size microfluidic chips are higher than those of the narrow pore size microfluidic chips, and the percentages of the large microfluidic chips are equal to the percentages of the medium pore size microfluidic chips), it is the opposite with the heterogeneous microfluidic chips. In the heterogeneous microfluidic chips, it can be observed that in the large-small microfluidic chips, the salt content shows a higher percentage on the small pore side than on the large pore side. And in the medium-small microfluidic chips, it can be seen that the small pore side also exhibits more salt than the medium pore side. The impact of heterogeneity is thus that the salt content per pore size shows inverse values. This could be explained by the impact of capillary pressure, which results in a higher water saturation for smaller pores, resulting in higher salt precipitation. For example, the large-small microfluidic chip showed a water saturation of 42 and 53% and a salt saturation of 5 and 7% in the respective large and small pore size parts.

6.1.1.4   How can the insights gained from this study be utilized to enhance the efficiency of CCS?

Insights gained from this research on salt precipitation experiments can be utilized in various ways to enhance the efficiency of CCS technologies. For instance, it has been observed that temperature has little effect on the location of precipitation, but because of the water distribution and corresponding evaporation the location varies over time. Insights gleaned from this research, such as the difficulties of having a large saturation of water present in the reservoir, consistently resulted in higher levels of salt precipitation. This knowledge can facilitate prevention of well plugging, improving the chances of successful CO_2 injection.

6.1.2 What are the mechanisms governing salt precipitation observed in heated microfluidic systems?

The experimental observations shed light on the spatial distribution of salt precipitation within microfluidic channels. While water tends to accumulate predominantly on the outlet side of the microfluidic chip, salt precipitation exhibits a more even distribution, albeit with a slight bias towards the inlet side. The use of a heating box, where the air around the microfluidic chip is heated, as opposed to a heating plate underneath the microfluidic chip, has been found to have negligible effects on the locations and, surprisingly, speed of salt precipitation. Instead, the amount and distribution of water within the microfluidic chip emerge as critical determinants, affecting evaporation rates and, consequently, salt precipitation dynamics. Moreover, the interplay between water backflow and salt precipitation reveals a nuanced relationship, with small backflow not necessarily correlating with increased salt precipitation.

The impact of rock pattern on pore geometry further complicates the salt precipitation dynamics. Experiments demonstrate a direct correlation between water content and salt concentration, with microfluidic chips exhibiting higher water saturation consistently yielding higher salt percentages. This trend holds true across various microfluidic chip configurations, with smaller pore sizes generally resulting in lower salt precipitation. Notably, however, heterogeneous microfluidic chips exhibit inverse behavior as compared to homogeneous microfluidic chips. For these microfluidic chips, larger pore sizes correlate with relatively lower salt precipitation due to favorable flow dynamics during CO_2 injection, which flushes brine more effectively from the larger pores. This differential behavior highlights the importance of pore-scale heterogeneity in influencing salt precipitation dynamics.

6.2 Hydrate formation

6.2.1 Sub-questions

6.2.1.1 How does this kinetics elucidate the mechanisms of hydrate formation and dissociation?

In the first experiment with manual pressure pulse control, hydrates formed rapidly as soon as pressure was sufficiently reduced. This experiment highlighted the sensitivity of hydrate nucleation to pressure fluctuations, with rapid formation indicating a highly reactive nucleation process. The resulting saturations of water and hydrate is given in Figure 6-4. The manual operation of a tap for venting high-pressure CO_2 led to an undefined time interval and a lack of precise control, suggesting that more uniform pressure reduction might stabilize the nucleation process. However, the observation of the rapid onset of hydrate formation under these fluctuating conditions underscores the critical role of pressure in hydrate stability.

The second and third experiments employed a trigger mode to control the pressure pulse, providing a more structured insight into the kinetics of hydrate formation. In the second experiment, utilizing a 0.5-second trigger mode, fewer hydrates formed, suggesting that the longer interval between pressure spikes might not have sufficiently disturbed the system to support extensive nucleation. This could also be due to an insufficient level of supersaturation during these intervals, hindering widespread hydrate formation.

Conversely, the third experiment with a 0.2-second trigger mode showed more effective hydrate formation. The shorter interval likely caused more intense pressure perturbations, leading to rapid supersaturation and enhanced nucleation. This consistent triggering provided a more uniform kinetic environment, potentially more conducive to hydrate formation compared to the manual trigger. However, this would not explain the high number of hydrates in the first experiment although that might be explained by the high water saturation. More research is needed.
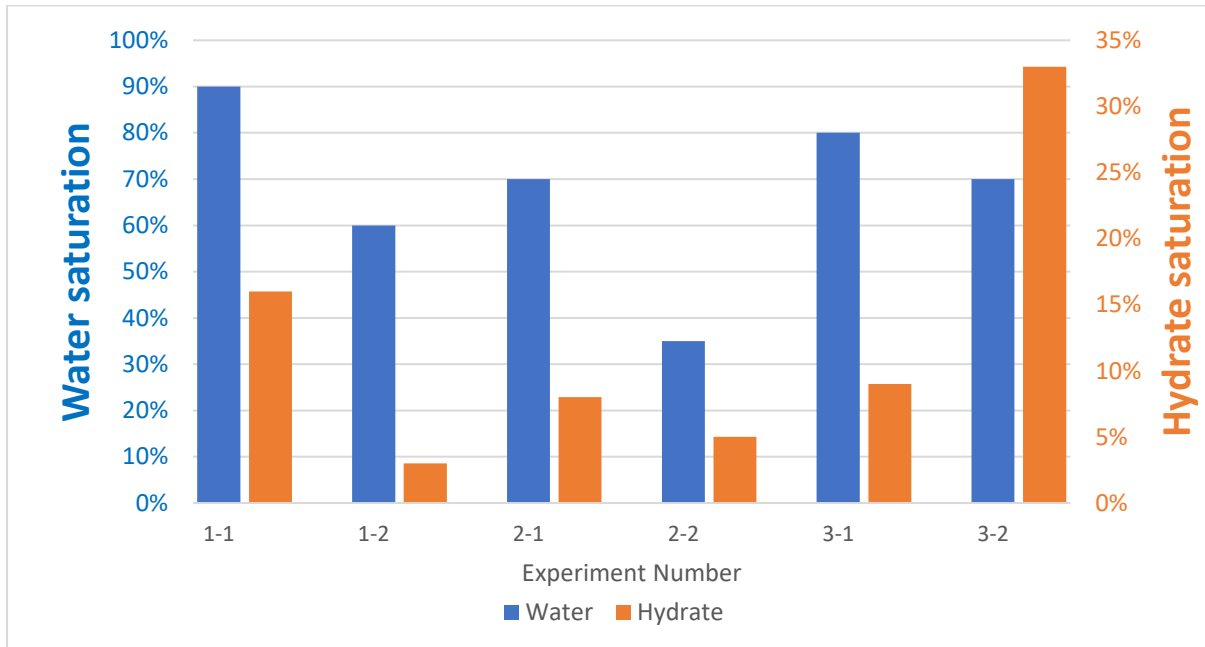
Figure 6-4 Bar graph showing water (blue, left axis) and hydrate (orange, right axis) saturations for all 3 experiments and 2 cycles.

Dissociation kinetics were also observed through temperature increases in all experiments. Hydrates began dissociating at specific temperatures, consistently identified across the experiments. Dissociation commenced from 5.3°C to 8.7°C. It was shown that minor temperature fluctuations as small as 0.1°C can significantly impact hydrate integrity.
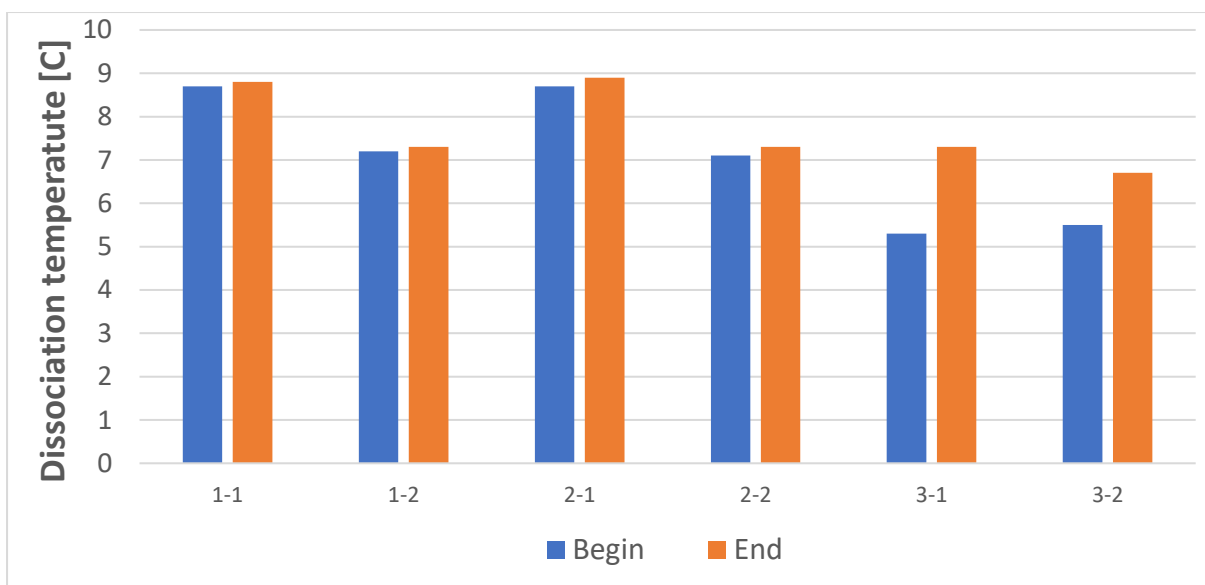
Figure 6-5 Bar graph showning dissoiation temperatures of all 3 experiments and 2 cycles.

Overall, the kinetics observed in these experiments, particularly the effects of controlled pressure adjustments and temperature changes, highlight the dynamic nature of hydrate formation and dissociation. These results underscore the importance of system conditions in determining the rate and extent of hydrate nucleation and dissociation, showing that both pressure and temperature are critical parameters governing these mechanisms.

6.2.1.2 What types of hydrate morphologies can be observed?

In this study, various hydrate morphologies have been observed as shown in Figure 5-2. The formation of hydrates within a micromodel significantly differs from that in drying experiments where salt crystals typically appear as a sort of 'blobby interface'. Contrarily, hydrates in the micromodel present themselves with diverse structures.

Detailed analysis reveals that many hydrate structures previously described in the literature are also present in our model. These include morphologies such as pore-filling, where hydrates grow freely in the center of a pore; load-bearing, where hydrates form point contacts with adjacent grains in the center of a pore; grain-cementing, where hydrates cement the grains together; grain-coating, where hydrates grow uniformly around and on the surface of the grains; and patchy, where hydrates locally cluster into larger crystals.

Notably, our results have showed a 'sheet-like' hydrate structure, which could not be found in literature. This structure distinctly differs from the traditionally recognized forms and points to possible alternative formation processes, hydration number or environmental influences that have not been fully explored yet.

These observations underscore the complexity and diversity of hydrate morphologies and suggest that there is much to learn about the conditions and processes influencing their formation. Identifying new structures such as the 'sheet-like' hydrates opens new avenues for further research into hydrate dynamics and stability in geological systems.

6.2.1.3 How can the insights gained from this study be utilized to enhance the efficiency of CCS?

One significant finding is the importance of precise control over pressure conditions. The experiments demonstrated that a reduced trigger interval from 0.5 seconds to 0.2 seconds led to more hydrate formation. Implementing precise and automated pressure controls preventing such pulses in CCS operations could lead to less hydrate formation, thereby enhancing the efficiency of carbon storage. However, it is worth noting that more research is needed to precisely quantify the effect. Lastly, the categorization of different hydrate morphologies, including a novel 'sheet-like' structure, provides deeper insights into the physical properties and stability of hydrates. These morphological insights are crucial for predicting and preventing hydrate-based blockages of CO_2 storage. Overall, the data and findings from this study not only deepen our understanding of the physical and chemical dynamics of CO_2 hydrates but also pave the way for innovative approaches to optimize and scale CCS technologies. These enhancements could lead to more robust, efficient, and safer carbon storage solutions, significantly impacting global efforts to mitigate climate change.

6.2.2 What factors influence the growth of CO_2 hydrates in microfluidic systems?

The growth of CO_2 hydrates in the microfluidic system was influenced by several key factors. The two most important factors are pressure and temperature, and CO_2 hydrate formation exhibits a high dependence on these factors. In microfluidic systems, precise control over these parameters was

crucial as it significantly impacts the growth kinetics and stability of the hydrates. Additionally, the flow rate of CO_2 and water within the microfluidic channels played a vital role in determining the rate and extent of hydrate formation. Furthermore, the design and surface properties of the microfluidic channels were significant contributors to hydrate formation dynamics. Surface interactions could influence nucleation and growth kinetics, with different geometries providing varied nucleation sites and growth conditions. It's worth noting that in this experiment, only one type of microfluidic chip was used, hence the channel geometry and surface properties were not varied.

Additionally, it was observed that pressure pulses influence the hydrate formation. Each hydrate crystal, like ice, requires a starting point, a nucleation site, where the initial molecules manage to form the correct structure together. Once this happens, more molecules join in the same arrangement, allowing the crystal to grow. The exact timing and manner in which this initial nucleation occurs and triggers the hardening process is somewhat of a mystery. In the example of a bottle of water placed in a freezer, if you hit the supercooled bottle, you disturb the system, causing nucleation to occur. The pressure pulse for hydrate formation acts like the hit on the bottle, providing the necessary disturbance for the water molecules to connect and nucleate. Therefore, the shorter the pressure pulse, the greater the shock, and the more hydrate formation is expected.

7   Conclusions and Recommendations for Future Work

This study aimed to shed light on two phenomena hindering effective CCS in subsurface reservoirs: Salt dry-out and Hydrate formation. For this purpose, experiments were done using microfluidic models.

7.1   Salt dry-out

It was found that salt dry-out is most dependent on initial water saturation. While the water tends to accumulate on the outlet side, the salt is distributed over the entire microfluidic chip. It was found that the heating box had very little impact when compared to previous studies. It was also found that a smaller pore size leads to a lower salt saturation, yet only in a homogenous microfluidic chip. In a heterogeneous case, the salt concentrates in the smaller pores.

For salt dry-out, many questions still remain. These questions might become the basis for future work. Next to these questions, there are many points with which the experiment setups and methodology can be improved. The recommendations improvements are listed below:

- **Refinement of microfluidic chip designs**: The unexpected invariability in permeability observed across different microfluidic chip designs underscores the need for further research into the effects of microfluidic chip thickness on fluid dynamics. A redesign of the microfluidic chips, incorporating increased thicknesses, would likely yield more insightful data on salt crystallization patterns and on their influence on permeability.

- **In-depth analysis of pore geometry**: The structure and distribution of pores within the microfluidic chips play a critical role in salt formation. An enhanced analytical approach to understanding pore geometry could lead to more insight.

- **Flow rate optimization**: The current setup does not allow for controlled and measurable CO_2 flow rates. Integrating flow sensors into future experiments could provide a more precise control and data collection, enhancing the reliability and repeatability of results.

- **Improvements in lighting and imaging techniques**: Enhancing the lighting and imaging methodologies could significantly improve the accuracy and efficiency of data processing and analysis.

- **Experimental repetition and validation**: To ensure the reliability of findings, it is essential to repeat experiments and validate results under varying conditions to confirm their reproducibility.

7.2   Hydrate formation

Similar to salt dry-out, hydrate saturation was found to have a positive correlation with initial water saturation. It was found that hydrates are very sensitive to pressure and temperature changes, both when forming and during dissociation. Hydrate formation was found to be sensitive to pressure pulses, with short pressure pulses shown to be advantageous for hydrate growth. Additionally, a

'sheet-like' hydrate structure was observed, which could not be found in literature. Hydrate dissociation was shown to be very temperature dependent, where a change in temperature of 0.1°C could result in total disappearance of all hydrates.

As with salt dry-out, the hydrate formation phenomena are not yet fully understood. Once again, the recommendations for future work and research in this field are listed below.

- **Impact of water/brine impurities on hydrate formation**: Assess how impurities in water or brine influence the process of hydrate formation, potentially affecting the stability and structure of hydrates.

- **Effect of microfluidic chip thickness on hydrate formation**: Explore the relationship between microfluidic chip thickness and hydrate formation to determine optimal design parameters for microfluidic chips used in experiments.

- **Analysis of 'sheet-like' hydrate structures**: Study the formation and causes of 'sheet-like' structures within hydrates to understand their implications for hydrate behavior and stability.

- **Experimental repetition and validation**: Similar to salt dry-out, hydrate experiments should be repeated and validated, increasing the number of cycles to ensure consistency and reliability of results.

- **Optimization of trigger intervals**: Find the optimal trigger intervals for hydrate formation, enhancing the efficiency and control of experimental setups.

- **Impact of microfluidic chip permeability and patterns**: Investigate how variations in microfluidic chip permeability and patterns affect hydrate formation.

Bibliography

Abbasi, P., Madani, M., Abbasi, S., & Moghadasi, J. (2022, January). Mixed salt precipitation and water evaporation during smart water alternative CO_2 injection in carbonate reservoirs. *Journal of Petroleum Science and Engineering*(208), p. 109258. https://doi.org/https://doi.org/10.1016/j.petrol.2021.109258

Aghajanloo, M., Yan, L., Berg, S., Voskov, D., & Farajzadeh, R. (2024, February 24). Impact of CO_2 hydrates on injectivity during CO_2 storage in depleted gas fields: A literature review. *Gas Science and Engineering, 123*, 205250. https://doi.org/https://doi.org/10.1016/j.jgsce.2024.205250

Alvarado, V., & Manrique, E. (2010). Chapter 2 - Enhanced Oil Recovery Concepts. *Enhanced Oil Recovery - Field Planning and Development Strategies*, pp. 7-16. https://doi.org/https://doi.org/10.1016/B978-1-85617-855-6.00008-5

Arendt, B., Dittmar, D., & Eggers, R. (2004, June 20). Interaction of interfacial convection and mass transfer effects in the system CO_2–water. *International Journal of Heat and Mass Transfer, 47*(17-18), 3649-3657. https://doi.org/https://doi.org/10.1016/j.ijheatmasstransfer.2004.04.011

Bandilla, K. W. (2020). Carbon capture and storage. *Future Energy*, pp. 669-692. https://doi.org/https://doi.org/10.1016/B978-0-08-102886-5.00031-1

Bhattacharjee, G., Kumar, A., Sakpal, T., & Kumar, R. (2015). Carbon dioxide sequestration: influence of porous media on hydrate formation kinetics. *Sustainable Chemistry & Engineering*(3), pp. 1205-1214. https://doi.org/https://doi.org/10.1021/acssuschemeng.5b00171

Centre for Gas Hydrate Research. (2023). *What are Gas Hydrates?* Retrieved October 17, 2023, from https://hydrate.site.hw.ac.uk/what-are-gas-hydrates/

Cerasi, P., Todorovic, J., Raphaug, M., & Grimstad, A.-A. (2021, October 12). *Salt Precipitation Experiments for Improved CO_2 Storage*. Retrieved May 29, 2024, from SINTEF: https://blog.sintef.com/sintefenergy/ccs/salt-precipitation-experiments-for-improved-co2-storage/

Chesnokov, C., Farajzadeh, R., Prempeh, K. O., Kahrobaei, S., Snippe, J., & Bedrikovetsky, P. (2024). Joule-Thomson cooling of CO_2 injected into aquifer under heat exchange with adjacent formations by Newtons law-1D exact solution. *arXiv preprint*. https://doi.org/https://doi.org/10.48550/arXiv.2403.09049

Chong, Z. R., Yang, S. H., Babu, P., Linga, P., & Li, X. S. (2016, January 15). Review of natural gas hydrates as an energy resource: Prospects and challenges. *Applied Energy*(162), pp. 1633-1652. https://doi.org/https://doi.org/10.1016/j.apenergy.2014.12.061

Espinosa-Marzal, R. M. (2010, March 10). Advances in Understanding Damage by Salt Crystallization. *Accounts of chemical research, 43*(6), 897-905. https://doi.org/https://doi.org/10.1021/ar9002224

Espinosa-Marzal, R. M., & Scherer, G. W. (2010, March 10). Advances in Understanding Damage by Salt Crystallization. *Accounts of chemical research, 43*(6), 897-905. https://doi.org/https://doi.org/10.1021/ar9002224

Gambelli, A. M., & Rossi, F. (2021, December 1). Thermodynamic and kinetic characterization of methane hydrate 'nucleation, growth and dissociation processes, according to the labile Cluster theory. *Chemical Engineering Journal*(425). https://doi.org/https://doi.org/10.1016/j.cej.2021.130706

Gauteplass, J., Almenningen, S., Barth, T., & Ersland, G. (2020, September). Hydrate Plugging and Flow Remediation during CO2 Injection in Sediments. *Energies*(13(17)). https://doi.org/http://dx.doi.org/10.3390/en13174511

Gauteplass, J., Almenningen, S., Ersland, G., & Barth, T. (2018, November). Hydrate seal formation during laboratory CO2 injection in a cold aquifer. *International Journal of Greenhouse Gas Control*(78), pp. 21-26. https://doi.org/https://doi.org/10.1016/j.ijggc.2018.07.017

Gauteplass, J., Almenningen, S., Ersland, G., Barth, T., Yang, J., & Chapoy, A. (2020, February 1). Multiscale investigation of CO2 hydrate self-sealing potential for carbon geo-sequestration. *Chemical Engineering Journal*(381). https://doi.org/https://doi.org/10.1016/j.cej.2019.122646

Ghoniem, A. F. (2011, February). Needs, resources and climate change: Clean and efficient conversion technologies. *Progress in energy and combustion science, 1*(37), pp. 15-51. https://doi.org/https://doi.org/10.1016/j.pecs.2010.02.006

Hauge, L. P. (2016, August 16). Pore-level hydrate formation mechanisms using realistic rock structures in high-pressure silicon micromodels. *International Journal of Greenhouse Gas Control, 53*, 178-186. https://doi.org/https://doi.org/10.1016/j.ijggc.2016.06.017

Hauge, L. P., Gauteplass, J., Høyland, M. D., Ersland, G., Kovscek, A., & Fernø, M. A. (2016, August 16). Pore-level hydrate formation mechanisms using realistic rock structures in high-pressure silicon micromodels. *International Journal of Greenhouse Gas Control, 53*, 178-186. https://doi.org/https://doi.org/10.1016/j.ijggc.2016.06.017

Ho, T.-H. M., & Tsai, P. A. (2020, September 14). Microfluidic salt precipitation: implications for geological CO2 storage. *Lab on a Chip, 20*(20), pp. 3806-3814. https://doi.org/https://doi.org/10.1039/D0LC00238K

IPCC — Intergovernmental Panel on Climate Change. (2023, March 20). *Urgent climate action can secure a liveable future for all*. Retrieved September 26, 2023, from IPCC — Intergovernmental Panel on Climate Change: https://www.ipcc.ch/2023/03/20/press-release-ar6-synthesis-report/

Jamekhorshid, A., & Azin, R. (2023). Chapter 10 - Application of life cycle assessment on enhanced oil recovery processes. *Challenges and Recent Advances in Sustainable Oil and Gas Recovery and Transportation*, pp. 227-242. https://doi.org/https://doi.org/10.1016/B978-0-323-99304-3.00013-3

Kim, M. S. (2013, February 27). Aquifer-on-a-Chip: understanding pore-scale salt precipitation dynamics during CO2 sequestration. *Lab on a Chip, 13*, 2508-2518. https://doi.org/https://doi.org/10.1039/C3LC00031A

Kim, M., Sell, A., & Sinton, D. (2013, February 27). Aquifer-on-a-Chip: understanding pore-scale salt precipitation dynamics during CO2 sequestration. *Lab on a Chip, 13*, 2508-2518. https://doi.org/https://doi.org/10.1039/C3LC00031A

Libbrecht, K. G. (2005, April). The physics of snow crystals. *Reports on progress in physics*(68). https://doi.org/http://dx.doi.org/10.1088/0034-4885/68/4/R03

Lyu, X., Khait, M., & Voskov, D. (2021, August 11). Operator-Based Linearization Approach for Modeling of Multiphase Flow with Buoyancy and Capillarity. *SPE Journal*(26), pp. 1858-1875. https://doi.org/https://doi.org/10.2118/205378-PA

Makogon, Y. F. (1997). *Hydrates of hydrocarbons.* Retrieved October 23, 2023, from https://www.osti.gov/biblio/665385

Makwashi, N., Zhao, D., Ismaila, T. A., & Paiko, I. (2018). Pipeline gas hydrate formation and treatment: a review. *Pipeline gas hydrate formation and treatment: a review*, (pp. 2450-2454). Kano. Retrieved from https://www.researchgate.net/profile/Nura-Makwashi/publication/330262173_Pipeline_Gas_Hydrate_Formation_and_Treatment_A_Review/links/5c3643d392851c22a3677854/Pipeline-Gas-Hydrate-Formation-and-Treatment-A-Review.pdf

Masoudi, M. (2021). *Near wellbore processes during carbon capture, utilization, and storage (CCUS): an integrated modeling approach.* University of Oslo, Department of Geosciences. Retrieved from https://www.duo.uio.no/handle/10852/89862

Massah, M., Sun, D., Sharifi, H., & Englezos, P. (2018, February). Demonstration of gas-hydrate assisted carbon dioxide storage through horizontal injection in lab-scale reservoir. *The Journal of Chemical Thermodynamics*(117), pp. 106-112. https://doi.org/https://doi.org/10.1016/j.jct.2017.09.019

Micronit. (n.d.). *Enhanced oil recovery (EOR) chip - topconnect*. Retrieved from https://store.micronit.com/eor_chip.html

Micronit. (n.d.). *Fluidic Connect 4515 chip holder - topconnect*. Retrieved from https://store.micronit.com/fluidic_connect_4515.html

Micronit. (n.d.). *Fluidic Connect Pro chip holder - topconnect*. Retrieved 1 10, 2024, from https://store.micronit.com/fluidic_connect_pro.html

Miri, R., & Hellevang, H. (2016, August). Salt precipitation during CO2 storage—A review. *International Journal of Greenhouse Gas Control*(51), pp. 136-147. https://doi.org/https://doi.org/10.1016/j.ijggc.2016.05.015

Miri, R., van Noort, R., Aagaard, P., & Hellevang, H. (2015, October 24). New insights on the physics of salt precipitation during injection of CO2 into saline aquifers. *International Journal of Greenhouse Gas Control*. https://doi.org/https://doi.org/10.1016/j.ijggc.2015.10.004

Norouzi, A. M., Babaei, M., Han, W. S., Kim, K. Y., & Niasar, V. (2021, June 2). CO2-plume geothermal processes: A parametric study of salt precipitation influenced by capillary-driven backflow. *Chemical Engineering Journal*(425), p. 130031. https://doi.org/https://doi.org/10.1016/j.cej.2021.130031

Ott, H., Roels, S. M., & De Kloe, K. (2015, December). Salt precipitation due to supercritical gas injection: I. Capillary-driven flow in unimodal sandstone. *International Journal of Greenhouse Gas Control*(43), pp. 247-255. https://doi.org/https://doi.org/10.1016/j.ijggc.2015.01.005

Ren, X., Guo, Z., Ning, F., & Ma, S. (2020, February 10). Permeability of hydrate-bearing sediments. *Earth-science reviews*(202), p. 103100. https://doi.org/https://doi.org/10.1016/j.earscirev.2020.103100

Riahi, K., Rubin, E. S., Taylor, M. R., Schrattenholzer, L., & Hounshell, D. (2004, July). Technological learning for carbon capture and sequestration technologies. *Energy economics, 4*(26), pp. 539-564. https://doi.org/https://doi.org/10.1016/j.eneco.2004.04.024

Schneider, C., Rasband, W., & Eliceiri, K. (2012, June 28). NIH Image to ImageJ: 25 years of image analysis. *Nature Methods*(9), pp. 671-675. https://doi.org/https://www.nature.com/articles/nmeth.2089#citeas

Sokama-Neuyam, Y. A., Boakye, P., Aggrey, W. N., Obeng, N. O., Adu-Boahene, F., Woo, S. H., & Ursin, J. R. (2020, June 14). Theoretical Modeling of the Impact of Salt Precipitation on CO2 Storage Potential in Fractured Saline Reservoirs. *ACS omega, 5*(24), pp. 14776–14785. https://doi.org/https://doi.org/10.1021/acsomega.0c01687

Sun, Q., & Kang, Y. T. (2016, September). Review on CO2 hydrate formation/dissociation and its cold energy application. *Renewable and Sustainable Energy Reviews*(62), pp. 478-494. https://doi.org/https://doi.org/10.1016/j.rser.2016.04.062

Suranovic, S. (2013, June). Fossil fuel addiction and the implications for climate change policy. *Global Environmental Change, 3*(23), pp. 598-608. https://doi.org/https://doi.org/10.1016/j.gloenvcha.2013.02.006

Tang, Y., Yang, R., & Kang, X. (2018, December 14). Modeling the effect of water vaporization and salt precipitation on reservoir properties due to carbon dioxide sequestration in a depleted gas reservoir. *Petroleum, 4*, pp. 385-397. https://doi.org/https://doi.org/10.1016/j.petlm.2017.12.003

The Engineering ToolBox. (2024). *Gases - Dynamic Viscosities*. Retrieved June 1, 2024, from The Engineering ToolBox: https://www.engineeringtoolbox.com/gases-absolute-dynamic-viscosity-d_1888.html

van der Vleuten, R., Farazjadeh, R., Voskov, D., V., N., & Plug, W. (2022, August 29). Impact of Reservoir Heterogeneity on Dry-out Effect during CO2 Injection.

Vysniauskas, A., & Bishnoi, P. R. (1982, September 22). A kinetic study of methane hydrate formation. *Chemical Engineering Science, 38*(7), pp. 1061-1972. https://doi.org/https://doi.org/10.1016/0009-2509(83)80027-X

Xie, N., Liu, Z., Yang, S., & Tan, C. (2020). Energy Efficiency Analysis of Postcombustion Hydrate-Based CO2 Capture with Tetrahydrofuran and Tetra-n-butylammonium Bromide. *Industrial & Engineering Chemistry Research, 2*(59), pp. 802-813. https://doi.org/https://doi.org/10.1021/acs.iecr.9b04744

Xu, J., Bu, Z., Li, H., Li, S., & Sun, B. (2021, December 13). Pore-scale flow simulation on the permeability in hydrate-bearing sediments. *Fuel*(312), p. 122681. https://doi.org/https://doi.org/10.1016/j.fuel.2021.122681

Yan, L., Niftaliyev, R., Voskov, D., & Farajzadeh, R. (2024). Dynamics of salt precipitation at pore scale during CO2 subsurface storage in saline aquifer.

Yan, L., van der Vleuten, R., Najjarihagh, S., Aghajanloo, M., Schellart, M., Voskov, D., & Farajzadeh, R. (2024). Exploring Reservoir Heterogeneity Effects: Insights From Experimental Study On CO2 Injection And Dry-Out Phenomenon.

Yang, L., Xu, M., Yang, Y., Fan, J., & Zhang, X. (2019, December 1). Comparison of subsidy schemes for carbon capture utilization and storage (CCUS) investment based on real option approach: Evidence from China. *Applied Energy*(255). https://doi.org/https://doi.org/10.1016/j.apenergy.2019.113828

Yang, S. H., Babu, P., Chua, S. F., & Linga, P. (2016, January 15). Carbon dioxide hydrate kinetics in porous media with and without salts. *Applied Energy*(162), pp. 1131-1140. https://doi.org/https://doi.org/10.1016/j.apenergy.2014.11.052

Appendices

A   Salt dry-out

A.1   Images of the microfluidic chips used for salt dry-out experiments clean
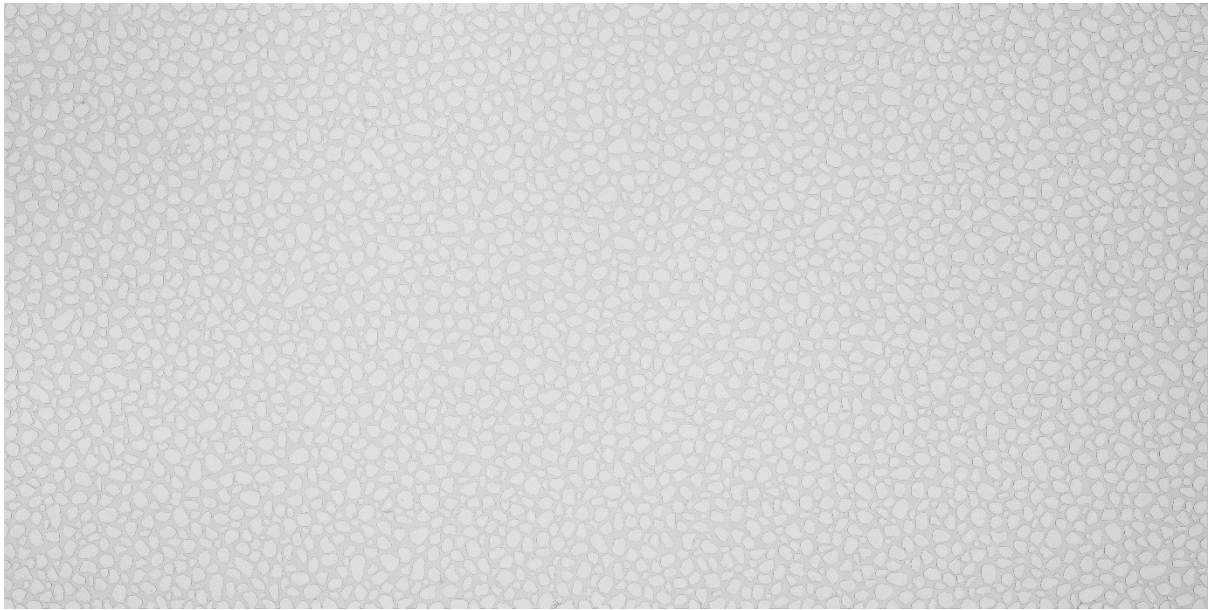
Appendix Figure A-1 Small pore size microfluidic chip clean
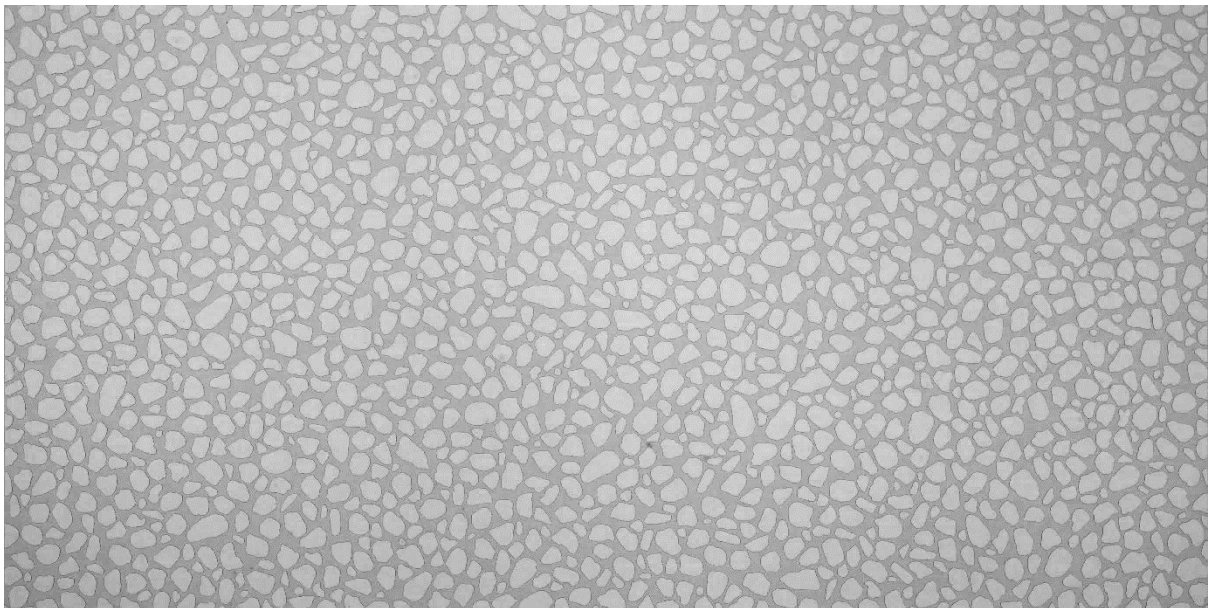
Appendix Figure A-2 Medium pore size microfluidic chip clean
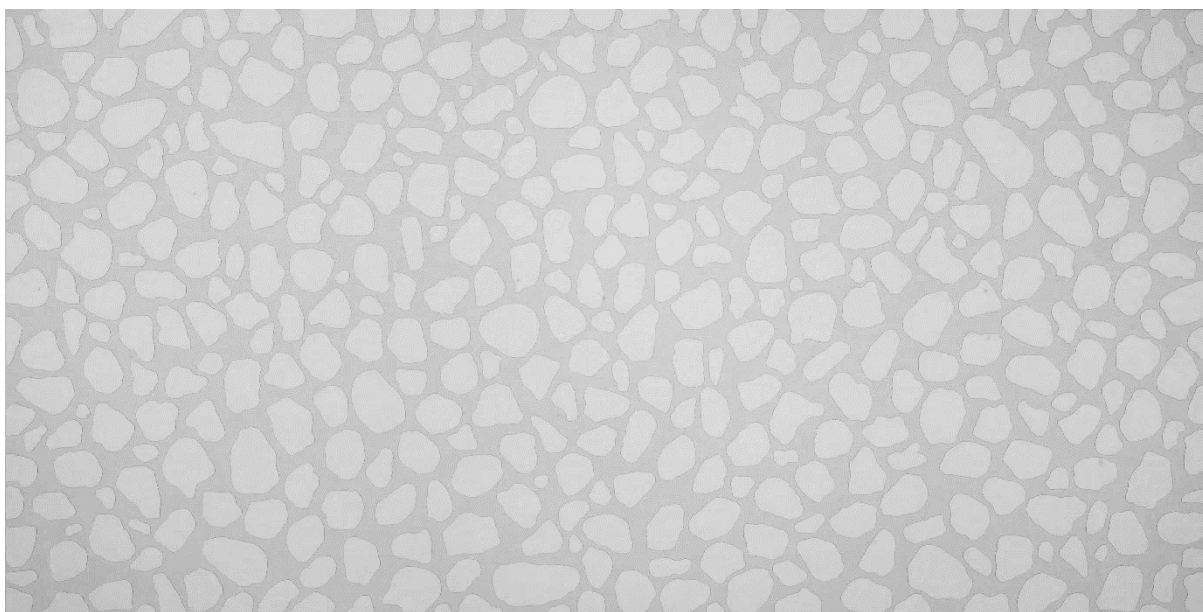
Appendix Figure A-3 Large pore size microfluidic chip clean
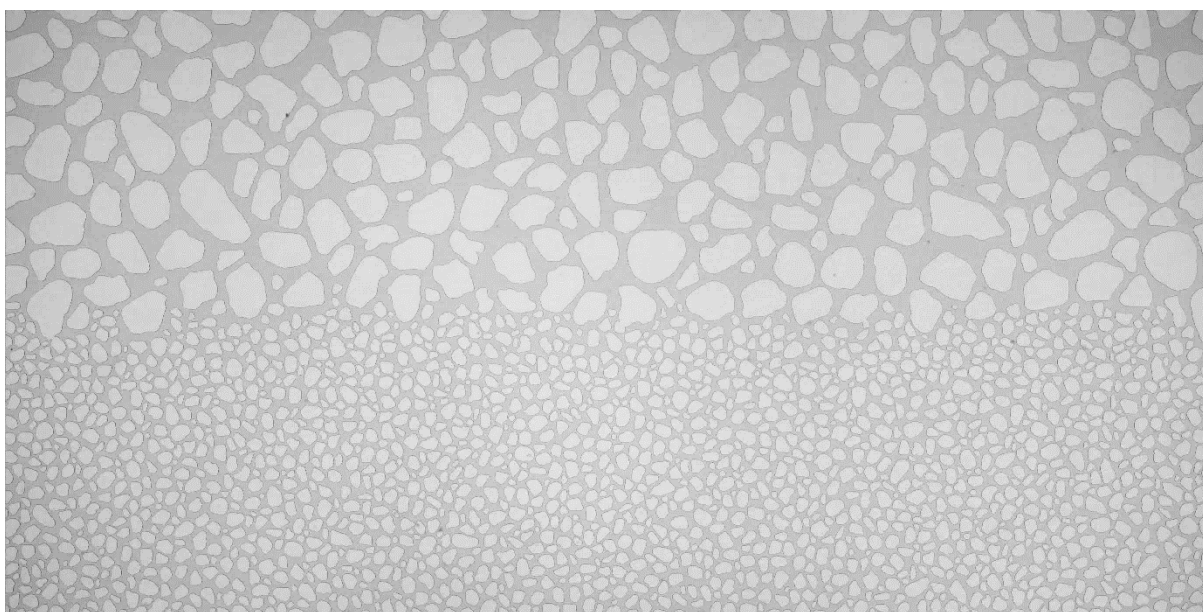
Appendix Figure A-4 Large-small pore size microfluidic chip clean
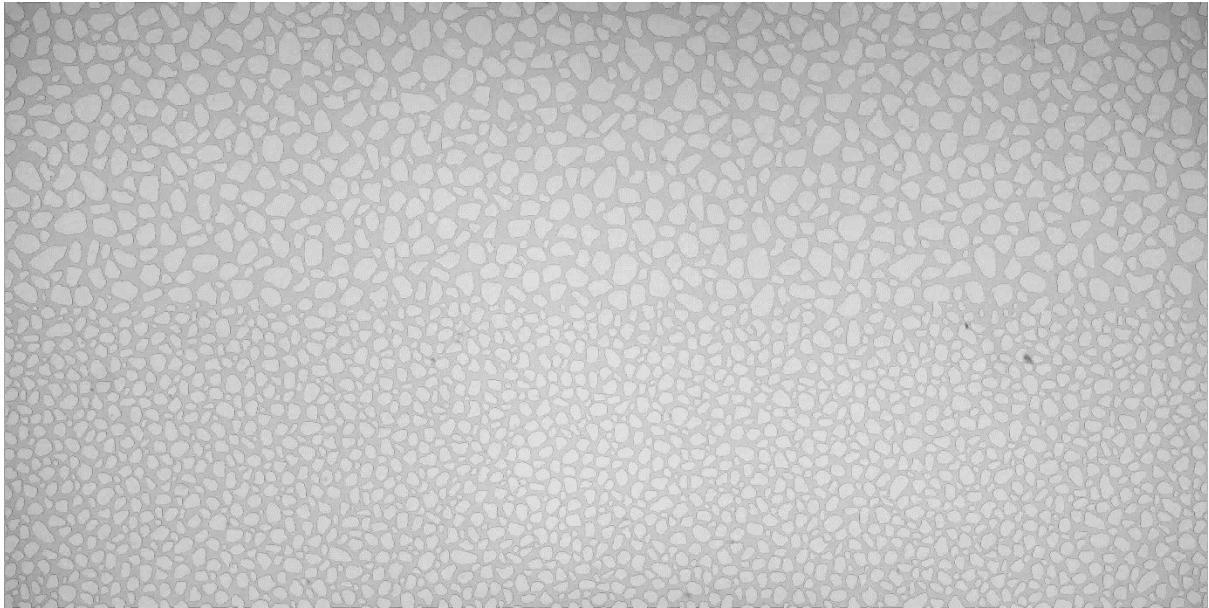
Appendix Figure A-5 Medium-small pore size microfluidic chip clean

A.2 Images of microfluidic chips for salt dry-out experiments after complete drying
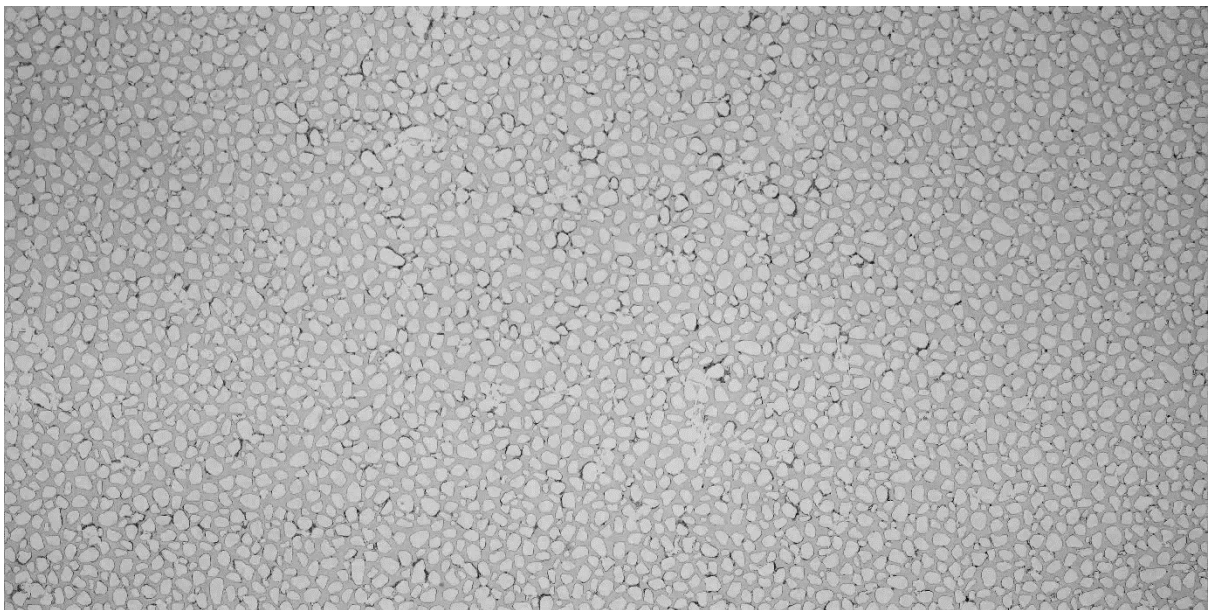
Appendix Figure A-6 Small pore size microfluidic chip after complete drying
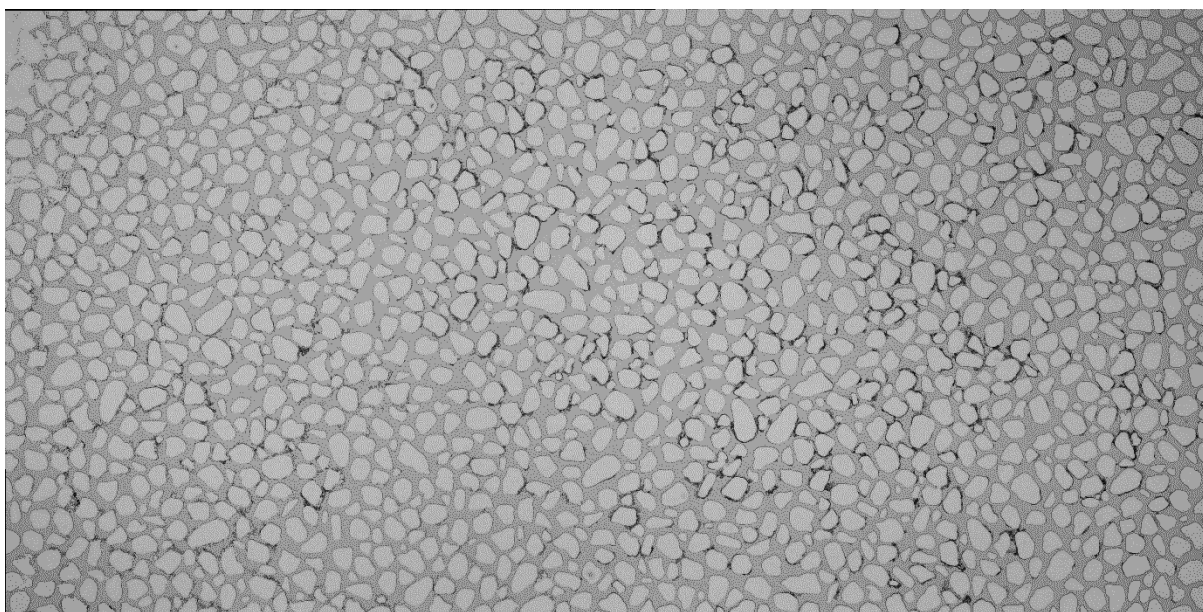
Appendix Figure A-7 Medium pore size microfluidic chip after complete drying
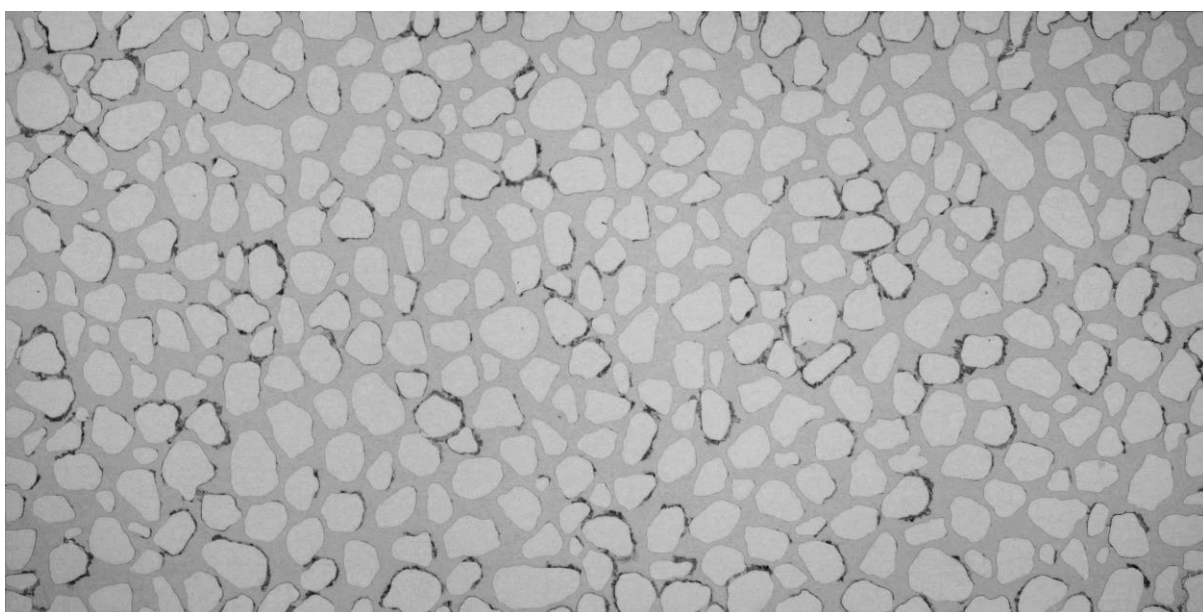
Appendix Figure A-8 Large pore size microfluidic chip after complete drying
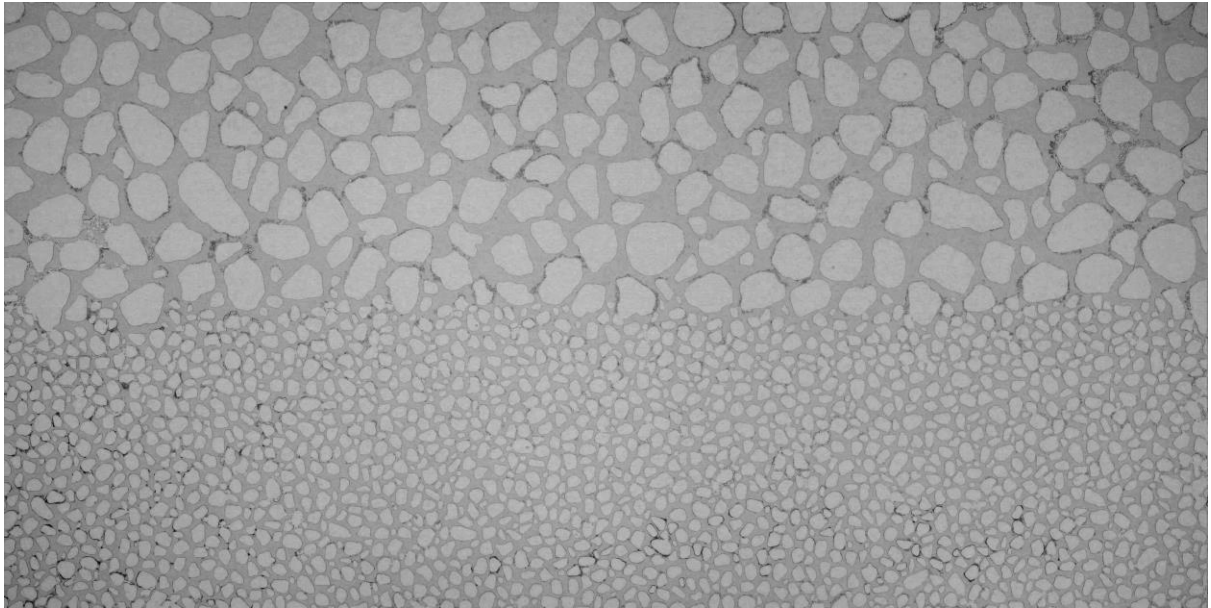
Appendix Figure A-9 Large-small pore size microfluidic chip after complete drying
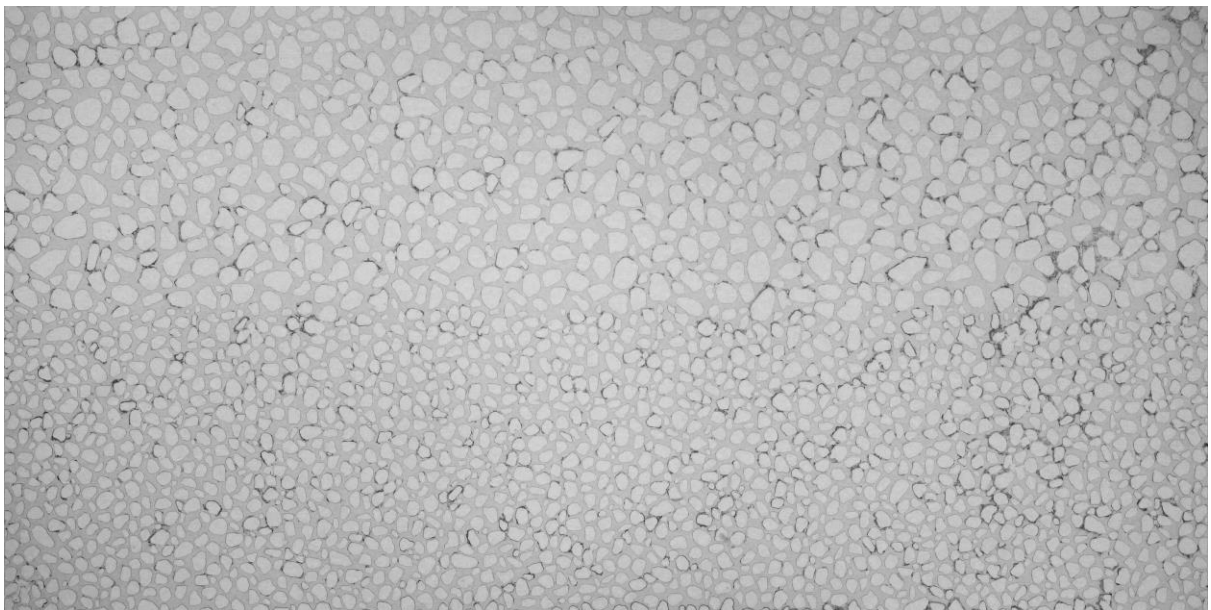
Appendix Figure A-10 Medium-small pore size microfluidic chip after complete drying

Appendix Figure A-11 Pore size distribution for the small microfluidic chip. Average size = 95.16 μm
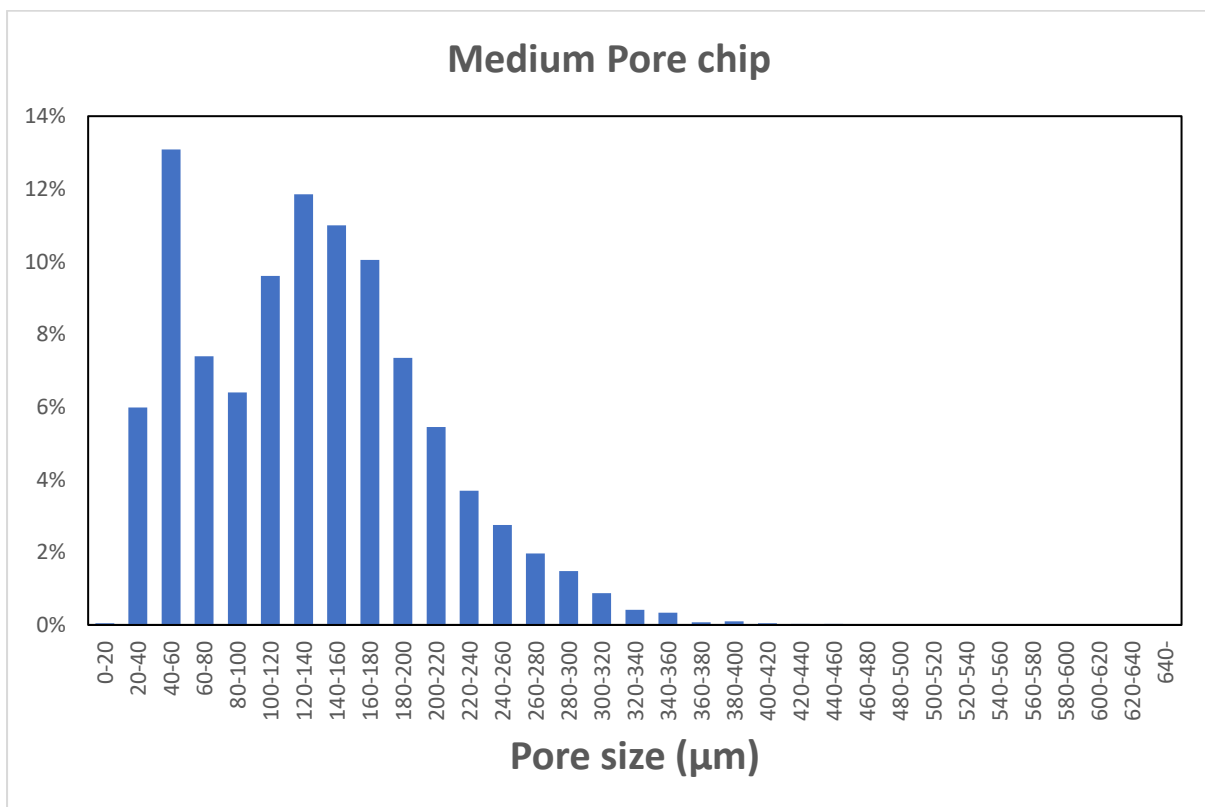
Appendix Figure A-12 Pore size distribution for the medium microfluidic chip. Average size = 135.65 μm
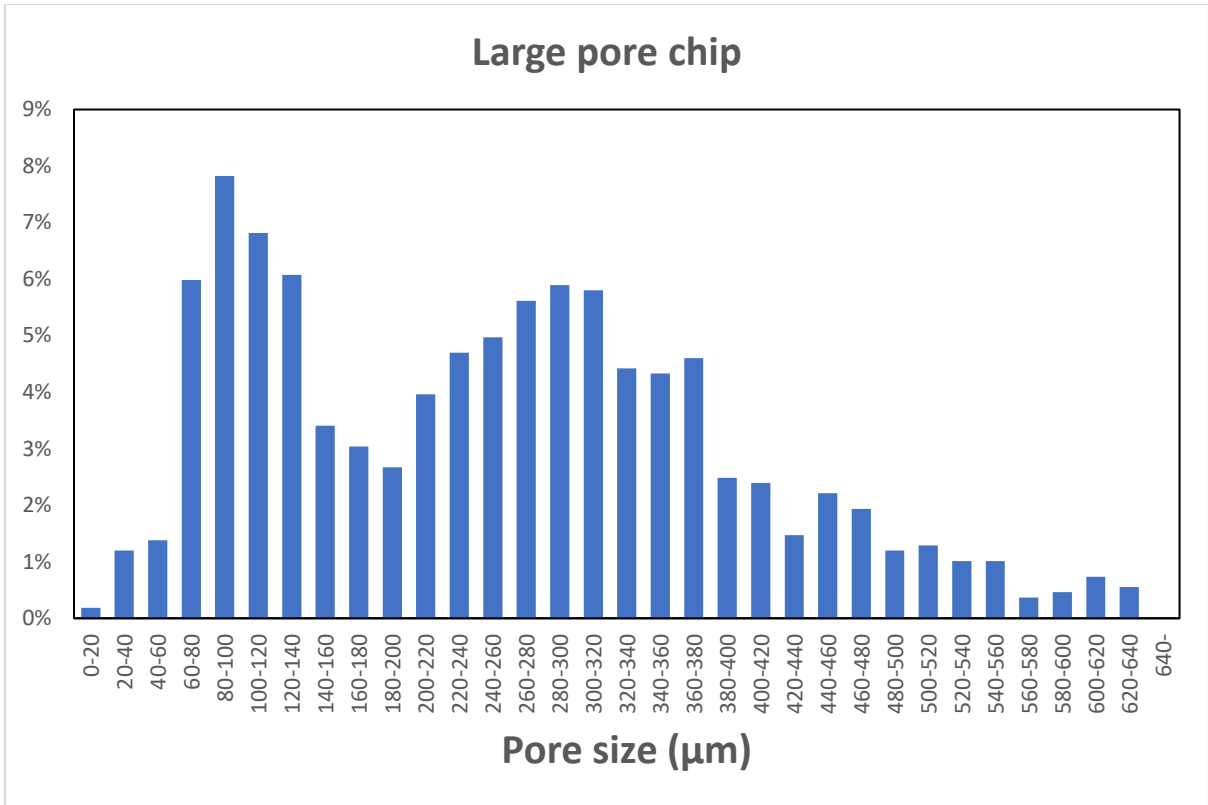
Appendix Figure A-13 Pore size distribution for the large microfluidic chip. Average size = 255.64 μm
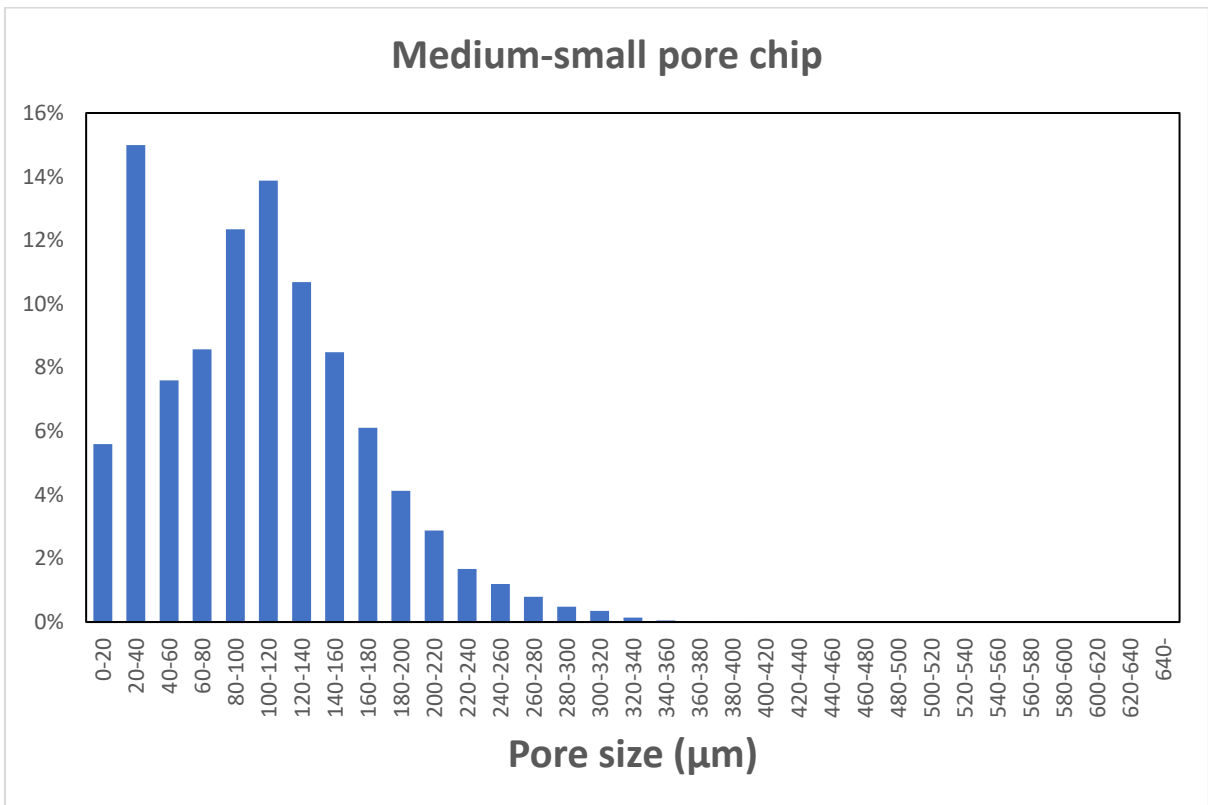
Appendix Figure A-14 Pore size distribution for the medium-small microfluidic chip. Average size = 104.52 μm
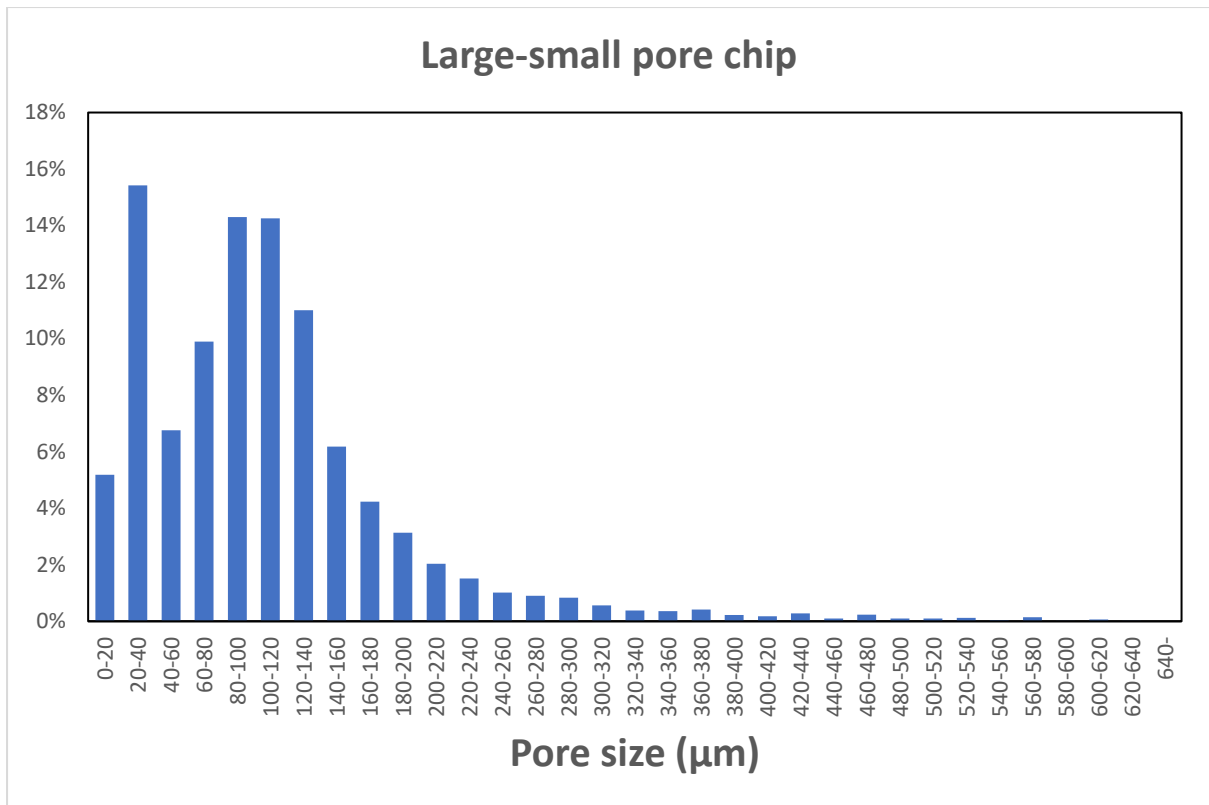
Appendix Figure A-15 Pore size distribution for the large-small microfluidic chip. Average size = 109.83 μm

A.4 Pressure curves from salt dry-out experiments
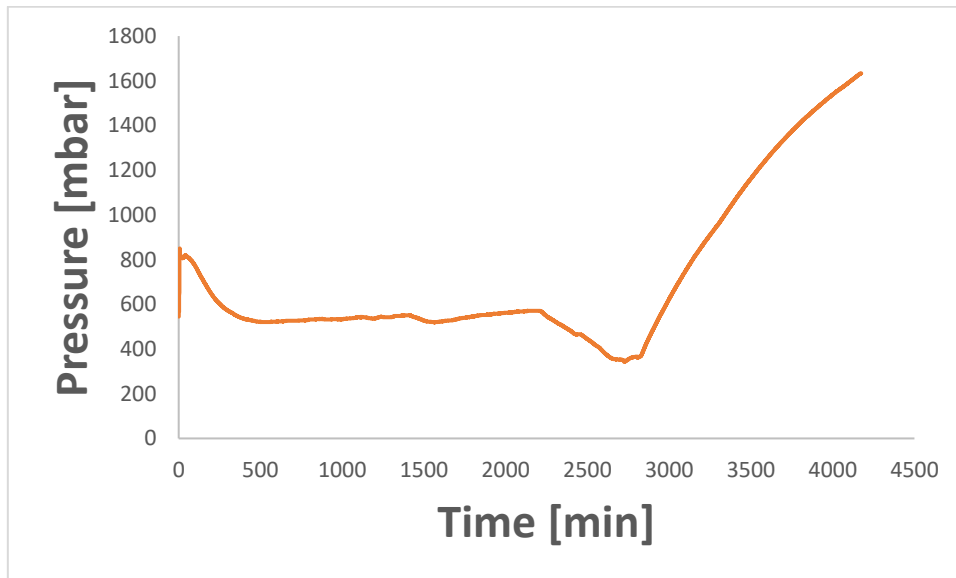
Appendix Figure A-16 Pressure curve of first small microfluidic chip experiment
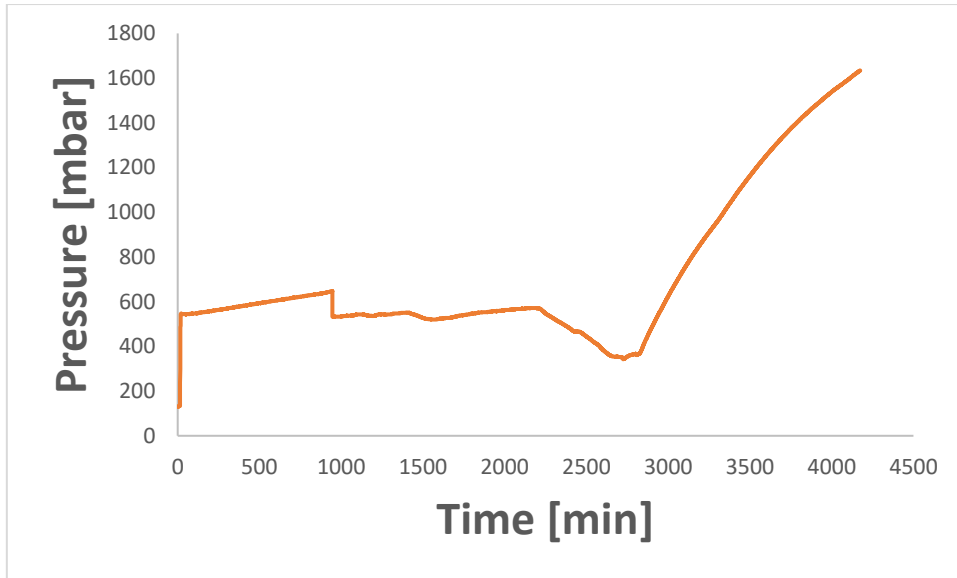
Appendix Figure A-17 Pressure curve of second small microfluidic chip experiment
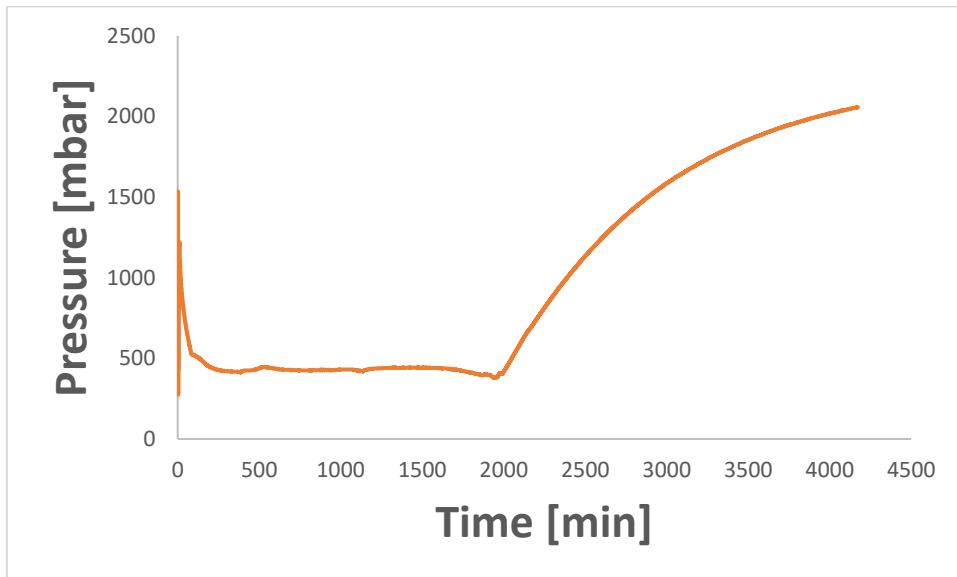
Appendix Figure A-18 Pressure curve of first medium microfluidic chip experiment
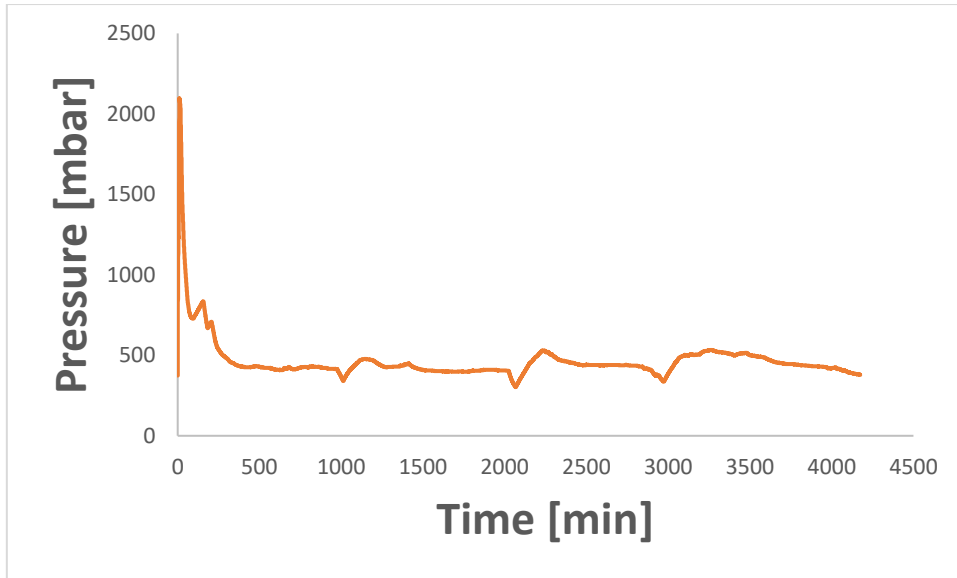
Appendix Figure A-19 Pressure curve of second medium microfluidic chip experiment
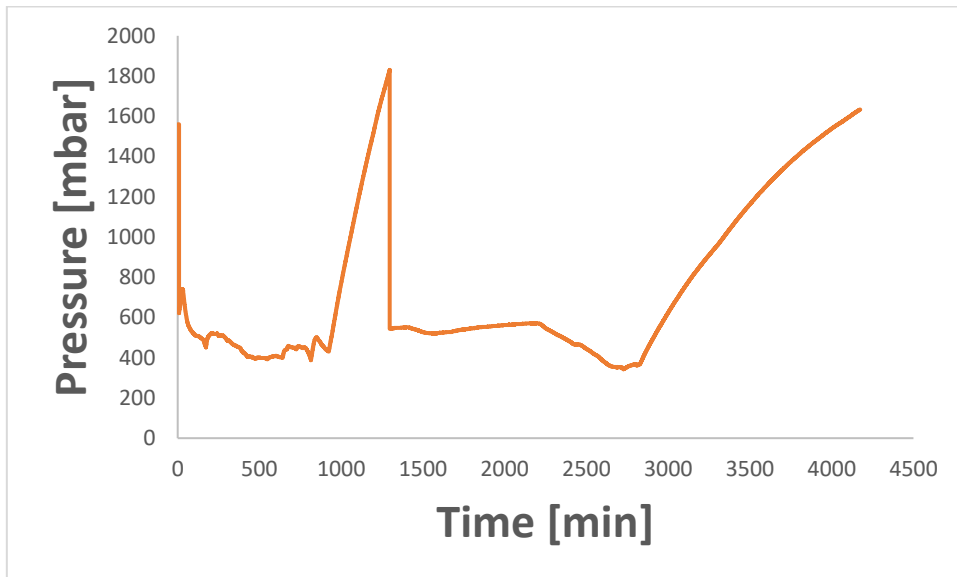
Appendix Figure A-20 Pressure curve of first large microfluidic chip experiment
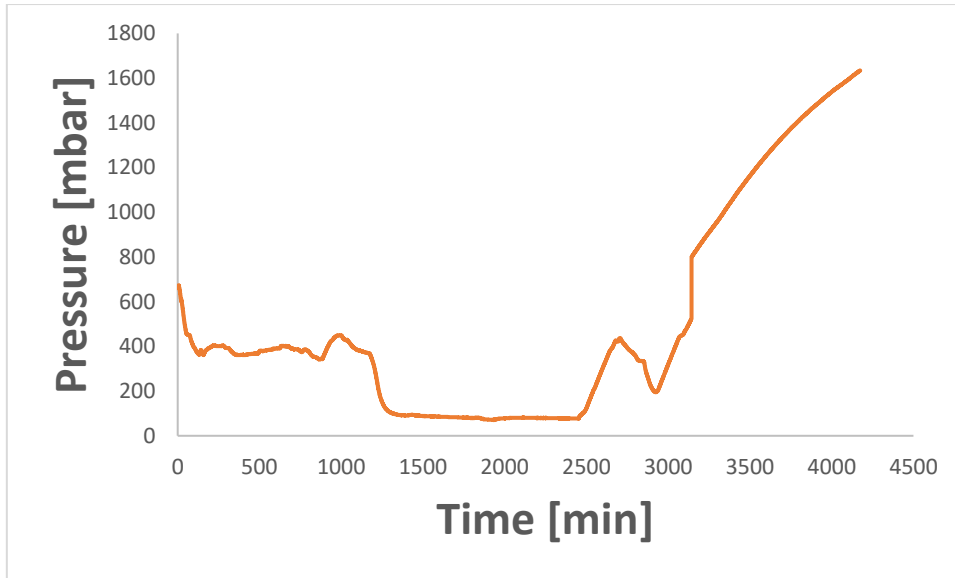
Appendix Figure A-21 Pressure curve of second large microfluidic chip experiment
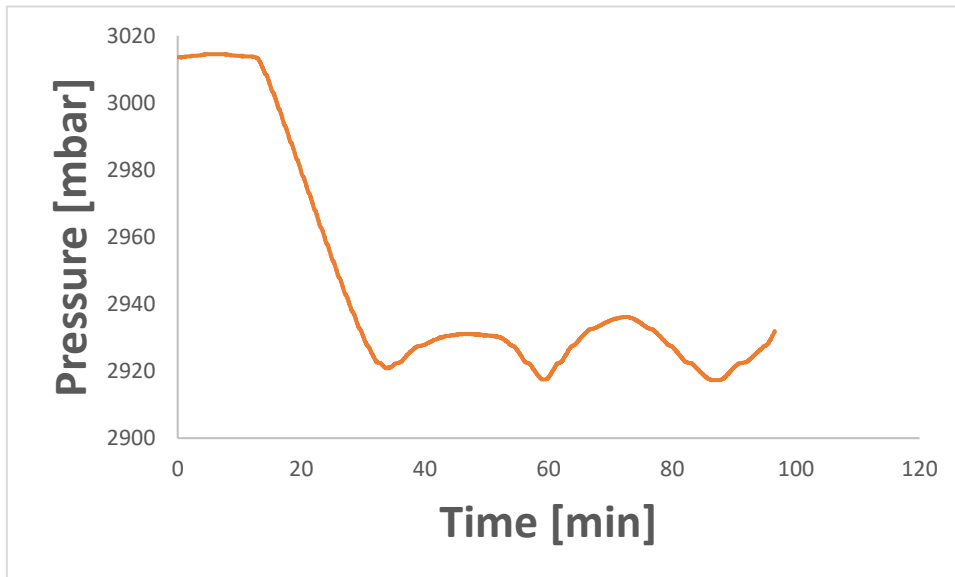
Appendix Figure A-22 Pressure curve of first medium-small microfluidic chip experiment
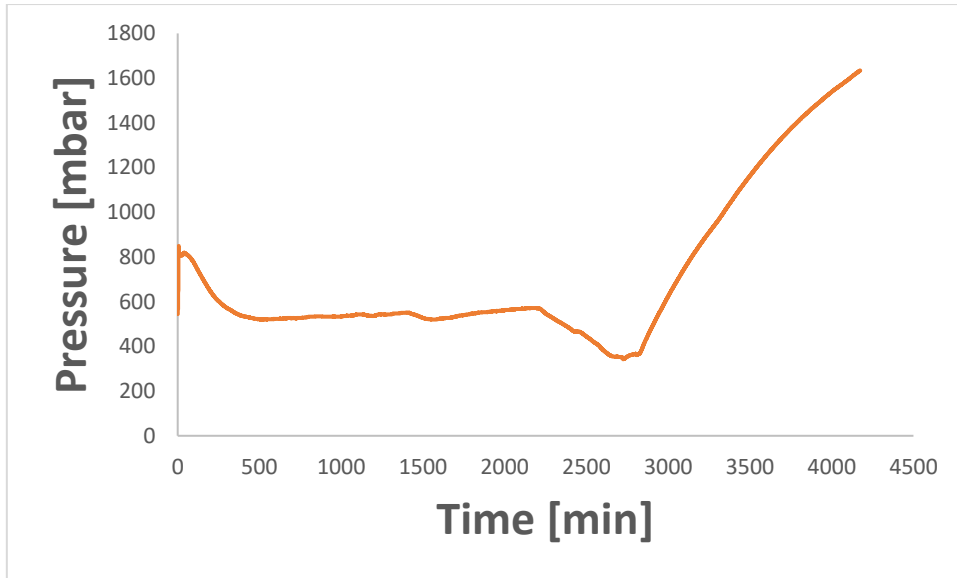
Appendix Figure A-23 Pressure curve of second medium-small microfluidic chip experiment
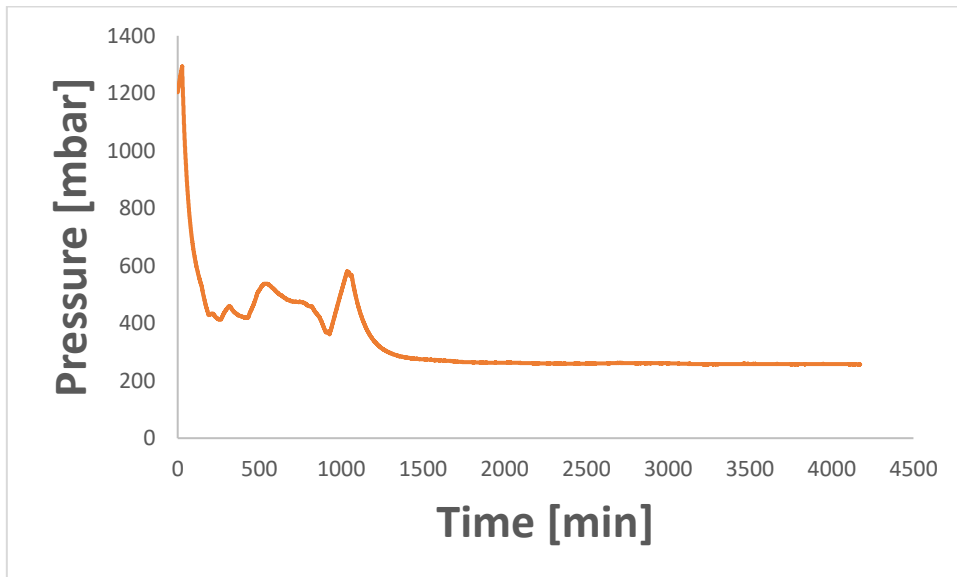
Appendix Figure A-24 Pressure curve of first large-small microfluidic chip experiment
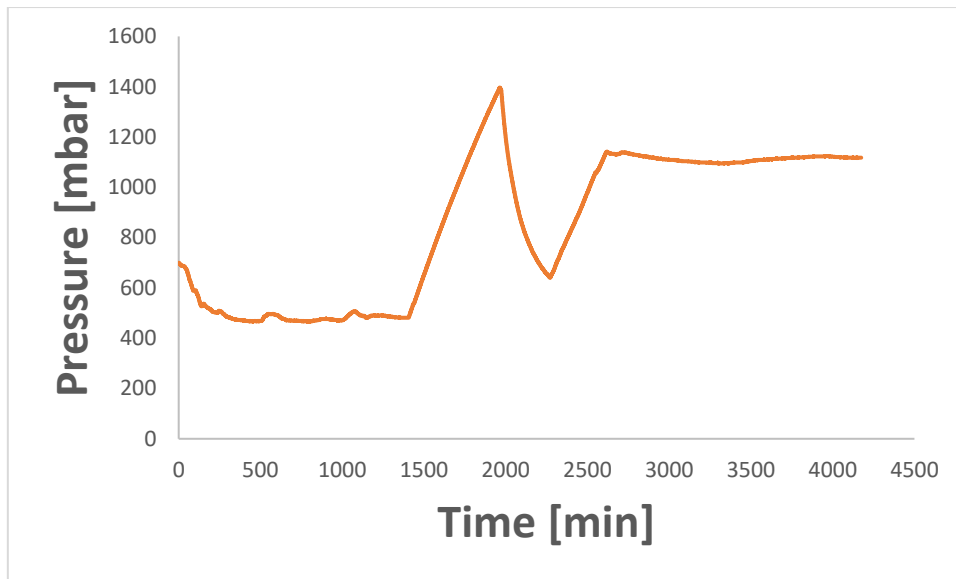
Appendix Figure A-25 Pressure curve of second large-small microfluidic chip experiment

B   Hydrates

B.1   Image of physical rock network EOR microfluidic chip clean
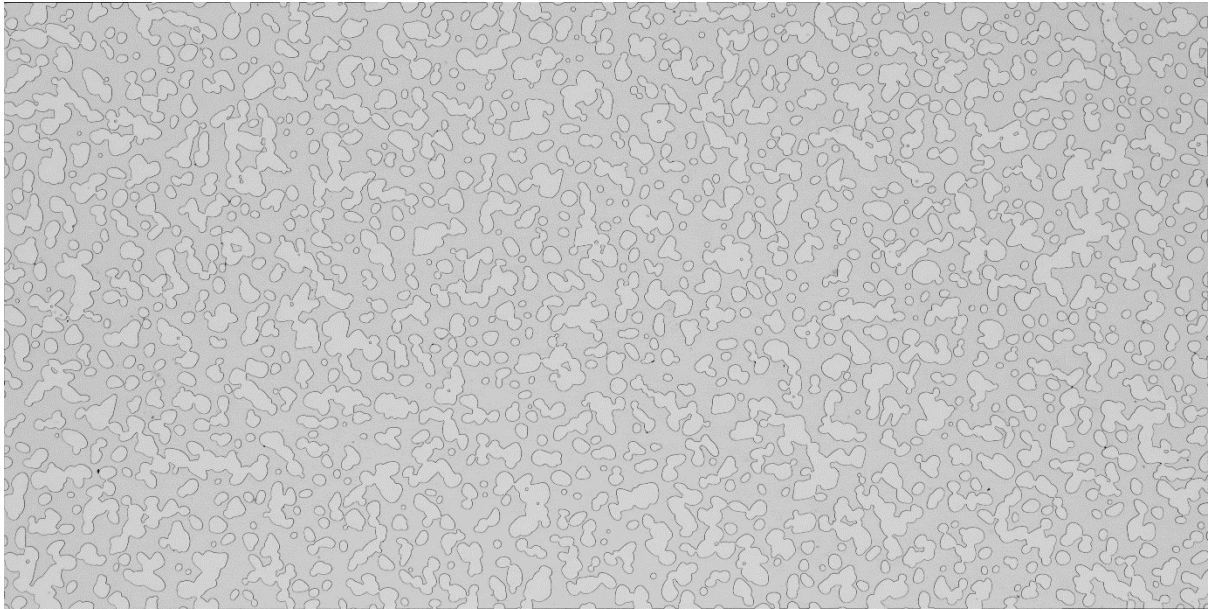
Appendix Figure B-1 Physical rock network EOR microfluidic chip

B.2   Image of physical rock network EOR microfluidic chip in use
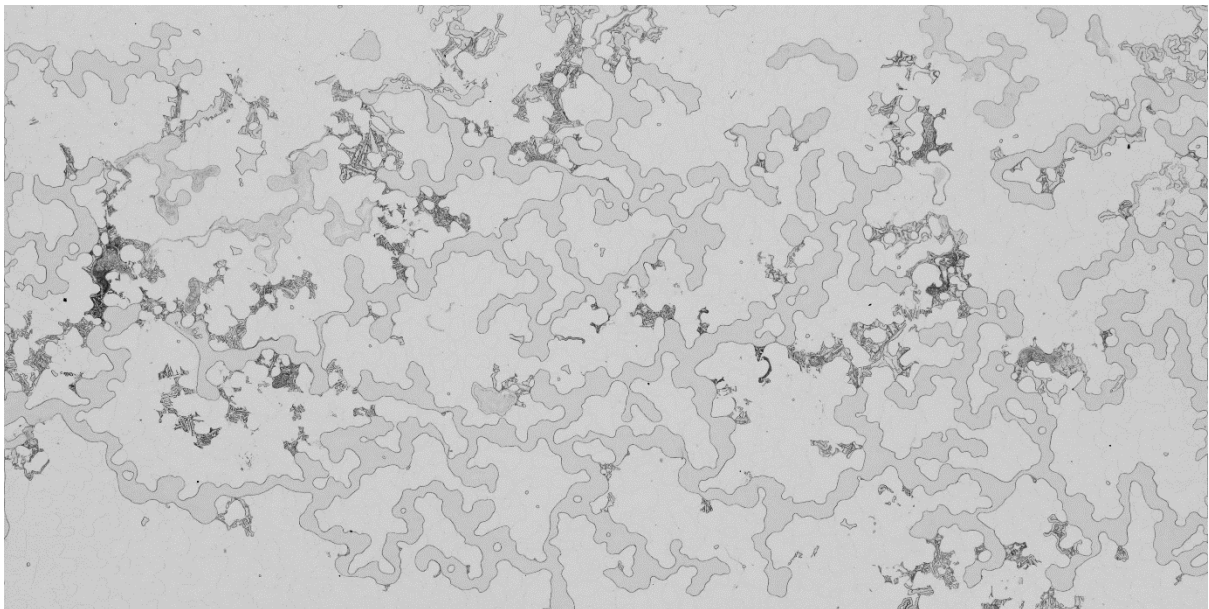
Appendix Figure B-2 Image of how the hydrates are visible in the Physical Rock Network EOR microfluidic chip
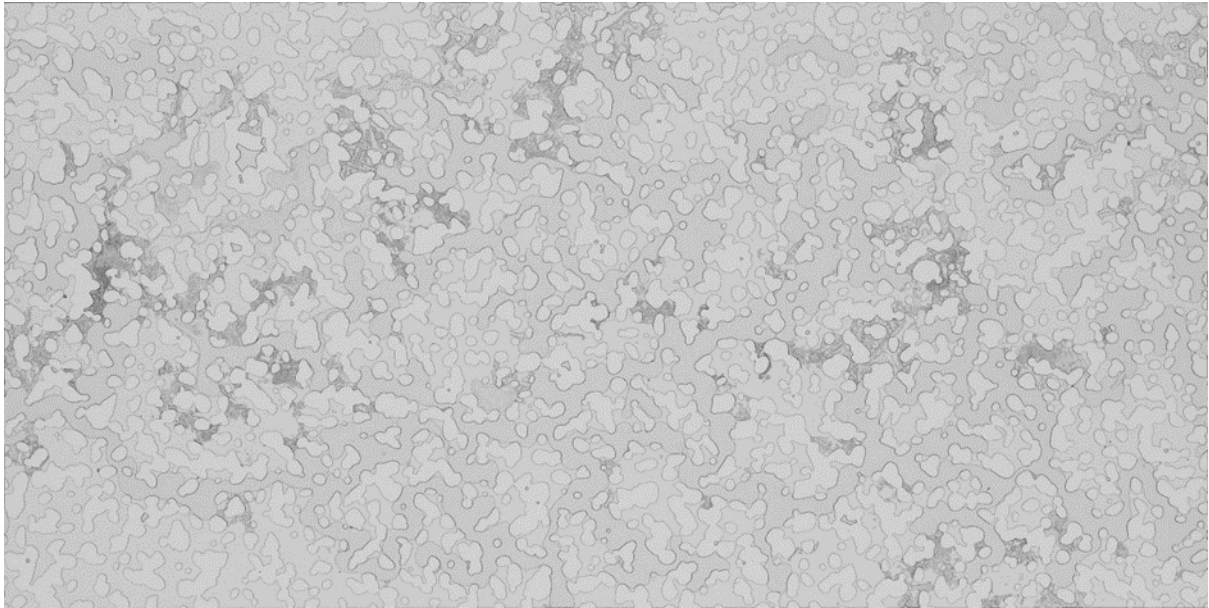
Figure 0-1 Image of how the hydrates are visible in the Physical Rock Network EOR microfluidic chip with grains overlay
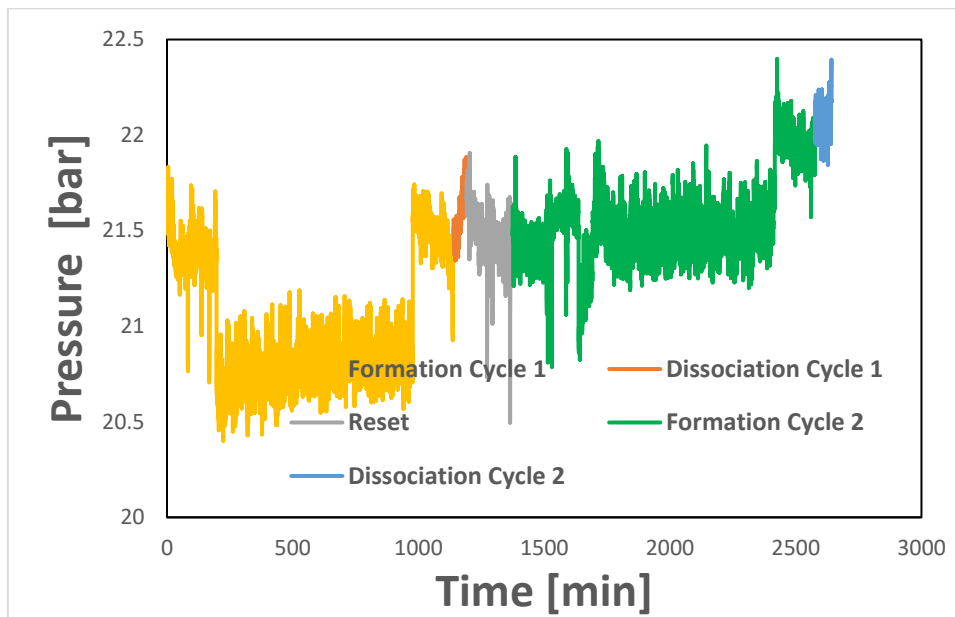
Appendix Figure B-3 Pressure curve from first experiment with manually controlled pressure
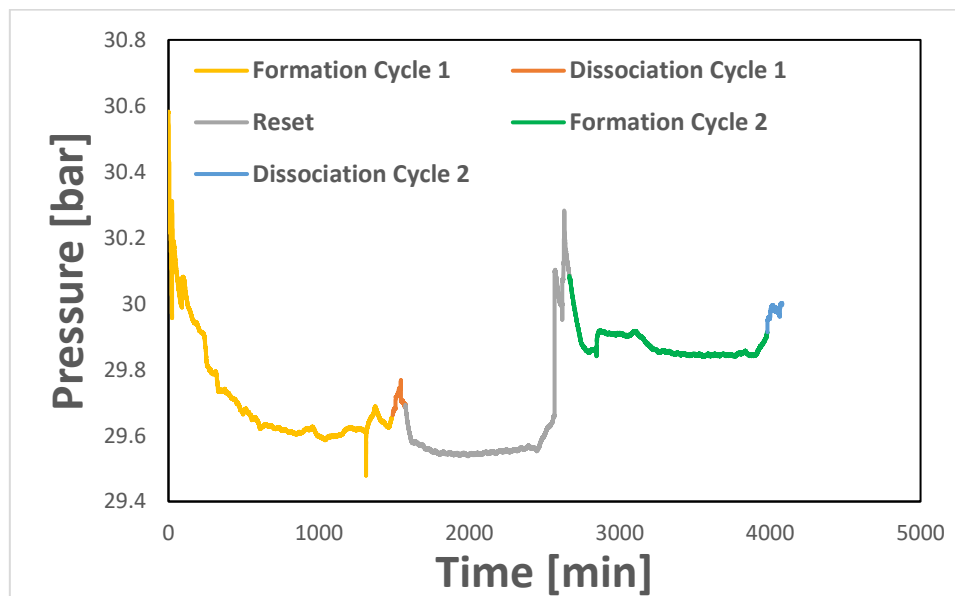
Appendix Figure B-4 Pressure curve from second experiment with trigger mode of 0.5 seconds
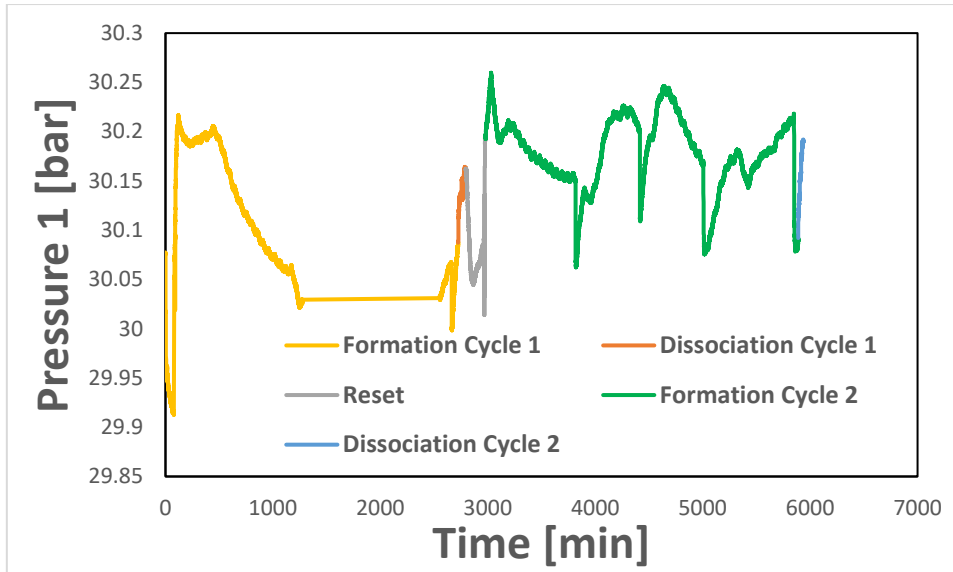
Appendix Figure B-5 Pressure curve from third experiment with trigger mode of 0.2 seconds

C   Steps Image processing

The following steps are undertaken for image processing:

1. Import the images into ImageJ. Due to a limit in RAM, choose a stepsize that results in a total stack of 150-200 images. (Menu path: File › Import › Image Sequence)
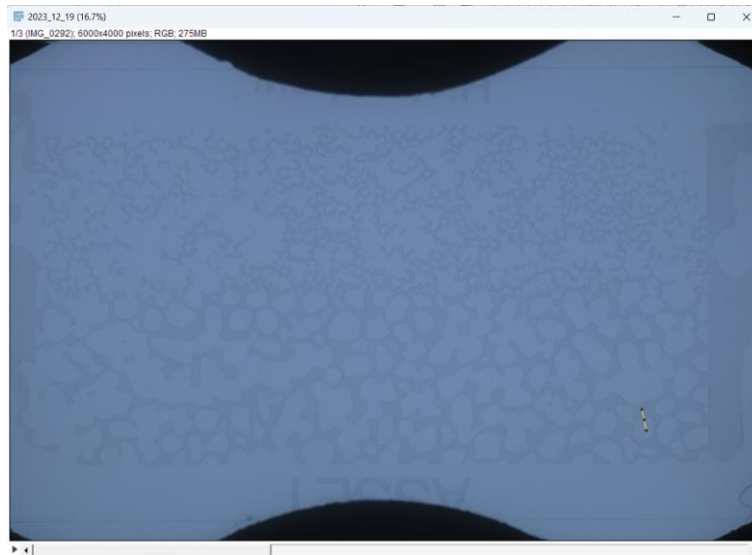
Appendix Figure C-1 The raw image after loading

2. If importing several folders of images, use the *concatenate* function to merge all stacks into one. (Menu path: Image › Stacks › Tools › Concatenate).

3. Align the images using the Scale Invariant Feature Transform (SIFT) algorithm to account for any movement of the camera/microfluidic chip, such as those caused by temperature shifts. (Menu path: Plugins › Registration › Linear Stack Alignment with SIFT).

Appendix Figure C-2 Screenshot of ImageJ, showing the stack after alignment

4. Rotate the image so that the chip is perfectly straight. This can be achieved by drawing a line on a border and measuring the angle. Then use the Rotate tool (Menu path: Image › Transform › Rotate).
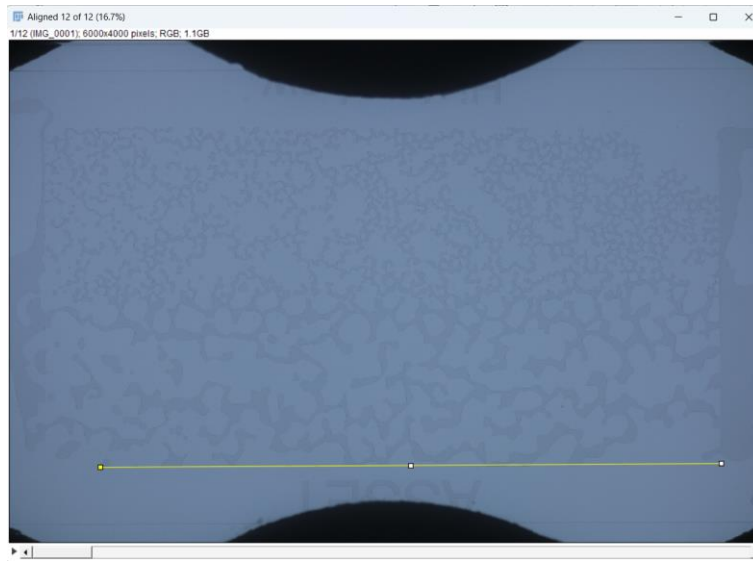
Appendix Figure C-3 Screenshot of ImageJ, showing the line used for stack rotation

5. Load the saturation photo and crop both the saturation photo and the stack to the same dimensions. Select only the pore part of the chip. The dimensions can be copied by pressing SHIFT-E.
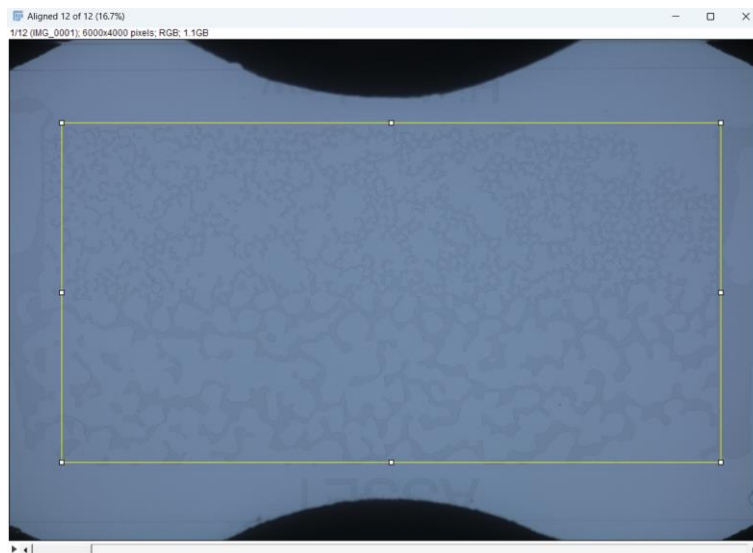
Appendix Figure C-4 Screenshot of ImageJ, showing the cropping of the pore part of the chip

6. Subtract the saturation photo from the experimental photos, resulting in the grains being 'deleted'. Subtract is a function of the image calculator (Menu path: Process › Image Calculator).
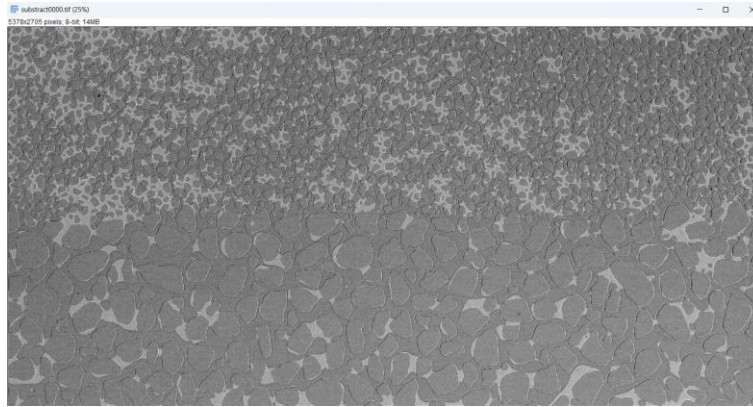
Appendix Figure C-5 Screenshot of ImageJ, showing the result after cropping and substraction

7. Apply a threshold to turn the photos into binary images. This is done twice: once for the salt/hydrates and once for the water saturation. (Menu path: Image › Adjust › Threshold).
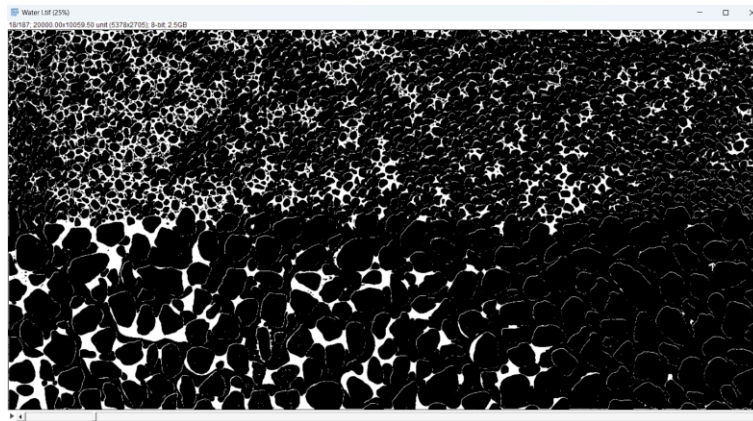
Appendix Figure C-6 Screenshot of ImageJ, showing the image after a threshold has been set

8. The initial threshold is rarely perfect and noise remains. Therefore, create substacks from the stacks, de-noise them, and then recombine them. This function can be found under remove outliers. (Menu path: Process › Noise › Remove Outliers)
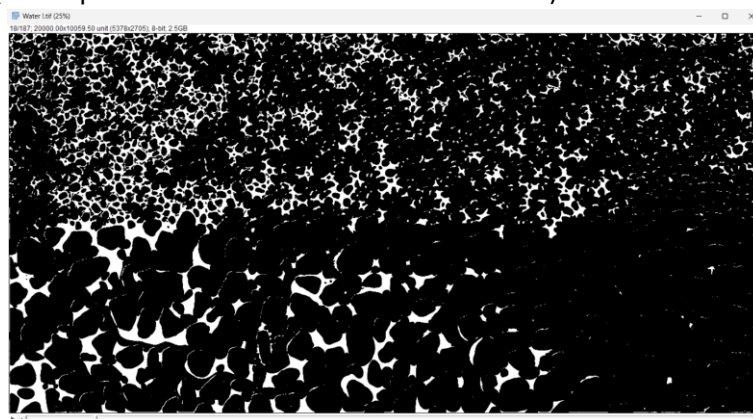
Appendix Figure C-7 Screenshot of ImageJ, showing the final image after de-noising

9. If the overall threshold is satisfactory, scale the stack to the dimensions of the microfluidic chip. (Menu path: Analyze › Set Scale)

10. Analyze the particles using the "analyze particles" function, which provides the area values of the water or the salt/hydrates in each image, necessary for creating graphs in Excel. (Menu path: Analyze › Analyze Particles)

D   Capillary number calculation

Appendix Table D-1 Capillary number calculation for all 10 salt dry-out experiments, showing validity for all

Parameter	Unit	SALT DRY-OUT									
Chip Name		Small	Small	Medium	Medium	Large	Large	Large-Small	Large-Small	Medium-Small	Medium-Small
w	m	9.52E-05	9.52E-05	1.36E-04	1.36E-04	2.56E-04	2.56E-04	1.10E-04	1.10E-04	1.05E-04	1.05E-04
L	m	2.00E-02	2.00E-02	2.00E-02	2.00E-02	2.00E-02	2.00E-02	2.00E-02	2.00E-02	2.00E-02	2.00E-02
h	m	5.00E-06	5.00E-06	5.00E-06	5.00E-06	5.00E-06	5.00E-06	5.00E-06	5.00E-06	5.00E-06	5.00E-06
μ	Pa s	1.61E-05	1.61E-05	1.61E-05	1.61E-05	1.61E-05	1.61E-05	1.61E-05	1.61E-05	1.61E-05	1.61E-05
θ	°	40	40	40	40	40	40	40	40	40	40
γ	Nm	0.068	0.068	0.068	0.068	0.068	0.068	0.068	0.068	0.068	0.068
q	m/s	0.00438	0.00078	0.00665	0.00205	0.00164	0.00051	0.00193	0.00103	0.00279	0.00086
N_c	-	1.54E-07	2.75E-08	2.38E-07	7.33E-08	5.97E-08	1.86E-08	6.85E-08	3.65E-08	9.88E-08	3.04E-08
Valid (<E-5)		Yes	Yes	Yes	Yes	Yes	Yes	Yes	Yes	Yes	Yes

Appendix Table D-2 Capillary number calculation for all 6 hydrate experiments, showing validity for all

Parameter	Unit	HYDRATE					
w	m	3.00E-04	3.00E-04	3.00E-04	3.00E-04	3.00E-04	3.00E-04
L	m	2.00E-02	2.00E-02	2.00E-02	2.00E-02	2.00E-02	2.00E-02
h	m	5.00E-06	5.00E-06	5.00E-06	5.00E-06	5.00E-06	5.00E-06
μ	Pa s	1.61E-05	1.61E-05	1.61E-05	1.61E-05	1.61E-05	1.61E-05
θ	°	40	40	40	40	40	40
γ	Nm	0.068	0.068	0.068	0.068	0.068	0.068
q	m/s	0.000237	0.000237	0.00037	0.00037	0.00022	0.00022
N_c	-	8.65E-09	8.65E-09	1.33E-08	1.33E-08	7.92E-09	7.92E-09
Valid (<E-5)		Yes	Yes	Yes	Yes	Yes	Yes

E   Experimental overview

Appendix Table E-1 Overview of all salt dry-out experiments and obtained results

Experiment	Flowrate mm/s	Hours till dry-out	Longest lasting water location	Highest salt concentration location	Max. water	Max. salt	Max. water large/medium	Max. salt large/medium	Max. water small	Max. salt small	Water backflow	Bigger than initial value	Initial max. water value
Small 1	4.38	54	outlet	inlet	74%	7%					no		
Small 2	0.78	45	middle	outlet	49%	4%					no		
Medium 1	6.65	89	outlet	inlet	40%	10%					yes	yes	29%
Medium 2	2.05	76	outlet	inlet	36%	10%					no		
Large 1	1.64	12	outlet	outlet	42%	11%					yes	no	
Large 2	0.51	13	outlet	inlet	38%	9%					yes	yes	32%
Large-Small 1	1.93	35	outlet	Inlet	94%	12%	42%	5%	53%	7%	yes	yes	40%
Large-Small 2	1.03	133	outlet	Inlet	53%	9%	22%	3%	33%	6%	yes	no	
Medium-Small 1	2.79	29	outlet	middle	37%	8%	21%	3%	16%	5%	no		
Medium-Small 2	0.86	20	outlet	outlet	31%	8%	19%	3%	13%	5%	no		

Appendix Table E-2 Overview of all hydrate experiments with obtained results

Experiment	Cycle	Flowrate [mm/s]	Max. water	Max. Hydrate	Conversion factor	Dissociation start temperature [°C]	Dissociation end temperature [°C]
1st	1	0.237	90%	5%	8.8%	8.7	8.8
1st	2	0.237	60%	3%	3.8%	7.2	7.3
2nd	1	0.365	70%	8%	7.0%	8.7	8.9
2nd	2	0.365	35%	5%	9.1%	7.1	7.3
3rd	1	0.217	80%	9%	5.9%	5.3	7.3
3rd	2	0.217	70%	33%	10.4%	5.5	6.7